

The Pennsylvania State University

The Graduate School

**BODY AND SURFACE WAVE TOMOGRAPHY OF WEST ANTARCTICA AND
SOUTHERN AFRICA: IMPLICATIONS FOR LITHOSPHERIC ARCHITECTURE,
TECTONIC DEVELOPMENT, AND GEODYNAMICS**

A Dissertation in

Geosciences

by

Austin White-Gaynor

© 2020 Austin White-Gaynor

Submitted in Partial Fulfillment
of the Requirements
for the Degree of

Doctor of Philosophy

May 2020

The dissertation of Austin White-Gaynor was reviewed and approved* by the following:

Andrew A. Nyblade
Head of the Department and Professor of Geosciences
Dissertation Advisor
Chair of Committee

Charles J. Ammon
Professor of Geosciences

Sridhar Anandakrishnan
Professor of Geosciences

Victor W. Sparrow
Director of Graduate Program in Acoustics
United Technologies Corporation Professor of Acoustics

Mark E. Patzkowsky
Head of Graduate Programs and Research in Geosciences

ABSTRACT

In this thesis, I present new subcontinental-scale upper mantle velocity models from body wave and surface wave tomography in two regions of the planet experiencing uplift, rifting, and volcanism, West Antarctica and southern Africa. These models are used to address outstanding questions about the nature and origin of plateau uplift, rifting, and volcanism. In Chapter 2, I present a new P-wave tomography model for an area extending from Marie Byrd Land to the Wilkes Subglacial Basin in East Antarctic, developed using new broadband seismic data from stations deployed across the Ross Sea Embayment, combined with data recorded on stations in surrounding regions of West Antarctica. Velocity variations in the model are highly correlated with areas of active volcanism and rifting, as well as with an area of subglacial seismicity, possibly linked to magmatic processes. Across the Ross Sea Embayment, I attribute velocity variations to changes in the thermal structure of the upper mantle resulting from three phases of rifting of the West Antarctica Rift System. The velocity variations could result in $\sim\pm 10$ mW/m² variations in surface heat flow and 10^2 Pa s variations in mantle viscosity. This heterogeneity in the thermo-mechanical properties of the lithosphere could influence the stability of the West Antarctic Ice Sheet, as the ice sheet changes in response to oceanic and atmospheric conditions.

In Chapters 3 and 4, I present new upper mantle velocity models for southern Africa and parts of eastern Africa developed from new data collected on Proterozoic mobile belts adjacent to the Kalahari Craton. These new data provide constraints on upper mantle velocity away from the thick lithosphere of the Kalahari Craton. In Chapter 3, I present P-wave and S-wave velocity models from body wave tomography that show distinct boundaries in upper mantle velocity correlated to tectonic terrane boundaries. Synthetic tests show that, with the exception of deeper structure imaged beneath central Mozambique, the upper mantle velocity variations in southern Africa can be explained by differences in lithospheric thickness alone. In Chapter 4, I test this

interpretation with a shear wave velocity model developed using Rayleigh wave phase dispersion measurements. The improved depth resolution of the surface wave tomography model, compared to the body wave tomography models, allows me to better constrain the depth extent of the velocity differences across the study area. Combined, surface and body wave models indicate that the upper mantle velocity variations in southern Africa, outside of central Mozambique, primarily arise from differences in lithospheric architecture. Therefore, I conclude that the upper mantle beneath southern Africa, with the possible exception of central Mozambique, is not thermochemically perturbed. This finding indicates that the buoyant support for the Southern African Plateau likely resides at mid-to-lower mantle depths.

TABLE OF CONTENTS

LIST OF FIGURES	vii
LIST OF TABLES	xiv
ACKNOWLEDGEMENTS.....	xv
Chapter 1 Introduction	1
West Antarctica.....	2
Southern Africa	3
Chapter 2 Heterogeneous upper mantle structure beneath the Ross Sea Embayment and Marie Byrd Land, West Antarctica, revealed by P-wave tomography	5
Introduction.....	6
Geologic Setting.....	7
Previous Geophysical Studies	11
Data Selection and Preparation	13
Inversion of Travel-Time Residuals.....	15
Results	16
Resolution Tests	18
Checkerboard Tests.....	18
Tabular Body Tests	21
Discussion.....	22
Summary and Conclusions.....	28
Chapter 3 Seismic architecture of the upper mantle beneath southern Africa from body wave tomography	30
Introduction.....	31
Tectonic Background.....	34
Previous Geophysical Studies	36
Data and Methods.....	39
Model Results.....	41
Model Resolution	47
Discussion.....	51
Anomalies Reported in Previous Studies	51
New Anomalies	52
Summary and Conclusions.....	58
Chapter 4 Surface wave tomography of southern Africa: craton vs off-craton upper mantle structure.....	61
Introduction.....	62
Tectonic Background.....	65
Previous Geophysical Studies	65

Rayleigh wave phase velocities.....	67
Inversion for shear wave velocity.....	71
Results	74
Discussion.....	77
Summary and Conclusions.....	82
Chapter 5 Conclusions	84
West Antarctica.....	84
Southern Africa	85
Future Work.....	90
Antarctica	90
Africa	91
Appendix A Supplemental Figures for Chapter 2.....	93
Appendix B Supplemental Figures for Chapter 3.....	97
Appendix C Supplemental Figures for Chapter 4.....	109
Bibliography.....	133

LIST OF FIGURES

- Figure 2-1: a) Generalized tectonic map of the study region. Transantarctic Mountains (TAM) are denoted with parallel line segments (Dalziel and Elliot, 1982). Marie Byrd Land crustal block (MBL, Dalziel and Elliot, 1982) and the Wilkes Subglacial Basin (WSB) are outlined by the dotted and solid lines. The West Antarctic Rift System (WARS) is lightly shaded. RSE: Ross Sea Embayment, EA: East Antarctica. b) Map showing the locations of seismic stations used in this study. Topography is from BEDMAP2 (Fretwell et al., 2013). RI: Ross Island, FR: Ford Ranges, KEP: King Edward VII Peninsula, BSB: Byrd Subglacial Basin. Boundaries for the Eastern Basin (EB) are compiled from several sources (Decesari et al., 2007; Davey and Brancolini, 1995; Brancolini, et al., 1995) with the outermost limit shown by the dotted lines and the inner most limit shown by the solid lines. Shaded regions denoting the Central Trough (CT), Victoria Land Basin (VLB), and Northern Basin (NB) are from Brancolini et al. (1995), while solid outlines denoting the CT, VLB, NB, and Terror Rift (TR) are from Granot et al. (2013). CH: Central High, RI: Ross Island. c) Map of MBL crustal block (Dalziel and Elliot, 1982) showing locations of Cenozoic volcanoes (red circles; LeMasurier et al., 2008) and seismicity (orange circles) reported by (1) Lough et al. (2013) and (2) Winberry and Anandakrishnan (2003). Background topography is from BEDMAP2.....10
- Figure 2-2: Locations of $M \geq 5.5$ earthquakes (red circles) used in this study plotted with respect to the center of the study area (inverted blue triangle).....14
- Figure 2-3: a-d) Depth slices through P-wave model at 100 km increments. Triangles mark station locations. Anomalies A – J discussed in the text are labeled in (b). Black line segments in (d) denote lines of cross-section locations, shown in (e-f). e) Cross-section A-A' through the tomography model, with bed and ice surface profiles above (from BEDMAP2; Fretwell et al., 2013). RIS: Ross Ice Shelf. Other abbreviations are the same as Fig. 2-1. Anomalies A – J discussed in text are labeled. Dark grey triangle marks Mt. Erebus on RI. f) Same as (e) but for cross-section B-B'. MM: Mt. Melbourne...17
- Figure 2-4: a) Input synthetic model with 50 km radius Gaussian tapered spheres with peak amplitude of $\pm 5\%$ centered at 100 km depth. b) Corresponding recovered structure from (a). c) Input synthetic model with 100 km radius Gaussian tapered spheres centered at 200 km depth. d) Corresponding recovered structure from (c). e) Cross-section along A-A' (Fig. 2-3) showing 50 km radius sphere input model from (a) on the upper panel and recovered model from (b) on the lower panel. f) Cross-section along B-B' (Fig. 2-3) showing 100 km radius input model from (c) on the upper panel and recovered model from (d) on the lower panel.....20

- Figure 2-5: a) Cross-section A-A' (Fig. 2-3) with tabular body synthetic input. Anomalies discussed in the text are labeled. All input anomalies have $\pm 4\%$ peak amplitudes, except for the 50 km wide body directly beneath RI corresponding to Anomaly G, which has a -6% peak amplitude. b) Corresponding recovered anomalies. c) Cross-section through the actual model for comparison (same as Fig. 2-3 e).....22
- Figure 2-6: Depth slice at 200 km through P-wave model (same as Fig. 2-3 b), showing the eastern (EB) and western (WB) portions of the RSE, the locations of seismicity in MBL (orange circles), active volcanoes (orange triangles) and seismic stations (open triangles).25
- Figure 3-1: Topographic map showing tectonic boundaries in southern Africa and locations of seismic stations used in the P-wave and S-wave models. Tectonic terranes are labeled as (a) Kaapvaal Craton; (b) Zimbabwe Craton; (c) Limpopo Belt; (d) Bushveld Igneous Province; (e) Tanzania Craton; (f) Congo Craton/Angolan Shield; (g) Rehoboth Province; (h) Bangweulu Block; (i) Irumide Belt; (j) Southern Irumide Belt; (k) Kheis Belt; (l) Okwa Terrane; (m) Namaqua-Natal Belt; (n) Cape Fold Belt; (o) Damara Belt; (p) Mozambique Belt; (q) Etendeka Flood Basalt Province; (r) Okavango Rift; (s) Gariep Belt (Begg et al., 2009; Frimmel and Frank, 1998). Elevations from GEBCO (Weatherall et al., 2015).....33
- Figure 3-2: Horizontal cross-sections through the P-wave (top) and S-wave (bottom) models at 100 km increments. Tectonic boundaries correspond to those in Fig. 3-1.....43
- Figure 3-3: a) Horizontal cross-section through the P-wave model at 200 km depth. Major velocity anomalies are labeled A-K. Surface intersections of cross-sections I-VI are shown with black line segments. Tectonic boundaries are the same as those in Fig. 3-1. b-g) Vertical cross-sections taken through the P-wave model corresponding to black line segments from (a). Intersected anomalies (A-K) are labeled.45
- Figure 3-4: a) Horizontal cross-section through the S-wave model at 200 km depth. Major velocity anomalies are labeled A-K. Surface intersections of cross-sections I-VI are shown with black line segments. Tectonic boundaries are the same as those in Fig. 3-1. b-g) Vertical cross-sections taken through the S-wave model corresponding to black line segments from (a). Intersected anomalies (A-K) are labeled.46
- Figure 3-5: a-d) Horizontal cross-sections of P-wave checkerboard resolution tests taken at 100 km intervals (100-400 km). Intersection line of the III vertical cross-section shown in (e) and (f) is labeled in (c). e) Synthetic P-

- wave velocity model used to create an artificial travel-time dataset. Inversion results from this synthetic dataset are shown in (c) and (f).....49
- Figure 3-6:** a-d) Horizontal cross-sections of S-wave checkerboard resolution tests taken at 100 km intervals (100-400 km). Intersection line of the III vertical cross-section shown in (e) and (f) is labeled in (c). e) Synthetic S-wave velocity model used to create an artificial travel-time dataset. Inversion results from this synthetic dataset are shown in (c) and (f).....50
- Figure 3-7:** a) Tabular body model used to create a synthetic P-wave travel-time dataset representing relatively thin lithosphere (~130 km) adjacent to relatively thick lithosphere (~200 km) beneath the Damara Belt (left of image). A deeper synthetic anomaly is required beneath central Zambia (center of image) and a lower mantle anomaly is required beneath northern Zambia (right of image). The vertical cross-section is taken along transect I (Fig. 3-3). Damara Belt, Zimbabwe Craton (Zim. Cr.) and Mozambique Belt (MB) are labeled. b) Inversion results from synthetic travel-times created using model (a). All anomalies are smeared vertically. c) Vertical cross-section from P-wave model taken along transect I (see Fig. 3-3). d) The same initial tabular model at (a) with a relatively thin lithosphere beneath northern Namibia (left of image) and a deeper low velocity anomaly beneath Mozambique (right of figure). The vertical cross-section is taken along transect III (Fig. 3-3).55
- Figure 3-8:** a) Tabular body model used to create a synthetic S-wave travel-time dataset representing relatively thin lithosphere (~130 km) adjacent to relatively thick lithosphere (~200 km) beneath the Damara Belt (left of image). A deeper synthetic anomaly is required beneath central Zambia (center of image) and a lower mantle anomaly is required beneath northern Zambia (right of image). The vertical cross-section is taken along transect I (Fig. 3-3). Damara Belt, Zimbabwe Craton (Zim. Cr.) and Mozambique Belt (MB) are labeled. b) Inversion results from synthetic travel-times created using model (a). All anomalies are smeared vertically. c) Vertical cross-section from P-wave model taken along transect I (see Fig. 3-3). d) The same initial tabular model at (a) with a relatively thin lithosphere beneath northern Namibia (left of image) and a deeper low velocity anomaly beneath Mozambique (right of figure). The vertical cross-section is taken along transect III (Fig. 3-3).56
- Figure 4-1:** Topographic map showing location of seismic stations used in this study. Corresponding seismic network abbreviations are labeled. Tectonic boundaries (white lines) are from labeled in Figure 3-1.64

Figure 4-2: Location, event origin time, and back-azimuth for earthquakes used for the final inversion. Additional source information can be found in Table F-2.....	68
Figure 4-3: a) Teleseismic earthquake recorded on AfricaArray station CVNA filtered between 30-200 s. b) Earthquake waveform recorded on AfricaArray station SEK filtered between 30-200 s and windowed between a 5.0-2.0 km/s group velocity window. c) Cross-correlogram of the waveforms from (a) and (b). d) Cross-correlogram from (c) filtered by a series of narrow band filters with center periods from 30-200 s and offset from the origin for visibility. Warmer colors are for shorter period filters and cooler colors are from longer period filters.	70
Figure 4-4: Structural phase velocity maps for periods 40 (a), 80 (b), 120 (c), and 200 (d) seconds. Map cells with less than three measurements are not colored.	71
Figure 4-5: a) Starting model from the grid search (black line) and 100 perturbed initial models (gray lines). One standard deviation above and below the mean is marked (dotted lines). AK135 Earth reference model shown with dashed line (Kennett et al., 1995). Cell location marked on inset map. b) Model results from the inversion with mean (black line), one standard deviation above and below the mean (dotted lines), and individual output velocity models (gray lines). Inset: Phase velocities used to constrain the inversion (a-b) along with their uncertainties from Helmholtz tomography. Phase velocities forward calculated for the individual velocity models are shown with gray lines.	73
Figure 4-6: Horizontal cross-sections through the final velocity model at 50 km intervals.....	76
Figure 4-7: a) Areas used to calculate regional average 1D velocity models. KC – Kalahari Craton; DB – Damara Belt; EA – East Africa; NC – Niassa Craton. b) Average 1D velocity profiles calculated for the regions boxed in (a). AK – AK135 (Kennett et al., 1995). c) Percent shear wave velocity difference between 1D velocity profiles in (b).	78
Figure 4-8: a) Horizontal cross-section through the shear wave velocity model at 300 km depth. Boxes encompass a general region for southern Africa (blue) and eastern Africa (red). b) Shear wave velocities of cells within the regional boxes from (a).	82
Figure 5-1: Depth slice at 200 km through P-wave model showing the eastern (EB) and western (WB) portions of the RSE, the locations of seismicity in	

MBL (orange circles), active volcanoes (orange triangles) and seismic stations (open triangles).....	85
Figure 5-2: a) Shear wave velocity difference between the Kalahari Craton and Damara Belt (black line). 1D velocity profiles through the synthetic velocity structure, or tabular bodies, used in Fig. 3-8 a (red) and the adapted profile (blue), more closely representing the black line. b) Synthetic velocity structure from Fig. 3-8 used to create a synthetic dataset of relative travel-times. c) Results from inverting the dataset calculated through (b) d) Synthetic velocity structure created to represent the velocity difference between the Kalahari Craton and Damara Belt from Chapter 4. e) Results from inverting the synthetic dataset created through (d). f) Vertical cross-section through the S-wave model (same as Fig. 3-4 b).....	88
Figure A-1: Model domain showing location of knots in latitude, longitude, and depth. Location of seismic stations marked by white squares.	93
Figure A-2: Trade-off curve analysis for flattening and smoothing parameterization. Each circle represents a unique model run. Optimal parameterization decreases the RMS of travel-time residuals without increasing model roughness. Standard procedure is to choose parameterization that lies within the ‘elbow’ or bend of the trade-off curve (VanDecar, 1991).	94
Figure A-3: Station static terms from the inversion output, plotted over bedrock topography from BEDMAP2 (Fretwell et al., 2013). These terms are subtracted from the relative arrival times to account for shallow structure. In regions with relatively thick, slow crust, positive station terms are subtracted from the arrival times, thereby reducing the overall relative arrival time for the given station. Likewise, for stations situated on thick, fast crust, negative station terms are subtracted, which relatively increase the arrival times.	95
Figure A-4: (top) Rays per grid cell (Fig. A-1) determined from ray tracing using the station and event geometry employed in our final model. Warm colors represent regions with higher ray density. Note that in the central RIS, there is a small region with very high ray density due to the dense cluster of DRIS stations. (bottom) Model results obtained after removing the DRIS station observations. This was performed to decrease the ray density in the central RIS. Note that the high amplitude, low velocity feature (Anomaly F) in the central RIS is now diminished.	96
Figure B-1: Location of earthquakes used to measure relative arrival times for the P-wave (left) and S-wave (right) models.	97

Figure B-2 : Trade-off curves for regularization parameterization. The chosen parameterization is marked.....	98
Figure B-3 : Horizontal cross-sections through the P-wave model at 100 km intervals. Tectonic boundaries (Begg et al., 2009; Frimmel and Frank, 1998) are marked by black lines.....	99
Figure B-4 : Horizontal cross-sections through the S-wave model at 100 km intervals. Tectonic boundaries (Begg et al., 2009; Frimmel and Frank, 1998) are marked by black lines.....	102
Figure B-5 : Horizontal cross-sections through checkerboard synthetic test results for the P-wave model. The starting model consisted of $\pm 5\%$ spheres and a width at half maximum of 200 km. At 700 and greater depths, the width at half maximum was increased to 400 km.	105
Figure B-6 : Horizontal cross-sections through checkerboard synthetic test results for the S-wave model. The starting model consisted of $\pm 5\%$ spheres and a width at half maximum of 200 km. At 700 and greater depths, the width at half maximum was increased to 400 km.	106
Figure B-7 : a) Horizontal cross-section of a synthetic velocity model used to calculate relative travel-times. b) Vertical cross-section through a synthetic P-wave model. c) Results of the inversion of synthetic travel-times calculated through (b). d) Vertical cross-section V from the P-wave model. e) Vertical cross-section through a synthetic S-wave model used to calculate relative travel-times. f) Results of the inversion of travel-times calculated through (e). g) Vertical cross-section V through the S-wave model.....	107
Figure B-8 : Station static terms from the inversion output, plotted over topography from GEBCO (Weatherall et al., 2015). These terms are subtracted from the relative arrival times to account for shallow structure.....	108
Figure C-1 : Example relative phase delays versus epicentral distance difference between stations from Jin and Gaherty, 2015. Cooler colors show phase delay (seconds) measurements for shorter periods and warmer colors show phase delay measurements for longer periods. Gray circles show measurements that did not meet the quality control requirements outlined in Chapter 4. Differences in phase velocities manifest in different slopes in trend lines for the various periods. Negative epicentral distance differences occur when the reference station is further from the event hypocenter than the secondary station.	110
Figure C-2 : Apparent phase velocity maps for all measured periods (30-200 s) from eikonal tomography. Tectonic boundaries (Begg et al., 2009; Frimmel and Frank, 1998) are marked by black lines.....	110

Figure C-3: Connected stations used for cross-correlations with maximum interstation spacing of 850 km and minimum spacing of 20 km for 30, 110, and 200 s period Rayleigh waves.	115
Figure C-4: Number of events contributing to each cell for the phase velocity inversion. This gives a rough estimate of the data distribution, but does not represent the total number of measurements that contribute to each cell, which can include multiple crossing rays per event. Connected stations used for cross-correlations with maximum interstation spacing of 850 km and minimum spacing of 20 km for 30, 70, 110, and 200 s period Rayleigh waves.	115
Figure C-5: Structural phase velocity maps for all measured periods (30-200 s) from Helmholtz tomography. Tectonic boundaries (Begg et al., 2009; Frimmel and Frank, 1998) are marked by black lines.....	119
Figure C-6: Estimates of the standard deviation in phase velocity from stacking phase velocity maps driven from eikonal tomography.....	122
Figure C-7: Absolute phase velocity (30-200 s) differences for each grid cell measured with interstation distances limited to 250 km from the same cell measurement when interstation spacing was increased to 850 km. This shows that the difference between phase velocity measurements with highly restricted interstation spacing are primarily within 0.1 km/s from those measured with the interstation distances increased to 850 km, even at the short periods.....	127
Figure C-8: Example sensitivity kernels for 30-200 s fundamental mode Rayleigh waves through a representative velocity model.	132
Figure C-9: Horizontal cross-sections (50-325 km) through the final shear wave velocity model at 25 km intervals. Tectonic boundaries (Begg et al., 2009; Frimmel and Frank, 1998) are marked by black lines.....	132
Figure C-10: a) Horizontal cross-section through shear wave velocity model. Surface intersections of vertical cross-sections are labeled A-D. b-e) Vertical cross-sections through the shear wave velocity model. Tectonic regions are labeled at the surface. D. Belt – Damara Belt; Kal. Craton – Kalahari Craton; ORZ – Okavango Rift Zone; EA – Eastern Africa; SIB/NC – Southern Irumide Belt / Niassa Craton; MB – Mozambique Belt.	132

LIST OF TABLES

Table 4-1: Parameter spaced used in grid search for best fitting starting 3-layer model..... 72

ACKNOWLEDGEMENTS

This research has been supported by National Science Foundation grants 1142126, 0440032, 0530062, 0824781, 1128936, and 1634108. The findings and conclusion of this thesis do not necessarily reflect the views of the National Science Foundation. The seismic deployments in this dissertation benefited greatly from the technical support of the Incorporated Research Institutions for Seismology (IRIS) through the Portable Array Seismic Studies of the Continental Lithosphere (PASSCAL) Instrument Center at New Mexico Tech. Seismic data are freely available through the IRIS Data Management Center. I would like to personally thank many members of the POLENET field team for their support and guidance during my Antarctic field seasons, including, but not limited to, Terry Wilson, Patrick Shore, David Saddler, Mark Whetu, and Mike Roberts, as well as the engineers from PASSCAL and UNAVCO.

Most of all, I would like to thank my thesis advisor Andrew Nyblade for his personal, professional, and academic support during my time at Penn State. In working with Andy, I received unwavering positive encouragement and benefited from many professional opportunities, all while being treated with respect. Thank you, Andy, for making graduate school such a rewarding and memorable experience.

Thank you, too, to my committee members Chuck Ammon, Sridhar Anandkrishnan, and Victor Sparrow for instilling a sense of academic excellence and curiosity in my work. In no matter what direction my professional life takes me, I will do my best to take these with me. Thanks to the Department of Geosciences faculty and staff for creating and maintaining such a collaborative and rewarding environment. I would also like to acknowledge Eli Baker and Rick Schult from the Air Force Research Laboratory and Michael Cleveland from Los Alamos National Laboratory for their collaboration and for inviting me out to New Mexico.

I would like to thank many people from the room 444 lab for directly contributing to my success. Special thanks to Cristo Ramirez, Kyle Homman, Chengping Chai, Marsella Kachingwe, Erica Emry, J.P. O'Donnell, and Natalie Accardo, and the many other people who came through. And thanks to Barbara and Toni for keeping the lab running smoothly.

A big shout out to my friends in State College, many of whom kept me fed and sane over the past few years. I want to sincerely thank Helen Gall for encouraging me to apply to graduate school, keeping me in it, and, of course, so much more. Lastly, I am extremely lucky to have been, and to continue to be, so motivated, encouraged, and supported by my two sisters, my brother-in-law, my mother, and my father.

Chapter 1

Introduction

In this thesis, seismic tomography of the upper mantle on sub-continental scales is used to improve our understanding of two continental regions where there remain outstanding questions about plateau uplift, rifting, and volcanism. In West Antarctica, there are several remaining questions about its tectonic past, evidence of which is often masked by the thick Antarctic ice sheet. For example, the history of the West Antarctica Rift System through to present day rifting and volcanism is not fully known. Upper mantle thermal structure is clearly linked to the high elevations and volcanism in Marie Byrd Land, but how that system connects to volcanism on Ross Island is an open area of investigation. In addition, it is not well understood how upper mantle viscoelastic properties, which can be constrained by seismic tomography, influence ice sheets as they adjust to climate-induced changes in atmospheric and oceanic conditions. In another region with anomalously high elevations, the Southern African Plateau in southern Africa, whether thermal anomalies in the upper mantle contribute to the excess topography is unclear. Continental rifting is ongoing in southern Africa, but the extent to which the upper mantle thermal structure can be correlated with present day rifting has also not been determined.

A useful tool for addressing such questions about the origin of plateau uplift, rifting, and volcanism is seismic tomography. Pioneering work in seismic tomography in the 1980s and 1990s developed regional-scale methodologies that increased model resolution, compared to previous global models, by 1-2 orders of magnitude (Romanowicz, 2003). Regional-scale methods were quickly applied to portable and temporary seismic networks, including long (~1000 km or more) linear arrays, deployed in the late 1990s and early 2000s (e.g., Fouch et al., 2004; Watson et al., 2006). In the following decade, the expansion of semi-permanent arrays in

Antarctica and Africa, including the POLENET network in Antarctica and the AfricaArray network in Africa, created regional datasets with long, continuous records. These networks fundamentally changed imaging capabilities, because data from the semi-permanent stations, used with data from sparse permanent stations, and from denser temporary networks of stations, allow for improved model resolution at the sub-continental scale.

In this thesis, I present new upper mantle velocity models for West Antarctica and southern Africa developed from regional-scale body wave and surface wave tomography, using data collected from recently deployed temporary networks in the Ross Sea Embayment in Antarctica, and Namibia, Botswana, South Africa, and Mozambique in southern Africa, together with previously collected seismic data. In each area, these new models enable improved characterization of the physical properties of the upper mantle beneath several adjacent tectonic terranes, enabling me to address several outstanding questions about the origin of plateau uplift, rifting, and volcanism within these regions.

West Antarctica

Previous seismic tomography studies using data from temporary networks (e.g., Watson et al., 2006; Lloyd et al., 2015; Brenn et al., 2017) and recent continental-scale networks (e.g., Shen et al., 2018) have revealed an upper mantle beneath West Antarctica that is not as uniformly slow as first-generation global models suggested (e.g., Sieminski et al., 2003; Ritzwoller et al., 2001; Danesi and Morelli, 2001). For example, Watson et al. (2006) imaged a sharp boundary between the lithosphere in East Antarctica and West Antarctica, as well as a low velocity anomaly in the upper mantle beneath Ross Island, an area of active volcanism. In central West Antarctica, the model from Lloyd et al. (2016) refined the boundary of a low velocity anomaly in the upper mantle, correlated with Cenozoic volcanism in that region. However, a possible

connection between the upper mantle thermal anomalies in these two regions beneath the Ross Sea Embayment could not be resolved.

Between 2014-2017, the RIS/DRIS (see Section 2.3) network was deployed and consisted of 34 broadband seismometers on and around the floating Ross Ice Shelf within the Ross Sea Embayment. Spatially, this network connected the linear seismic networks in East Antarctica (Watson et al, 2006; Brenn et al., 2017) to the linear networks in West Antarctica (Lloyd et al., 2016). Using data recorded on the RIS, TAMSEIS, TAMNET, and POLENET linear arrays, as well as on regional POLENET and permanent stations in Antarctica, I developed a relative P-wave velocity model for West Antarctica, spanning the eastern half of West Antarctica, from Marie Byrd Land, across the Ross Sea Embayment, and into East Antarctica.

From this model, I concluded that the upper mantle in West Antarctica is characterized by $\pm 0.5\%$ velocity variations over 100s of km, and associated much of the variability to tectonothermal alteration of the upper mantle during several phases of rifting of the West Antarctica Rift System. The magnitude of the seismic velocity variations indicates ~ 100 K variation in the lithospheric mantle, which could lead to 10^2 Pa s differences in mantle viscosity and ± 10 mW/m² variations in surface heat flow, possibly influencing the stability of the West Antarctic Ice Sheet by affecting basal ice conditions and glacial isostatic adjustment. The results of this study (Chapter 2) have been published. (White-Gaynor et al., 2019, Heterogeneous upper mantle structure beneath the Ross Sea Embayment and Marie Byrd Land, West Antarctica, revealed by P-wave tomography, *Earth and Planetary Science Letters*, 513 pp.40-50).

Southern Africa

On average, the Southern African Plateau has elevations of ~ 1 km, >500 m of which is considered anomalous (Nyblade and Robinson, 1994). In the mid-to-lower mantle beneath

southern Africa, a large thermochemical anomaly, the African Superplume, connects to the upper mantle beneath eastern Africa (Mulibo and Nyblade, 2013b). The thermal anomaly in the upper mantle beneath eastern Africa is considered to provide the buoyancy source of the ~1 km high East African Plateau (Moucha and Forte, 2011). The contribution from thermal anomalies in the upper mantle beneath southern Africa to the elevation of the Southern African Plateau is still unclear, as most images of the mantle in southern Africa were created using data recorded on stations in the Kalahari Craton, and imaging upper mantle structure beneath thick, cratonic lithosphere can be difficult.

In Chapter 3, I use data recorded from seismic stations deployed in the thinner mobile belts, adjacent to the Kalahari Craton. The stations are located in Namibia, Botswana, South Africa, and Mozambique. Using relative first-arrival times from teleseismic earthquakes, I present new P-wave and S-wave velocity models of the upper mantle beneath southern Africa and parts of eastern Africa (Chapter 3). My models illuminate differences in lithospheric architecture between tectonic terranes and show that, outside of central Mozambique, there is little indication of a thermochemical anomaly in the upper mantle beneath southern Africa.

In Chapter 4, I present an upper mantle shear wave velocity model that was developed by inverting Rayleigh wave phase velocity dispersion curves. Data for this study come from the same stations used in Chapter 3. While body wave tomography models (e.g., Chapter 3) can have high spatial resolution, surface wave tomography can yield models with better depth resolution. By comparing model results, I show that my surface wave model corroborates conclusions obtained from body wave tomography models (Chapter 3), namely that the velocity structure of the upper mantle beneath southern Africa, with the exception of central Mozambique, does not indicate the presence of a thermal perturbation. The implication of this finding is that, unlike the East African Plateau, the source of the buoyant support for the Southern African Plateau likely resides in the mid-to-lower mantle, and not the upper mantle.

Chapter 2

Heterogeneous upper mantle structure beneath the Ross Sea Embayment and Marie Byrd Land, West Antarctica, revealed by P-wave tomography

Abstract

We present an upper mantle P-wave velocity model for the Ross Sea Embayment (RSE) region of West Antarctica, constructed by inverting relative P-wave travel-times from 1881 teleseismic earthquakes recorded by two temporary broadband seismograph deployments on the Ross Ice Shelf, as well as by regional ice- and rock-sited seismic stations surrounding the RSE. Faster upper mantle P-wave velocities ($\sim +1\%$) characterize the eastern part of the RSE, indicating that the lithosphere in this part of the RSE may not have been reheated by mid-to-late Cenozoic rifting that affected other parts of the Late Cretaceous West Antarctic Rift System. Slower upper mantle velocities ($\sim -1\%$) characterize the western part of the RSE over a ~ 500 km-wide region, extending from the central RSE to the Transantarctic Mountains (TAM). Within this region, the model shows two areas of even slower velocities ($\sim -1.5\%$) centered beneath Mt. Erebus and Mt. Melbourne along the TAM front. We attribute the broader region of slow velocities mainly to reheating of the lithospheric mantle by Paleogene rifting, while the slower velocities beneath the areas of recent volcanism may reflect a Neogene-present phase of rifting and/or plume activity associated with the formation of the Terror Rift. Beneath the Ford Ranges and King Edward VII Peninsula in western Marie Byrd Land, the P-wave model shows lateral variability in upper mantle velocities of $\pm 0.5\%$ over distances of a few hundred km. The heterogeneity in upper mantle velocities imaged beneath the RSE and western Marie Byrd Land (MBL), assuming no significant variation in mantle composition, indicates variations in upper mantle temperatures of at least 100°C . These temperature variations could lead to differences in surface heat flow of $\sim \pm 10 \text{ mW/m}^2$ and mantle viscosity of 10^2 Pa s regionally across the study

area, possibly influencing the stability of the West Antarctic Ice Sheet by affecting basal ice conditions and glacial isostatic adjustment.

Introduction

Over the past two decades, substantial progress has been made in deploying temporary broadband seismic stations throughout Antarctica, leading to many advances in our understanding of crustal and mantle structure across much of the continent. With improved seismic data coverage, it has become clear that there is significantly more heterogeneity in West Antarctic (WA) upper mantle structure than earlier, lower resolution seismological studies of the region suggested (*e.g.*, Masters et al., 1996; Danesi and Morelli, 2001; Ritzwoller et al., 2001). For example, data from the POLENET network have illuminated differences in crustal and upper mantle structure beneath the Marie Byrd Land (MBL) crustal block and portions of the central West Antarctic Rift System (WARS) (Hansen et al., 2014; Chaput et al., 2014; Lloyd et al., 2015; Heeszel et al., 2016; Shen et al., 2018) (Fig. 2-1), while data from the TAMSEIS and TAMNNET networks have illuminated heterogeneous structure beneath WA adjacent to the boundary with East Antarctica (EA) (*e.g.*, Watson et al., 2006; Lawrence et al., 2006; Brenn et al., 2017; Graw et al., 2016).

Further characterizing the nature of heterogeneous WA upper mantle structure is not only important for advancing our understanding of the thermo-tectonic state of the crust and upper mantle but also for unraveling the geodynamic history of the WARS. In addition, it can provide improved constraints on surface heat flow and mantle viscosity, particularly if the heterogeneity is caused by variations in mantle temperature, and consequently help in estimating future sea level rise. Mantle viscosity affects glacial isostatic adjustment, and both glacial isostatic adjustment and surface heat flow can influence the response of ice sheets to climactic forcings

(Gomez et al., 2015; Barletta et al., 2018).

Improved data coverage over a large portion of WA not included within the footprints of previous networks (*e.g.*, TAMSEIS, TAMNNET, and POLENET) has recently been provided by the coupled RIS (Mantle Structure and Dynamics of the Ross Sea from a Passive Seismic Deployment on the Ross Ice Shelf) and DRIS (Dynamic Response of the Ross Ice Shelf to Wave-Induced Vibrations) projects. The RIS/DRIS network was deployed primarily on the floating ice of the Ross Ice Shelf between 2014-2017 and spanned much of the Ross Sea Embayment (RSE) (Fig. 2-1). In this study, we used data from the RIS/DRIS deployment and from several other networks (Fig. 2-1) to image the P-wave velocity structure of the upper mantle under the RSE and surrounding areas. Our P-wave model has improved spatial resolution compared to many previously published models (*e.g.*, Ritzwoller et al., 2001; Danesi and Morelli, 2001; Sieminski et al., 2003 and references therein), revealing new regions of heterogeneity within the WA upper mantle, as well as providing enhanced resolution of heterogeneous structure initially identified in previous studies (*e.g.*, Hansen et al., 2014; Heeszel et al., 2016). We attribute the imaged heterogeneity in upper mantle structure primarily to changes in mantle temperature, discuss how those changes could result from the history of rifting in WA, and examine the implications of those changes for surface heat flow and mantle viscosity.

Geologic Setting

The Antarctic continent is composed of EA, a large Precambrian shield, and WA, which consists of several crustal blocks within a wide region of extended crust (Fig. 2-1; Dalziel and Elliot, 1982). Separating EA from WA are the ~3,500 km-long, 4 km-high Transantarctic Mountains (TAM) (Fitzgerald, 2002). The EA-WA lithospheric boundary has experienced numerous periods of subduction, transpression, and extension since the Neoproterozoic

(Fitzgerald, 2002). The TAM principally consist of metamorphic basement rocks deformed during the Cambrian-Ordovician Ross Orogeny overlain by thick, undeformed Devonian to Triassic Beacon Supergroup sediments (Fitzgerald, 2002). Major uplift of the TAM is thought to have initiated in the Paleogene (Fitzgerald, 1992).

Bounding the EA margin of the northern TAM within Northern Victoria Land is the Wilkes Subglacial Basin, a ~400 km-wide depression with mean bedrock elevations ~500 m below sea level (Fig. 2-1). Several models have been proposed for the origin of the Wilkes Subglacial Basin (*e.g.*, Ferraccioli et al., 2009 and references therein), and its geodynamics are of broad interest because of the potential for substantial continental ice mass loss from the basin (Rignot et al., 2008).

MBL and the RSE sector of the WARS make up the majority of the WA portion of the study area (Fig. 2-1 a). MBL is the largest crustal block in WA and contains numerous Cenozoic volcanic centers that underlie, and in some cases protrude through the West Antarctic Ice Sheet. Outcrops near the coast indicate that the regional basement is composed of lowermost Paleozoic metamorphosed granitic rocks intruded by Devonian through Cretaceous magmas (Mukasa and Dalziel, 2000). Oligocene to Holocene alkaline volcanics associated with rifting of the WARS dominate most of the interior outcrops (LeMasurier, 1990); however, some lavas within a region of MBL have isotopic and trace elemental signatures that suggest a mantle source with a residual subduction component (LeMasurier et al., 2016). Proposed mechanisms for melt generation include a mantle plume, an upper mantle hotspot related to past subduction, and slab delamination (LeMasurier et al., 2016; LeMasurier and Landis, 1996; Finn et al., 2005). A region of seismicity arising from magmatic activity has been observed in MBL beneath the Executive Committee Range (Lough et al., 2013), and a second possible region has been identified in the King Edward VII Peninsula (KEP; Fig. 2-1 c) (Winberry and Anandkrishnan, 2003).

While there is some indication that rifting in WA began in the Jurassic, along with the emplacement of the Karoo-Ferrar Large Igneous Province, the primary phase of crustal extension occurred in the Late Cretaceous during the breakup of Gondwana (Siddoway, 2008). A second pulse of extension is thought to have occurred along the TAM margin in the Cenozoic, coeval with a period of TAM uplift and volcanism along the TAM margin near Ross Island (Fig. 2-1) (Fitzgerald, 2002).

The Ross Ice Shelf overlays much of the RSE sector of the WARS, which consists of a series of Late Cretaceous asymmetric grabens, including the Eastern Basin, Central Trough, Victoria Land Basin, and Northern Basin (Fig. 2-1 b) (Davey and Brancolini, 1995). The Eastern Basin spans the region east of 180° longitude in the embayment, from the continental slope southward beneath the Ross Ice Shelf (Davey, 1981). The western portion of the RSE, closer to the TAM boundary, is composed of the Central Trough, Victoria Land Basin, and Northern Basin, hereafter referred to as the western basins. The Victoria Land Basin has been associated with a pulse of extension during the Paleogene (Fitzgerald, 2002; Fielding et al., 2006). Post-Oligocene (Neogene) rifting is thought to have occurred within the narrow Terror Rift, which lies within the Victoria Land Basin, and is possibly associated with transtension and seafloor spreading (Fig. 2-1 b) (Granot et al., 2013; Fielding et al., 2006) or the impingement of a mantle plume (Phillips et al., 2018).

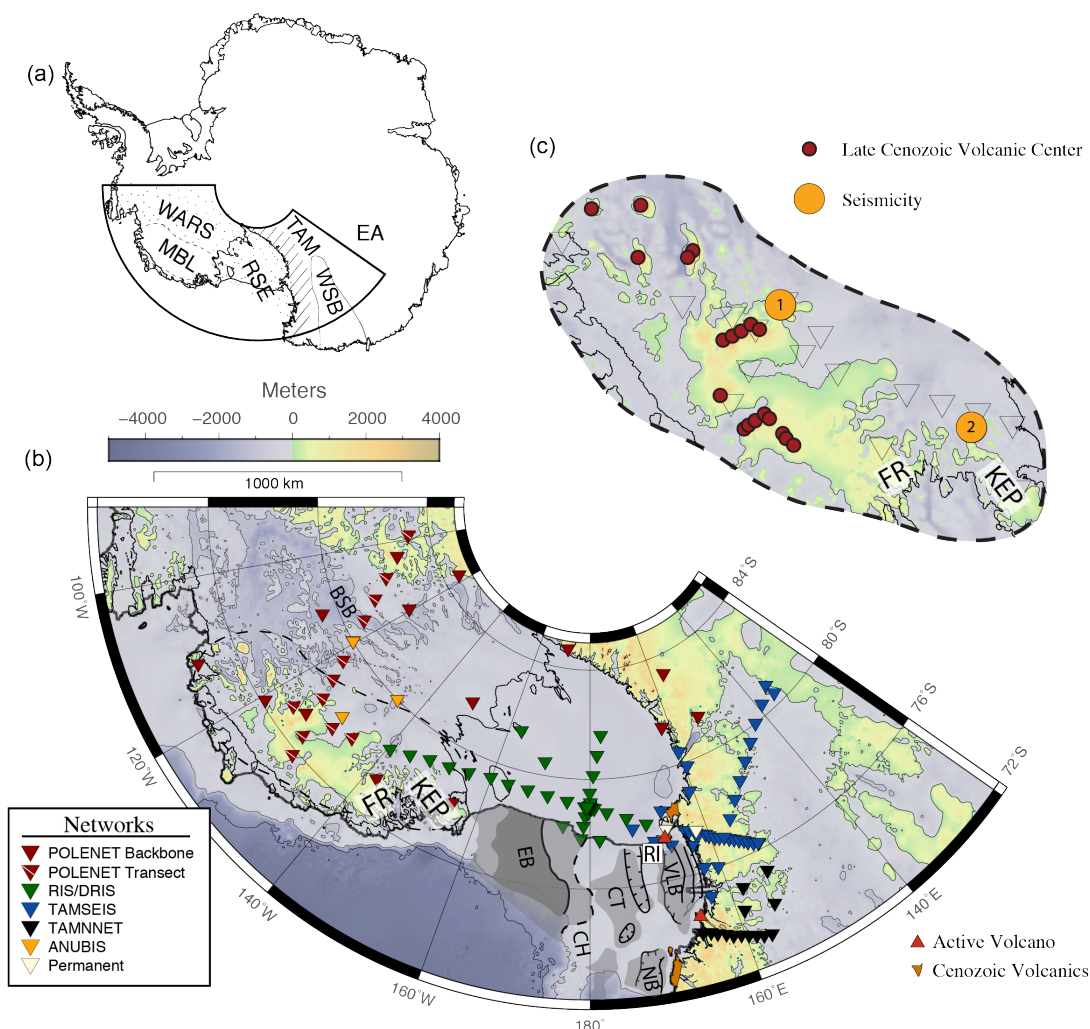


Figure 2-1: a) Generalized tectonic map of the study region. Transantarctic Mountains (TAM) are denoted with parallel line segments (Dalziel and Elliot, 1982). Marie Byrd Land crustal block (MBL, Dalziel and Elliot, 1982) and the Wilkes Subglacial Basin (WSB) are outlined by the dotted and solid lines. The West Antarctic Rift System (WARS) is lightly shaded. RSE: Ross Sea Embayment, EA: East Antarctica. b) Map showing the locations of seismic stations used in this study. Topography is from BEDMAP2 (Fretwell et al., 2013). RI: Ross Island, FR: Ford Ranges, KEP: King Edward VII Peninsula, BSB: Byrd Subglacial Basin. Boundaries for the Eastern Basin (EB) are compiled from several sources (Decesari et al., 2007; Davey and Brancolini, 1995; Brancolini, et al., 1995) with the outermost limit shown by the dotted lines and the inner most limit shown by the solid lines. Shaded regions denoting the Central Trough (CT), Victoria Land Basin (VLB), and Northern Basin (NB) are from Brancolini et al. (1995), while solid outlines denoting the CT, VLB, NB, and Terror Rift (TR) are from Granot et al. (2013). CH: Central High, RI: Ross Island. c) Map of MBL crustal block (Dalziel and Elliot, 1982) showing locations of Cenozoic volcanoes (red circles; LeMasurier et al., 2008) and seismicity (orange circles) reported by (1) Lough et al. (2013) and (2) Winberry and Anandakrishnan (2003). Background topography is from BEDMAP2.

Previous Geophysical Studies

The first continental-scale tomographic images of the upper mantle beneath Antarctica, extracted from global surface wave tomography models and constrained by only a few observations in Antarctica, showed fast upper mantle velocities beneath much of the continent (Roult et al., 1994; Masters et al., 1996). By adding data from additional permanent seismic stations in Antarctica, a next generation of continental-scale surface wave models achieved improved resolution and identified a dichotomy in the Antarctic upper mantle structure, with fast velocities beneath EA and slow velocities beneath WA (Ritzwoller et al., 2001; Danesi and Morelli, 2001; Sieminski et al., 2003).

Many of the earliest geophysical investigations of the WARS seeking regional-scale resolution of crustal and upper mantle structure were based on marine and aerogeophysical surveys (*e.g.*, Behrendt et al., 1996; Trey et al., 1999; Karner et al., 2005). For example, Behrendt et al. (1996) reported evidence for Cenozoic volcanism, based on aeromagnetic signatures, extending from Ross Island toward the central RSE along reactivated Mesozoic faults. A crustal model derived from gravity observations in the RSE showed anti-correlation of gravity anomalies with many sedimentary basins, suggesting a two-phase rift history that differentiated the Eastern Basin, Central Trough, Victoria Land Basin and Northern Basin from the Terror Rift (Karner et al., 2005). Using data from a marine seismic refraction survey across the front of the Ross Ice Shelf, Trey et al. (1999) imaged P_n velocities of ≥ 8.0 km/s in the uppermost mantle across the RSE, with a reduction to ~ 7.8 km/s near Ross Island. Together, many of the regional-scale geophysical studies pointed to a degree of heterogeneity in the crust and upper mantle beneath WA not resolved in continental-scale tomography models.

Starting in the late 1990s, the development of portable broadband seismic stations led to a substantial improvement in Antarctic terrestrial seismic data coverage. From 2000-2003, the

TAMSEIS project included 45 broadband seismic stations deployed from the TAM front near Ross Island into EA. Using data from that project, Watson et al. (2006) imaged a sharp lithospheric boundary between EA and WA below the TAM. Since 2007, the POLENET project has operated a backbone network of seismic stations in EA and WA augmented with two temporary regional arrays (Fig. 2-1 b). Lloyd et al. (2015) used data from the POLENET stations to develop P- and S-wave tomography models that show a large-scale low velocity anomaly in the upper mantle beneath MBL and parts of the central WARS. Combining the POLENET and TAMSEIS data, continental-scale body wave (Hansen et al., 2014) and surface wave (Heeszel et al., 2016) tomography models imaged upper mantle structure more broadly beneath the WARS, but limited resolution in these models from a lack of stations in the RSE region make it difficult to determine if low velocity anomalies beneath MBL and Ross Island connect at upper mantle depths beneath the RSE.

The 2012-2015 deployment of the TAMNNET array in Northern Victoria Land provided additional data for imaging the WA-EA boundary, parts of the RSE around the Terror Rift and its active volcanic centers, and parts of the Wilkes Subglacial Basin (Brenn et al., 2017; Graw et al., 2016). Shen et al. (2018) combined the previous broadband datasets with the RIS/DRIS data to image the shear-wave velocity structure of the WA crust and upper mantle using receiver functions and Rayleigh waves from ambient noise and earthquakes. Their results show that both the lithosphere and crustal thickness is highly variable throughout the region, with thicker lithosphere in the eastern Ross Sea compared to the western Ross Sea. Ramirez et al. (2016; 2017), Chaput et al. (2014), and Lawrence et al. (2006) have also investigated crustal and upper mantle structure beneath these networks using a variety of techniques.

Data Selection and Preparation

The primary dataset used for this study comes from the RIS/DRIS network (https://doi.org/10.7914/SN/XH_2014), which consisted of a two-year deployment of 34 broadband seismometers (Fig. 2-1 b). The RIS project deployed 18 seismometers with ~80 km spacing across the Ross Ice Shelf parallel to the shelf coast, from Ross Island to MBL. The simultaneous DRIS project deployed 16 seismometers N-S along the center of the Ross Ice Shelf, parallel to ice flow, with ~5-20 km spacing. Because of the up to ~600 m water column underlying the Ross Ice Shelf, S-waves were not well recorded, and so we limit our investigation here to the use of teleseismic P-waves.

We also used data from 28 regional POLENET (https://doi.org/10.7914/SN/YT_2007) stations in the TAM, MBL, and the central WARS, 15 TAMNNET stations (https://doi.org/10.7914/SN/ZJ_2012) in Northern Victoria Land, and 35 TAMSEIS stations (https://doi.org/10.7914/SN/XP_2000) in the TAM and EA. In addition, data were used from two Antarctic Network of Unattended Broadband Seismometers (ANUBIS; https://doi.org/10.7914/SN/YI_1997), as well as from permanent Global Seismic Network stations SBA (<https://doi.org/10.7914/SN/GT>) and VNDA (<https://doi.org/10.7914/SN/IU>). In total, data from 116 stations were used, spanning a timeframe from 2001-2017 and ranging geographically from the EA craton, across the TAM and the Ross Ice Shelf, and throughout much of MBL and the WARS (Fig. 2-1 b).

We gathered teleseismic P-waves for $M \geq 5.5$ earthquakes at epicentral distances ranging from 30-90°. Vertical-component waveforms for 1881 events were corrected for instrument response and bandpass filtered between 0.5-5 Hz. We manually picked initial P-wave arrivals on all available traces for each event. More precise relative arrival times were then determined for events with three or more picks using the multichannel cross-correlation (MCCC) approach of

VanDecar and Crosson (1990). This technique uses a three-second window around the initial picks and cross-correlates all combinations of traces for each event to find the ensemble correlation maxima. We accepted only cross-correlation coefficients of ≥ 0.70 , with 93% (*i.e.*, 1727) of the events meeting this threshold. A regularized least-squares optimization was used to find the best-fitting mean arrival time, from which cross-correlation coefficients and their distributions, as well as relative arrival times and data error, were calculated. Figure 2-2 shows the locations of all events used in the final inversion. It is important to note that uneven azimuthal source distribution can lead to a bias of the model in the direction of the denser source coverage. Fortunately, the dense source distribution from the Andean and Sumatran subduction zones led to an increased sensitivity in our model to structure roughly along strike of the linear portion of the RIS/DRIS deployment. The dataset yielded a total of 32,454 P-wave relative arrival times, with 11,381 (~35%) coming from the RIS/DRIS stations.

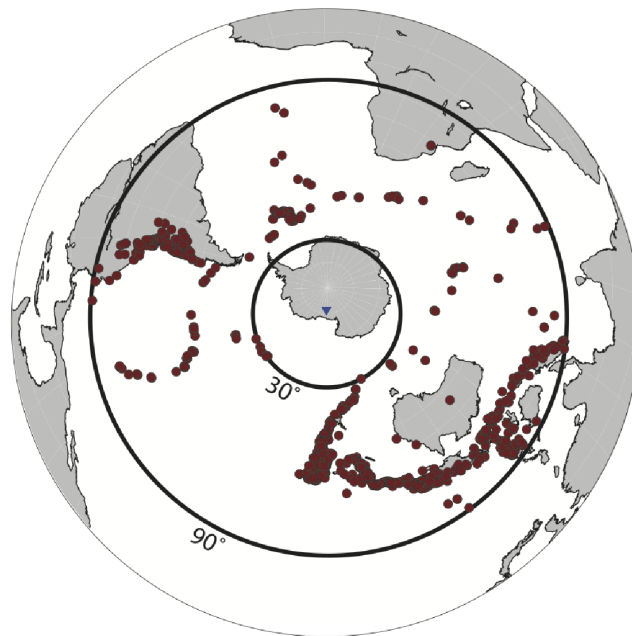


Figure 2-2: Locations of $M \geq 5.5$ earthquakes (red circles) used in this study plotted with respect to the center of the study area (inverted blue triangle).

Inversion of Travel-Time Residuals

The relative P-wave arrival times were inverted for variations in mantle velocities using the VanDecar (1991) method, which employs a conjugate-gradient algorithm and simultaneously solves for 3D updates to model slowness, station static terms, and event relocation terms by reducing the misfit of travel-time residuals. The station terms account for shallow structure at depths that lack crossing ray paths (*i.e.*, <50 km), and the event relocation terms absorb event location error and heterogeneous structure outside of the model domain. We incorporated smoothing and flattening regularization to stabilize the inversion.

The model domain for the inversion extended from 132°E to 97°W longitude, 67°S to 89°S latitude, and from the surface to 1600 km depth. Intersecting grid lines, or knots, were spaced 2° apart in longitude and 0.5° apart in latitude within the central portion of the model domain (*i.e.*, between 72-83°S, 139°-180°E, and 180-107°W; Fig. A-1), with variable knot spacing at depth. Between the surface and 200 km depth, knots were spaced at 25 km, between 200-1200 km depth knots were spaced at 50 km, and between 1200-1600 km depth they were spaced at 100 km. Outside this central region, knot spacing gradually increased in longitude and latitude, with the same vertical spacing as the central portion.

As first steps in the inversion method, we numerically calculated partial derivatives at each knot using slowness perturbations from the 1D IASP91 model (Kennett and Engdhal, 1991), and initial travel-time residuals were calculated relative to that velocity model. During the inversion process, models were then iteratively updated until changes in the model resulted in insignificant (<0.01 s) changes to the RMS travel-time residual. To select optimal smoothing and flattening parameters, we used a trade-off curve between the RMS travel-time residual reduction and the model roughness (Fig. A-2).

Results

Model results are shown in Figure 2-3, where the P-wave velocities (V_P) are plotted as percent differences relative to the model mean. Across MBL, a -0.75% V_P anomaly is observed between ~ 75 and >500 km depth (Anomaly A; Fig. 2-3). There is some evidence that Anomaly A continues into the central WARS along the linear portion of the POLENET Transect array (Fig. 2-1); however, outside of this region, Anomaly A is located mainly beneath the area of Cenozoic volcanism in MBL (Fig. 2-3). In the regions surrounding Anomaly A, relatively fast (0.75% V_P) structure is present from ~ 75 - 300 km depth. Anomaly B, a region of higher V_P ($\sim 0.75\%$), separates Anomaly A from a region of lower V_P (Anomaly C) within the KEP (Fig. 2-3). Anomaly C is isolated laterally and is present to a depth of ~ 400 km. Both Anomalies B and C are ~ 200 km wide along-strike of the RIS/DRIS network.

Our model also shows clear differences in the upper mantle structure between the eastern and western RSE. The eastern RSE is associated with a $\sim 0.25\%$ V_P anomaly in the upper 400 km of the model space (Anomaly D). This anomaly is ~ 500 km wide, extending from the edge of the KEP to the center of the RSE. In the western RSE, a ~ 500 km wide low V_P anomaly (-0.50% ; Anomaly E) parallels the front of the TAM and is present down to ~ 600 km depth. Within this broader low velocity region, three distinct areas of even lower V_P exist (Anomalies F, G, and H). Anomaly F is located in the central RSE, near the front of the Ross Ice Shelf, while Anomalies G and H are situated along the TAM boundary, directly beneath areas of recent and active volcanism (Fig. 2-1 c). In cross-section, Anomaly F is separated from Anomaly G by mantle with mean V_P structure (Fig. 2-3 e); however, there is connectivity between Anomalies G and H along the Terror Rift (Fig. 2-3 f). Anomalies F, G, and H are restricted to the upper 300 km of the model space.

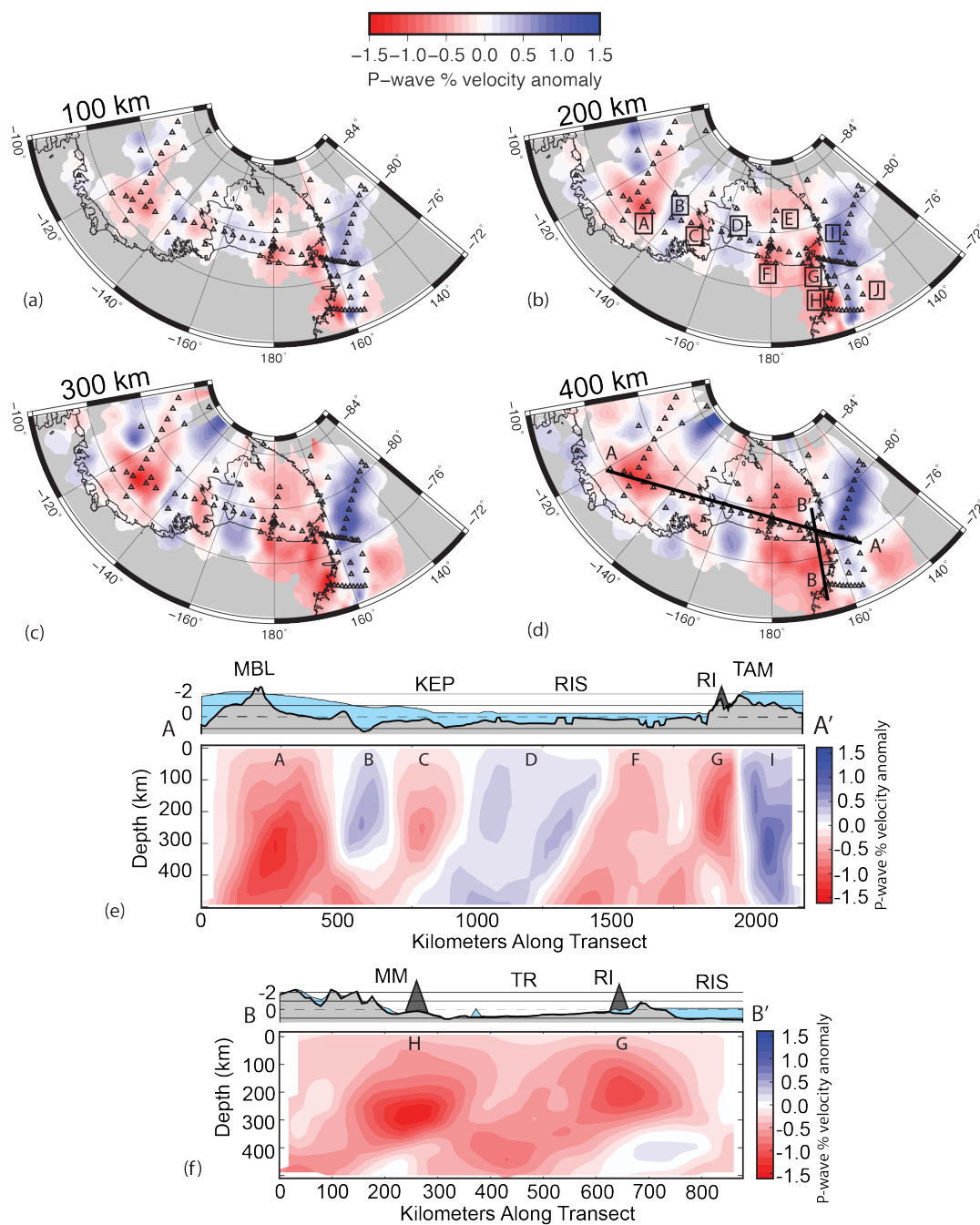


Figure 2-3: a-d) Depth slices through P-wave model at 100 km increments. Triangles mark station locations. Anomalies A – J discussed in the text are labeled in (b). Black line segments in (d) denote lines of cross-section locations, shown in (e-f). e) Cross-section A-A' through the tomography model, with bed and ice surface profiles above (from BEDMAP2; Fretwell et al., 2013). RIS: Ross Ice Shelf. Other abbreviations are the same as Fig. 2-1. Anomalies A – J discussed in text are

labeled. Dark grey triangle marks Mt. Erebus on RI. f) Same as (e) but for cross-section B-B'. MM: Mt. Melbourne.

A pronounced V_P gradient is present in our model under the TAM north of $\sim 80^\circ\text{S}$ latitude. There is a $\sim 2.5\%$ increase in V_P from the WARS to the EA flank of the TAM. Within EA, a $\sim 1.25\%$ V_P anomaly (Anomaly I) is present between ~ 50 - 500 km depth. All of EA has above average V_P except for the Wilkes Subglacial Basin. Anomaly J within the Wilkes Subglacial Basin has a peak anomalous V_P of -0.75% and is found north of $\sim 75^\circ\text{S}$ latitude (Fig. 2-3).

The station static terms removed during the inversion process are positive for regions with slower and somewhat thinner than average crust (*i.e.*, MBL, 27 km; Chaput et al., 2014; Ramirez et al., 2017) and negative in areas of faster and thicker than average crust (*i.e.*, TAM, 42 km; Chaput et al., 2014; Ramirez et al., 2017). Where crustal thickness is much thinner than average (*i.e.*, RSE, 19 km; Trey et al., 1999), station static corrections are relatively small (Fig. A-3).

Resolution Tests

Checkerboard Tests

Model resolution was tested using a series of synthetic checkerboard tests (Fig. 2-4). We placed gaussian tapered spheres with peak amplitudes of $\pm 5\%$ and radii of 50 km and 100 km at depths of 100 km and 200 km, respectively. Travel-times with added noise (4% standard deviation) were then calculated for the synthetic models and inverted to determine which parts of the model domain show the best recovery. For the 50 km radius spheres centered at 100 km

depth, a majority of the checkers are recovered along the A-A' transect (Fig. 2-4 e). The model recovers roughly 10-15% of the initial amplitudes, with the best recovery around Ross Island (Fig. 2-4 a-b). Vertical smearing is common in body wave tomography because of the vertical nature of the ray paths. On the A-A' transect, vertical smearing of ~100 km places peak amplitudes at ~200 km depth rather than at the initial 100 km position (Fig. 2-4 e). Likewise, for the 100 km radius spheres placed at 200 km depth (Fig. 2-4 c-d, f), vertical smearing of ~100 km occurs, resulting in peak amplitude (20-30%) recovery at ~300 km depth. Amplitude recovery of the checkerboard structures depends on the regularization (*i.e.*, smoothing and flattening) used in the inversion. Because our model spans a relatively wide region (55° in longitude or ~2500 km), relatively high smoothing and flattening weights were applied in the inversion. Nonetheless, the 20-30% amplitude recovery achieved is within the range of previous studies using similar tomographic techniques (*e.g.*, Watson et al., 2006).

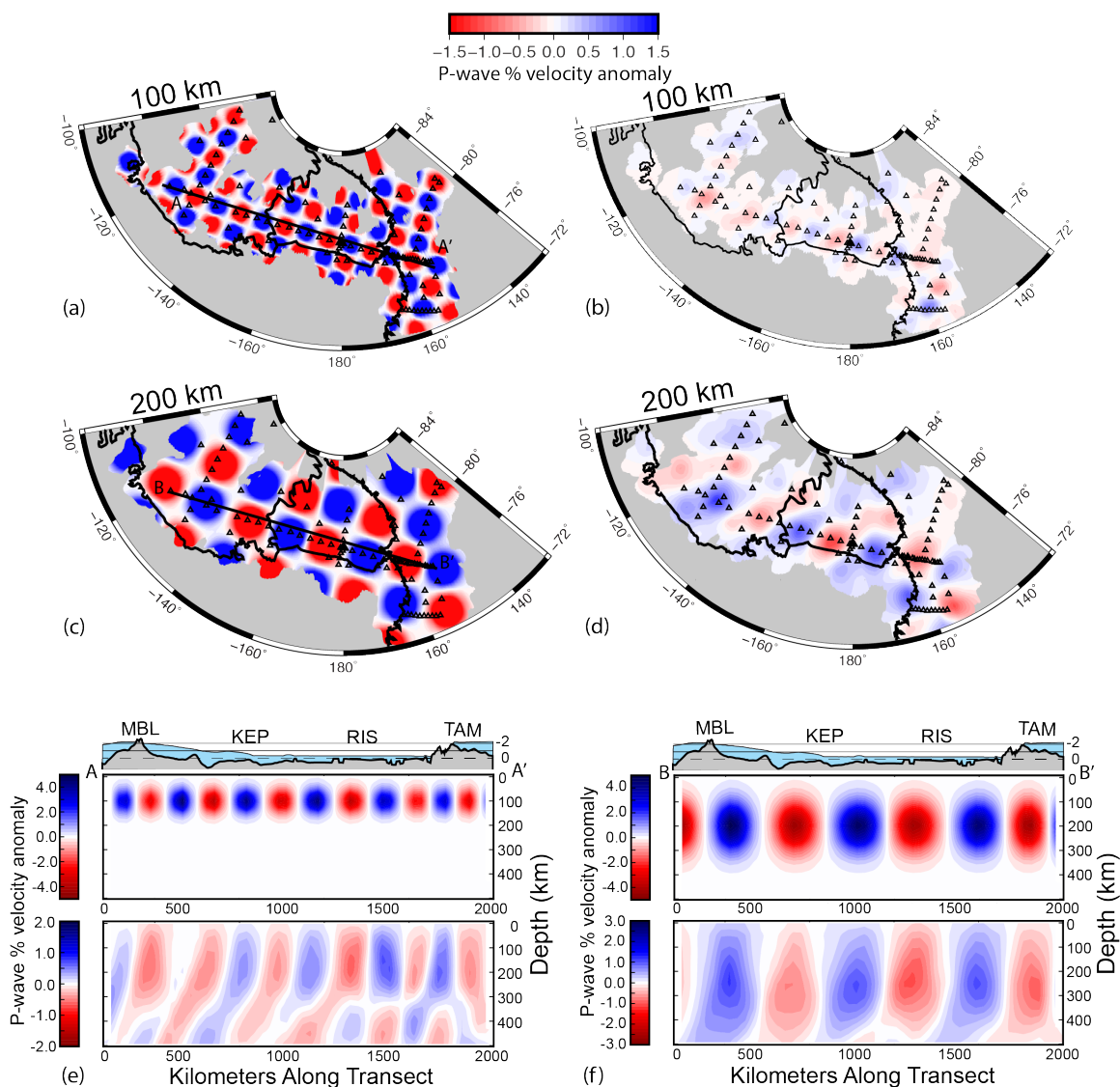


Figure 2-4: a) Input synthetic model with 50 km radius Gaussian tapered spheres with peak amplitude of $\pm 5\%$ centered at 100 km depth. b) Corresponding recovered structure from (a). c) Input synthetic model with 100 km radius Gaussian tapered spheres centered at 200 km depth. d) Corresponding recovered structure from (c). e) Cross-section along A-A' (Fig. 2-3) showing 50 km radius sphere input model from (a) on the upper panel and recovered model from (b) on the lower panel. f) Cross-section along B-B' (Fig. 2-3) showing 100 km radius input model from (c) on the upper panel and recovered model from (d) on the lower panel.

Tabular Body Tests

To further evaluate the resolution of anomalies in our model, we created a number of synthetic velocity structures, or tabular bodies, along profile A-A' (Fig. 2-5). As with the checkerboard tests, we calculated associated travel-times and inverted them to assess recoverability. For each tabular body, we specify a peak amplitude of the velocity anomaly, its length along-strike, its width, and the depth range over which the velocity anomaly tapers off, which we derive to be consistent with our final model (Fig. 2-3 e). Figure 2-5 shows the corresponding tabular body input model as well as the recovered structure obtained from inverting the synthetic travel-times using the same parameterization as in our actual model. The recovered amplitudes of the tabular velocity anomalies are between 20-25% of the input, except for the anomaly beneath RI. Since the recovered synthetic anomaly beneath Ross Island is smaller than Anomaly G in our model (Fig. 2-3), this low V_p structure must either be relatively stronger or broader than our input tabular body. The recovered synthetic structure in the tabular test already extends deeper than Anomaly G in our model, suggesting a stronger, rather than a deeper, structure is present beneath Ross Island when compared to our input tabular body (Fig. 2-5). Another difference between the pattern in the recovered tabular test and our final model occurs within EA, where the recovered high V_p anomaly does not extend as deep as Anomaly I in our model (Figs. 2-3 and 2-5). This suggests that the input synthetic anomaly was either too weak or too shallow, implying that the peak amplitude of the fast structure beneath EA could be deeper than 100 km, the depth of the input body. Overall, the vertical smearing in the recovered synthetic tabular test is very similar to the model (Fig. 2-5 c).

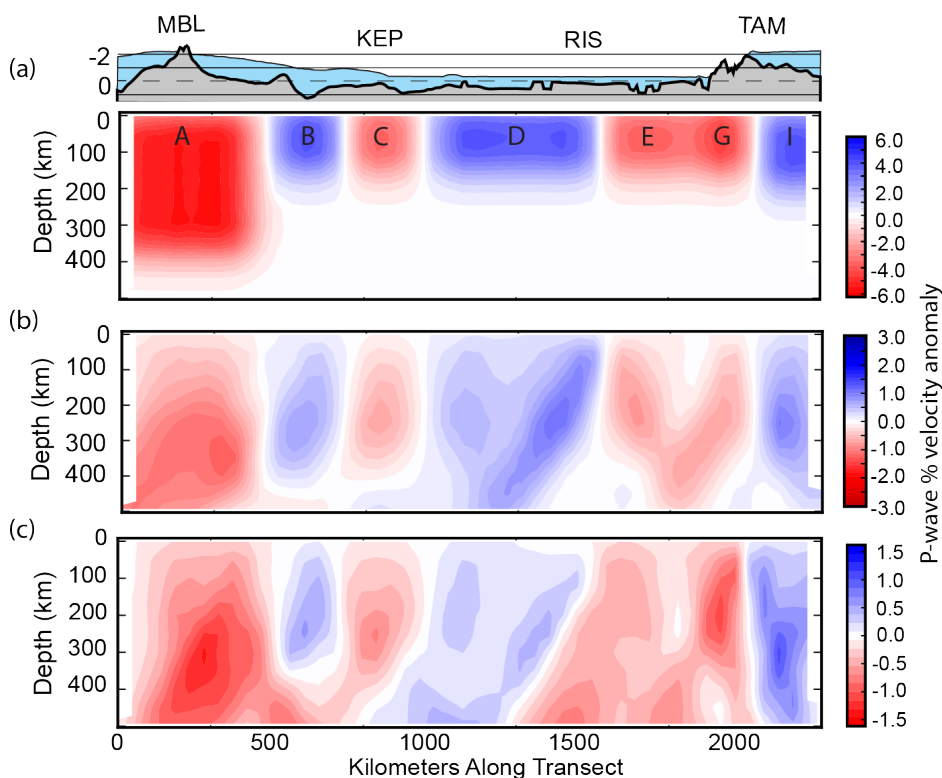


Figure 2-5: a) Cross-section A-A' (Fig. 2-3) with tabular body synthetic input. Anomalies discussed in the text are labeled. All input anomalies have $\pm 4\%$ peak amplitudes, except for the 50 km wide body directly beneath RI corresponding to Anomaly G, which has a -6% peak amplitude. b) Corresponding recovered anomalies. c) Cross-section through the actual model for comparison (same as Fig. 2-3 e).

Discussion

The wide aperture of the combined seismic networks used in this study allows us to investigate relative variations in upper mantle structure beneath several Antarctic terranes within a single consistently referenced model. Previous regional body wave studies have identified heterogeneity within various regions in Antarctica, but making comparisons between terranes greater than 1000 km apart relative to the same model mean has been difficult. With the RIS/DRIS network connecting seismic stations in the TAM region to those in MBL and the

central WARS, we can assess relative V_P variations between these provinces while simultaneously focusing on the previously poorly resolved region of the RSE. Additionally, by including data from seismic stations in regions adjacent to the RSE, we can evaluate the consistency of our model with previous tomographic results (Watson et al., 2006; Brenn et al., 2017; Lawrence et al., 2016; Hansen et al., 2014; Lloyd et al., 2016; Heeszel et al., 2016; Shen et al., 2018).

Given the results of the tabular body tests (Fig. 2-5) and the limited resolution of our model below 300 km, we believe that anomalies present in our model, with the exception of Anomaly A in MBL (Fig. 2-3), arise primarily from heterogeneous structure within the lithospheric mantle. However, heterogeneous upper mantle structure may not necessarily be confined to the mantle lithosphere and could in some places extend below the lithosphere into the asthenosphere. While difficult to constrain, recent shear wave velocity models of West Antarctica (Shen et al., 2018; Heeszel et al., 2016) indicate a lithospheric thickness of ≥ 80 -100 km for much of the RSE, 70-100 km for the central WARS, and 60-100 km in MBL.

Because a primary influence on V_P variability in the upper mantle is temperature (Cammarano et al., 2003), and, because geochemical analyses of Cenozoic mafic alkaline volcanic rocks across WA reveal a fairly narrow range of isotopic and trace element compositions (Hole and LeMasurier, 1994), we attribute the velocity variations in our model mainly to relative temperature differences. For calculations, we use the V_P temperature sensitivity ($\pm 0.75\%$ per 100 K) from Cammarano et al. (2003). Because of the ~ 20 -25% amplitude recovery in our resolution tests (see Figs. 2-4 and 2-5), this approach yields minimum temperature change estimates. Beneath MBL, however, water content in the upper mantle may be elevated compared to other areas of WA due to a history of subduction in the region (LaMasurier et al., 2016). Elevated pH_2O could suppress the mantle solidus and lead to greater amounts of partial melt in the upper

mantle. If this is happening, then upper mantle temperatures beneath MBL may not be as elevated as elsewhere in WA where we also image V_P anomalies of -1.5%.

Our model reveals heterogeneous structure not clearly seen in previous tomographic models of WA (*e.g.*, Anomalies B and C). Faster V_P in Anomaly B underlying the Ford Ranges separates Anomaly C in the KEP area from Anomaly A beneath MBL, previously imaged and interpreted by Lloyd et al. (2015) and Hansen et al. (2014) as thermally perturbed upper mantle (Figs. 1 and 3b). Along cross-section A-A' (Fig. 2-3 e), it is difficult to ascertain whether Anomaly C connects to Anomaly A at depth because of the limited depth resolution of the model. The tabular body test (Fig. 2-5) suggests little to no connectivity between these two anomalies; however, there is some indication of connectivity between Anomalies A and C south of Anomaly B in the 400 km depth slice (Fig. 2-3 d). Given the geographic proximity of Anomalies A and C, it seems possible that the mantle beneath the KEP could be influenced by thermochemically perturbed upper mantle structure beneath MBL but separated by less perturbed lithosphere beneath the Ford Ranges. While there are no known Cenozoic volcanoes in the KEP, the high geothermal heat flux (Maule et al., 2005) and seismic activity (Winberry and Anandakrishnan, 2003) found there could be linked to magmatic processes occurring in the region (Fig. 2-1 b).

Within the RSE (Fig. 2-1), our model shows a clear dichotomy between faster, cooler upper mantle structure in the eastern RSE (Anomaly D) and slower, warmer upper mantle structure in the western RSE (Anomaly E; Fig. 2-3 e). The difference in V_P between these regions indicates at least a ~100 K change in upper mantle temperature across the RSE. We attribute the temperature difference to the presence of colder and/or thicker lithosphere under the eastern RSE, in which case there may have been little, if any, Cenozoic reheating of the lithosphere in that part of the WARS. Spatially, Anomaly D correlates with the location of the Eastern Basin (Fig. 2-1 c) (*e.g.*, Decesari et al., 2007; Davey and Brancolini, 1995; Brancolini, et al., 1995; and Granot et al., 2013), and extends beneath the interior of the Ross Ice Shelf (Fig. 2-6).

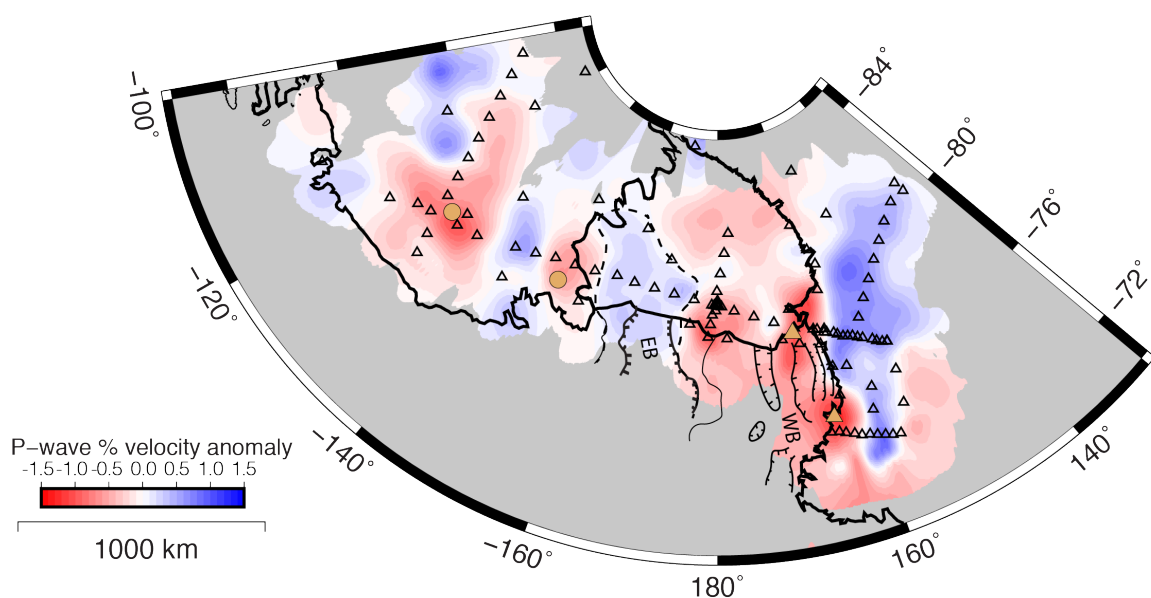


Figure 2-6: Depth slice at 200 km through P-wave model (same as Fig. 2-3 b), showing the eastern (EB) and western (WB) portions of the RSE, the locations of seismicity in MBL (orange circles), active volcanoes (orange triangles) and seismic stations (open triangles).

In the western RSE, our model shows three very low V_P anomalies (-1.25%; Anomalies F, G, and H) within a broader region of low V_P (-0.75%; Anomaly E). Anomalies G and H, which underlie the two active volcanoes Mt. Erebus and Mt. Melbourne along the TAM front (Fig. 2-6), are similar to the low velocity regions beneath these volcanoes imaged by Brenn et al. (2017). Anomaly F is located in the central RSE (Fig. 2-3). Bifurcation of the input anomaly in the tabular body test (Fig. 2-5) suggests that Anomaly F could simply be part of the broader Anomaly E. The dense cluster of DRIS stations in the central Ross Ice Shelf significantly increases ray density in this portion of the model (Fig. A-4). Several iterations of the model were run with various station configurations, including the removal of all of the DRIS stations. While the bifurcated velocity pattern still persists when the DRIS stations are removed, the amplitude of Anomaly F approaches that of Anomaly E (Fig. A-4), indicating that Anomaly F could be an artefact from high ray density. Because of that, we argue that the western RSE is primarily

characterized by a broad region (~500 km wide) of thermally perturbed lithosphere ($V_P \sim -0.75\%$), with focused lower V_P regions (-1.5%) along the TAM front under areas of recent magmatism (*i.e.*, Anomalies G and H). The larger reduction (-1.5%) in P-wave velocities beneath these volcanoes suggests a further ~100 K increase in upper mantle temperatures and/or the presence of partial melt, which is consistent with the suggestion by Brenn et al. (2017) that partial melt, either within the lithosphere or ponded at its base, could be present.

The east-to-west change in the RSE upper mantle temperature, from the cooler temperatures beneath the Eastern Basin to the warmer temperatures beneath the western basins, to the even warmer temperatures and/or partially melted rock beneath Mt Erebus and Mt. Melbourne can be interpreted as evidence of multiple phases of rifting in the WARS. Broad-scale rifting during the Late Cretaceous led to many of the extensional structures present in the RSE (*i.e.*, thinned crust and rift basins; Siddoway, 2008). The relatively low seismic velocities across the western portion of the RSE, compared to the eastern portion, can be explained by a Paleogene phase of extension that resulted in thinning and warming of the lithosphere (Anomaly E) and regional transtensional deformation (Faccenna et al., 2008). An even younger (Neogene-Present) period of extension focused along the TAM front, associated with the development of the Terror Rift and alkaline shield volcanism, may have followed that phase of rifting, and was possibly influenced by plume processes in the mantle (Phillips et al. 2018; and references therein).

Away from the KEP and RSE, our model shows similar structures to previous body wave tomography models. For instance, Watson et al. (2006) showed a 2-3% change in V_P over a lateral distance of ~50-100 km, demarcating the sharp boundary between the EA and WA lithosphere. Further to the north beneath Northern Victoria Land, Brenn et al. (2017) modeled a similar velocity contrast (~2-3%) beneath the TAM, marking an abrupt transition from WA to EA lithosphere. In the vicinity of RI, our model shows a ~2% horizontal V_P contrast directly beneath

the TAM. Therefore, with the addition of data collected from within the RSE, the strong boundary in upper mantle velocity structure is maintained, but with a slightly lower magnitude.

Beneath the Wilkes Subglacial Basin, both our model and the Brenn et al. (2017) model show a velocity reduction in the upper mantle. Although the Wilkes Subglacial Basin is near the edge of the model, where model resolution degrades, we believe that the imaged velocity reduction is sufficiently resolved to suggest the presence of thermally perturbed lithospheric mantle and/or lithosphere that is thinner than the surrounding areas of EA, as suggested by aeromagnetic surveys (Ferraccioli et al. 2009).

In MBL, Lloyd et al. (2015) reported a 2-3% V_P variation in the upper mantle structure between the Executive Committee Range and adjacent areas, and attributed the velocity variation to a ~ 150 K thermal anomaly. However, as noted previously, if the MBL upper mantle has a higher water content than elsewhere in WA, the velocity variation could also be caused by an increase in partial melt and a thermal anomaly less than $+150$ K. Hansen et al. (2014) also imaged a similar upper mantle low velocity structure beneath MBL. The location and amplitude of Anomaly A (Fig. 2-3) is consistent with the Lloyd et al. (2015) and Hansen et al. (2014) models. When taking vertical smearing into account, Anomaly A could be confined to the upper 400 km; however, given the limited vertical resolution in our model, we are not able to tightly constrain the depth extent of the anomaly. The tabular body test (Fig. 2-5) mimics Anomaly A in our model and requires that the input structure extend to at least 300 km depth, suggesting that the structure beneath MBL is present at sublithospheric depths but may not extend as deep as the transition zone. This suggestion is consistent with Emry et al. (2015), who show little evidence for thinning of the transition zone beneath MBL.

Our model is also broadly consistent with previous regional surface wave models that image upper mantle structure beneath MBL and the RSE. For example, both Heeszel et al. (2016) and Shen et al. (2018) show faster shear-wave velocities ($V_S \sim 4.5$ - 4.6 km/s) down to ~ 80 km

depth within the Eastern Basin and parts of the central WARS, with slower V_S (~ 4.2 - 4.3 km/s) at similar depths beneath the western basins. The variation in upper mantle V_S between the eastern and western basins is consistent with the variation in V_P in our model. The Shen et al. (2018) model also suggests slower upper mantle velocities beneath the KEP than the Ford Ranges at 80 km depth; however, the broad sensitivity kernels, wide Fresnel zones, and long wavelengths (~ 300 km) of Rayleigh waves sensitive to structure at ~ 100 km depth (Yang and Forsyth, 2006) make the KEP structure difficult to constrain using surface waves.

The heterogeneity in upper mantle V_P structure ($\sim \pm 0.75\%$) present throughout much of WA has important implications for surface heat flow and upper mantle viscosity. The variability in the velocity structure suggests at least ± 100 K variations in upper mantle temperatures over length scales of 100 km and more. In steady state, lithospheric mantle temperature anomalies of ± 100 K would lead to $\sim \pm 10$ mW/m² changes in surface heat flow. While this variability does not account for the large range in point estimates of heat flow across WA (*e.g.*, 69 mW/m², Engelhardt et al., 2004; 115 mW/m², Morin et al., 2010; and 285 mW/m², Fisher et al., 2015), it is consistent with the variability in regional heat flow (Schroeder et al., 2014; Maule et al., 2005; Pollard et al., 2005), and may be large enough to affect basal ice conditions. With regard to mantle viscosity, O'Donnell et al. (2017) showed that ± 100 K temperature variations in the upper mantle can result in viscosity changes of ~ 2 orders of magnitude, which Barletta et al. (2018) argued can have a significant impact on ice sheet stability by influencing glacial isostatic adjustment.

Summary and Conclusions

A P-wave model of upper mantle structure, extending from MBL and the WARS into EA, has been generated by inverting 32,454 relative P-wave travel-time residuals recorded by the

RIS/DRIS and other Antarctic seismic networks. The model has improved resolution over previously published body wave models for the region, particularly within the RSE sector of the WARS.

Within the RSE, our model shows a clear dichotomy in the upper mantle velocity structure between the eastern and western basins. Seismically fast upper mantle beneath the eastern RSE correlates with the Eastern Basin and suggests that the lithosphere in this region may not have been reheated by Cenozoic rifting. Seismically slow upper mantle over a ~500 km-wide area beneath the western RSE transitions to more focused, ~100 km-wide regions of even slower velocity along the TAM front beneath Mt. Erebus and Mt. Melbourne. We attributed the broad slow velocity region beneath the western RSE to Paleogene rifting, while the focused slower velocity anomalies under Mt. Erebus and Mt. Melbourne could be associated with a Neogene-Present phase of rifting and/or plume activity, which created the Terror Rift. Within the Ford Ranges and KEP in western MBL, we also see significant lateral variability in upper mantle velocity structure ($\pm 0.50\%$) over distances of only a few hundred km.

The heterogeneity in upper mantle velocity structure in our model, assuming no significant variation in composition, represents changes in temperature of at least 100 K over distances of hundreds of km. This variability in mantle temperature could lead to surface heat flow variations of $\sim \pm 10 \text{ mW/m}^2$ and 10^2 Pa-s changes in mantle viscosity, which could influence the stability of the West Antarctic Ice Sheet by affecting basal ice conditions and glacial isostatic adjustment.

Chapter 3

Seismic architecture of the upper mantle beneath southern Africa from body wave tomography

Abstract

In this study, we have developed new P-wave and S-wave velocity models of the upper mantle beneath southern Africa using data recorded on seismic stations spanning the entire southern African subcontinent. Teleseismic P-wave and S-wave travel-time data were recorded on 278 stations belonging to 8 temporary and 6 permanent networks between 1998 and 2018. In total, 13,326 unique P-wave travel-times and 9,242 unique S-wave travel-times were utilized from 693 earthquakes.

Many parts of our study area have been imaged previously by body wave tomography, and, in these regions, anomalies in our models are consistent with anomalies imaged in the previous studies. These anomalies include a large region with higher than average velocity in the upper 400 km beneath the Kaapvaal Craton, Limpopo Belt, Zimbabwe Craton, and portions of the Okwa and Magondi Belts, together referred to as the Kalahari Craton. In the northern Kaapvaal Craton, there is a region of lower than average velocity beneath the Bushveld Complex that extends to the northwest into central Botswana. The Namaqua-Natal Belt has regions with slightly higher than average velocity and regions with slightly lower than average velocity, while the upper 400 km beneath the Cape Fold Belt is lower than average. A deep-seated low velocity zone (LVZ) is present beneath central Zambia and the velocity of upper 400 km beneath the Okavango Rift Zone is lower than average.

Outside of the footprint of previous body wave tomography studies, our models reveal several new anomalies. Almost the entire upper mantle beneath the Damara Belt in northern

Namibia has lower than average velocity in the upper 400 km. Resolution tests show that this anomaly can be explained by thinner mobile belt lithosphere (~130 km) compared to thicker, cratonic lithosphere (~200 km) to the south. Along the northwestern coast of Namibia, beneath the Etendeka Flood Basalt Province, velocity structure is higher than average suggesting that the lithosphere in this region is relatively thick and/or depleted. The Rehoboth Province is underlain by velocity structure that is higher than average, which may reflect the presence of the Maltehohe Microcraton. Beneath the Mozambique Belt in central Mozambique, there is a deep-seated LVZ in the upper 600 km of the mantle that cannot be fully explained by differences in lithospheric thickness alone. North of this LVZ, beneath the Southern Irumide Belt, a high velocity anomaly is present in the upper mantle and could represent the Proterozoic Niassa Craton.

Resolution tests show that the velocity anomalies beneath the Damara Belt can be explained by lithospheric architecture alone and that there is no indication of excess temperatures in the upper mantle. Therefore, the source of buoyancy support for the Southern African Plateau, at least beneath the Damara Belt, must reside in the mid-to-lower mantle. Beneath the Mozambique Belt in central Mozambique, however, differences in lithospheric thickness alone cannot fully account for the LVZ imaged in our model. This suggests that the upper mantle beneath this part of southern Africa may be thermally perturbed. A plausible source for this thermal anomaly could be the African Superplume structure in the lower mantle beneath southern Africa.

Introduction

Many studies of the tectonic framework of southern Africa, extending back more than 50 years, have strongly influenced our understanding of Earth history and continental evolution (e.g.,

Brock, 1959; Anhaeusser, 1973; Kröner, 1977). However, the upper mantle structure in much of southern Africa remains poorly imaged, especially beneath Proterozoic mobile belts, limiting our understanding of African lithospheric evolution. To date, there have been few seismological studies of southern Africa using data from seismic networks deployed in Proterozoic terranes away from the Archean blocks which form the core of the southern African shield.

Recent deployments of broadband seismic instruments in regions peripheral to the greater Kalahari Craton (Fig. 3-1) provide an opportunity to image the upper mantle beneath southern Africa more broadly than in previous studies. In this investigation, we utilize data from several new seismic networks, as well as data from previous seismic networks, to develop P-wave and S-wave velocity models spanning most of southern Africa. Our models reveal upper mantle structure beneath terranes not imaged previously by body wave tomography, as well as improved resolution of upper mantle structure in previously studied regions of southern Africa.

Because of the limited seismic data coverage in the Proterozoic regions of southern Africa, one of the outstanding questions about southern Africa is the origin of plateau uplift. The southern African Plateau is ~1 km high and spans the subcontinent (Fig. 3-1) (Nyblade and Robinson, 1994). To the north, in eastern Africa, thermally perturbed upper mantle, revealed by seismic images, provides the buoyant support for the ~1 km high East Africa Plateau (Fishwick and Bastow, 2011). Our results enable us to address whether the upper mantle surrounding the thick cratonic lithosphere of the Kalahari Craton has been thermally perturbed to the same extent as upper mantle in eastern Africa, providing a source of buoyancy (i.e., uplift) for the Southern Africa Plateau.

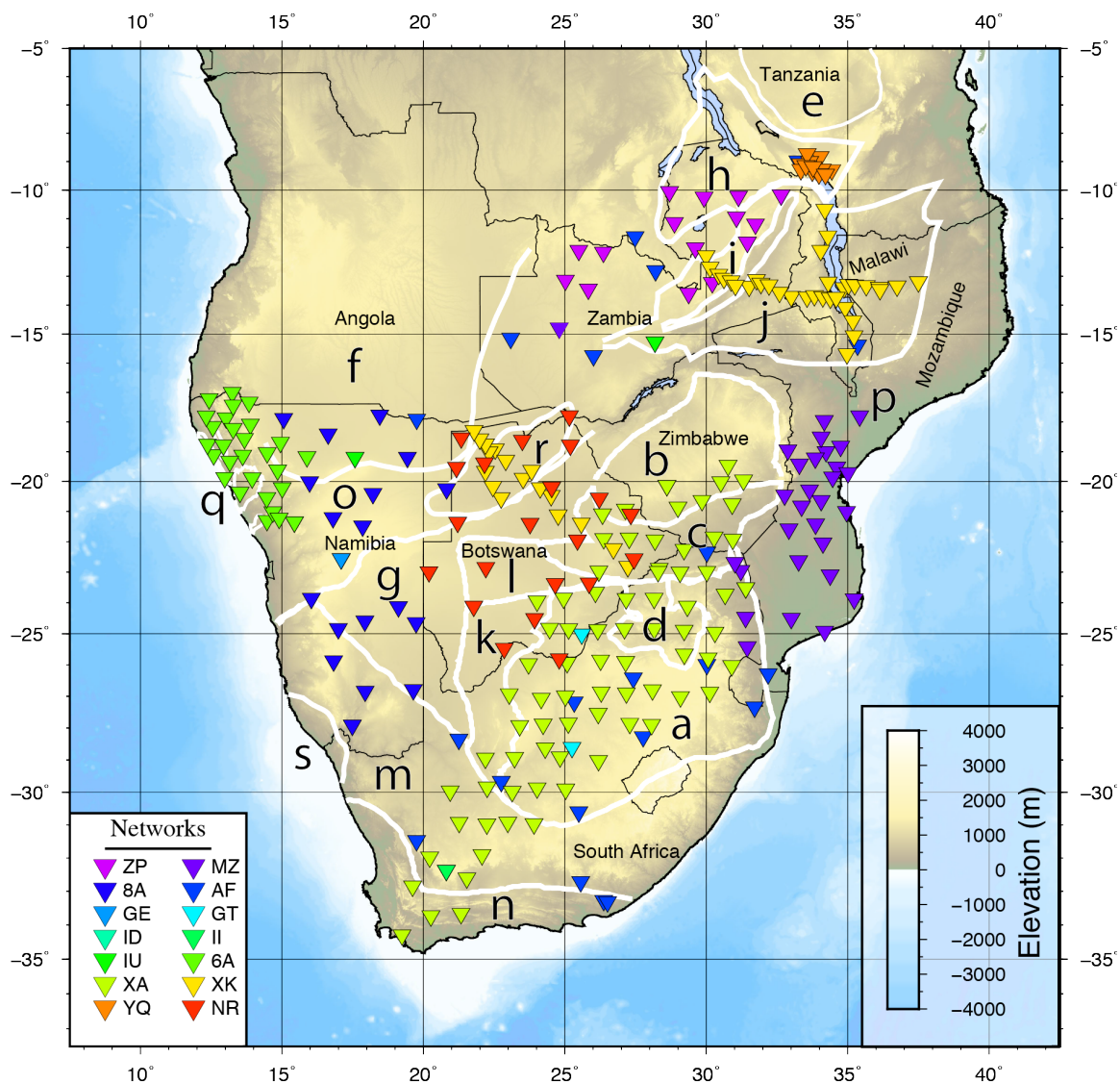


Figure 3-1: Topographic map showing tectonic boundaries in southern Africa and locations of seismic stations used in the P-wave and S-wave models. Tectonic terranes are labeled as (a) Kaapvaal Craton; (b) Zimbabwe Craton; (c) Limpopo Belt; (d) Bushveld Igneous Province; (e) Tanzania Craton; (f) Congo Craton/Angolan Shield; (g) Rehoboth Province; (h) Bangweulu Block; (i) Irumide Belt; (j) Southern Irumide Belt; (k) Kheis Belt; (l) Okwa Terrane; (m) Namaqua-Natal Belt; (n) Cape Fold Belt; (o) Damara Belt; (p) Mozambique Belt; (q) Etendeka Flood Basalt Province; (r) Okavango Rift; (s) Gariiep Belt (Begg et al., 2009; Frimmel and Frank, 1998). Elevations from GEBCO (Weatherall et al., 2015).

Tectonic Background

The thermotectonic and compositional structure of the crust and upper mantle in southern Africa ranges in age from Mesoarchean to Cenozoic, and its tectonic development can be described in three primary phases (Fig. 3-1). 1) A patchwork of Archean cratons comprises a large portion of southern Africa. 2) The cratons are surrounded and welded together by Proterozoic mobile belts accreted and deformed during major orogenic cycles (e.g., Pan-African). 3) During the Phanerozoic, the Precambrian tectonic framework experienced Mesozoic rifting, flood basalt volcanism, and Cenozoic rifting extending south and southwest from the East African Rift System (EARS).

There are three primary Archean cratonic blocks within the study area. The Kaapvaal and Zimbabwe cratons are both granite-greenstone terranes that formed in the Mesoarchean to Neoarchean (de Wit et al., 1992). The Limpopo Belt is a Neoarchean deformational belt that formed during the collision of the Kaapvaal and Zimbabwe Cratons. Combined, these terranes are commonly referred to as the greater Kalahari Craton (de Wit et al., 1992). The last major tectonothermal events to affect these terranes were the emplacement of the Great Dike in the Zimbabwe Craton c. 2.6 Ga (Jelsma and Dirks, 2002) and formation of the layered Bushveld igneous complex (Fig. 3-1) within the Kaapvaal Craton c. 2.1 Ga (Olsson et al., 2010). Extending from southern Angola northward to Cameroon is the expansive Congo Craton and Angolan Shield, a complex amalgamation of Archean and Proterozoic crustal blocks, much of which is covered by Phanerozoic sediments (Batumike et al., 2009).

The Proterozoic history of southern Africa is marked by continental growth through the accretion of numerous terranes to the Archean cratons (Fig. 3-1). During the Paleoproterozoic, the Kheis Belt and Rehoboth Province accreted to the western margin of the Kaapvaal Craton (Hanson, 2003). This was followed by the formation of the Namaqua-Natal Mobile Belt

surrounding the southern margin of the Kaapvaal Craton and Rehoboth Province c. 1.2-1.0 Ga (Cornell et al., 2006). To the northwest of the Kalahari Craton, orogenic events led to the accretion of the Magondi and Okwa terranes c. 2.0 Ga (McCourt et al., 2001). In the northernmost portion of the study area, the Irumide and Southern Irumide Belts formed in the Mesoproterozoic c. 1.3-1.0 Ga, however, some evidence suggests that these belts were extensively reworked during the Neoproterozoic Pan-African orogeny (Hanson, 2003). There are two major Pan-African orogens within the study area. In the eastern portion of the study area, the Mozambique Belt formed during the final assembly of Gondwana c. 841-632 Ma (Hanson, 2003). In the northwest, the Damara-Ghanzi-Chobe Belt (hereafter referred to as the Damara Belt) formed during the collision of the greater Kalahari Craton and the Congo Craton c. 580-500 Ma. During roughly the same time, small portions of the western margin of the Namaqua-Natal Belt were overprinted with the accretion of the Gariep Belt in southern Namibia (Eglington, 2006). The youngest deformational belt (c. 250 Ma) in the study region, the Cape Fold Belt, is located along the southern tip of the African continent and resulted from subduction and arc deformation at or near the southern margin of Gondwana (Hansma et al., 2016; Begg et al., 2009).

Several tectonic events punctuate the Phanerozoic history of southern Africa. The initial break-up of Gondwana coincides with Karoo rifting across southern Africa and the formation of the c. 180 Ma Karoo large igneous province in southern Africa (Duncan et al., 1997). The c. 130 Ma Etendeka large igneous province in northwestern Namibia is also associated with the breakup of Gondwana, as well as the Tristan Da Cunha mantle plume (Bauer et al., 2000). The Cenozoic is marked by the formation of incipient rifts linked to the southward extension of the EARS. Seismically active fault systems point to incipient rifting within the Okavango Rift Zone in northern Botswana (Scholz et al., 1976), and seismically active fault systems also define the southernmost extension of the Western Branch of the EARS in central Mozambique (Fonseca et al., 2014).

The topography of southern Africa is characterized by a ~1 km-high plateau (Fig. 3-1), which together with the East African Plateau and the southeastern Atlantic Basin, comprise the African Superswell (Nyblade and Robinson, 1994). The buoyancy support for, timing, and rate of uplift of the Southern African Plateau is not well understood (Nyblade and Sleep, 2003). Several mechanisms have been proposed for the buoyancy support of the region, including density anomalies and flow associated with the African Superplume in the mid-to-lower mantle (Forte et al., 2010; Gurnis et al., 2000; Lithgow-Bertollini and Silver, 1998) and thermally perturbed upper mantle beneath the Kalahari Craton (Li and Burke, 2004).

Previous Geophysical Studies

The crustal structure of southern Africa has been extensively examined using a range of seismological observations and models. Crustal thickness in the Kalahari Craton, and more recently portions of the surrounding Proterozoic terranes, has been characterized by receiver function analysis (Nguuri et al., 2001; James et al., 2001; Nair et al., 2006; Yu et al., 2015; Fadel et al., 2018), through joint inversion of receiver functions and surface wave dispersion measurements (Kachingwe et al., 2015; Kgawane et al., 2009), by modeling regional seismic phases (Wright et al., 2003; Kwadiba et al., 2003), and by inverting satellite gravity data (Tugume et al., 2013). Consistent across all of these studies is a range of crustal thicknesses of ~34-50 km within the cratonic blocks and the surrounding mobile belts.

There have been several previous body wave tomographic investigations in southern Africa, all capitalizing on expanding data coverage in the region. The earliest of these models were constructed using data from the Southern African Seismic Experiment (SASE; https://doi.org/10.7914/SN/XA_1997) deployment within the Kalahari Craton (Fig. 3-1). Fouch et al. (2004) modeled $\pm 2\%$ P-wave and $\pm 2.4\%$ S-wave velocity variations within the Kalahari

Craton, Namaqua-Natal Belt, and Cape Fold Belt. High velocity anomalies demarcating the cratonic region were present to depths of ≥ 300 km, and a low velocity anomaly was imaged beneath the Bushveld Complex. More recently, finite-frequency tomography has been applied to the SASE dataset, yielding similar results (Youssof et al., 2015). Yu et al. (2015), in one of the first regional-scale body wave tomography studies focusing on structure outside of the Kalahari Craton, obtained models showing a low velocity (-1-2% V_p) anomaly beneath the Okavango Rift Zone in northern Botswana, extending to a depth of ≤ 300 km.

Expanding on these previous studies, Ortiz et al. (2019) incorporated data from the SASE dataset with data from two other seismic networks in Botswana and Zambia, obtaining P-wave and S-wave velocity models for a broader region of southern Africa. Their model shows a similar degree of wave speed variability as previous models within the Kalahari Craton, Namaqua-Natal Belt, Cape Fold Belt, and the Okavango Rift Zone. However, their model shows a clear boundary between higher velocities to the south of the Damara Belt and lower velocities to the north, and they interpreted this boundary as the northern edge of the greater Kalahari craton. The Ortiz et al. (2019) model also shows a continuation of the LVZ beneath the Bushveld Complex extending to the northwest into central Botswana.

Further to the north in southern Zambia, the Ortiz et al. (2019) model shows a deep-seated low velocity anomaly extending at least as deep as the mantle transition zone. This feature was first reported by Mulibo and Nyblade (2013a; 2013b), who argued that the anomaly extends across the transition zone connecting the low velocity structure in the lower mantle beneath southern Africa, which has often been referred to as the African Superplume, with thermally perturbed upper mantle beneath eastern Africa. Because the Ortiz et al. (2019) model only imaged upper mantle structure beneath the portion of the Damara Belt in northern Botswana and southern Zambia, they were not able to determine if the LVZ under the Okavango Rift Zone extended to the southwest beneath the Damara Belt in northern Namibia.

Complementing the body wave models are many surface wave investigations of the upper mantle beneath southern Africa. Continental-scale velocity models of Africa have been developed by inverting teleseismic fundamental and/or higher mode Rayleigh and Love wave measurements (e.g., Ritsema and Heijst, 2000; Sebai et al., 2006; Prestley et al., 2008; Pasyanos and Nyblade, 2007; Chevrot and Zhao, 2007; Fishwick, 2010; Raveloson et al., 2015) and modeling the ambient noise wavefield (Emry et al., 2019). Consistent across these models is the presence of a higher velocity upper mantle lid underlying cratonic portions of the subcontinent and lower shear velocity structure in the upper mantle beneath the mobile belts.

Regional-scale models have also been developed for the study area from surface wave measurements using a variety of techniques. Two-plane wave approximations of teleseismic Rayleigh waves (Forsyth and Li, 2005) have been useful in characterizing structure in regions with higher-density station deployments in both southern (Li and Li, 2015; Adams and Nyblade, 2011; Li and Burke, 2006) and eastern (O'Donnell et al., 2013; Adams et al., 2012) Africa. Helmholtz tomography using interstation measurements of teleseismic fundamental mode Rayleigh wave phase dispersion has yielded comparable results, again capitalizing on regions with dense, temporary station arrays (Adams et al., 2018, Accardo et al., 2018). The regional-scale models provide better constrained estimates of lithospheric thickness beneath the Kalahari Craton and adjacent mobile belts than do body wave models, and have also imaged low velocity structure in the upper mantle correlating with rifting and volcanism in East Africa. Magnetotelluric methods have provided independent models of lithospheric structure for southern Africa and parts of eastern Africa. Across the Kaapvaal Craton, Damara Belt, and into the Congo Craton, Khoza et al. (2013) modeled much thinner lithosphere beneath the Damara Belt (~180 km) than beneath the cratonic blocks (~250 km). Other MT studies have modeled ~160 km thick lithosphere beneath the Damara Belt (Muller et al., 2009) and ~180 km thick lithosphere beneath the Okavango Rift Zone (Miensopust et al., 2011). Within the Rehoboth Province, Muller et al.

(2009) modeled ~180 km thick lithosphere. To the north, in eastern Zambia and southern Malawi, Sarafian et al. (2018) reported a deep resistive lithospheric root (~250 km) beneath the Southern Irumide Belt which may be interpreted as a remnant of the pre-Mesoproterozoic Niassa Craton.

Data and Methods

Figure 3-1 shows the location of seismic stations from which seismic waveform data were gathered. This investigation was motivated by new recordings from the 2015-2018 deployment of 19 AfricaArray broadband seismometers in Namibia (https://doi.org/10.7914/SN/ZP_2007). To complement these data, and provide a check on consistency with previous studies, we used additional data from 13 temporary and permanent networks in southern Africa covering a timespan from 1997-2018. To broaden the coverage within Namibia, we included observations from 28 terrestrial stations deployed from 2010-2012 as part of the Walpass network (<https://doi.org/10.14470/1N134371>). Also in Namibia, and contemporaneous with both the AfricaArray-Namibia and Walpass networks, a single station from the GEOFON network in Windhoek was included (<https://doi.org/10.14470/TR560404>). A total of 38 stations were utilized from Botswana, including 17 stations from the Seismic Arrays for African Rift Initiation (SAFARI) network in Botswana (https://doi.org/10.7914/SN/XK_2012) and 21 stations from the Botswana Network of Autonomously Recording Seismographs (<https://doi.org/10.7914/SN/NR>). In the northern portion of our model, we included data from 33 stations deployed with the SAFARI project, 16 stations from the AfricaArray Uganda/Tanzania deployment (https://doi.org/10.7914/SN/ZP_2007), 14 stations from the Study of Extension and Magmatism in Malawi and Tanzania (SEGMeNT) deployment (https://doi.org/10.7914/SN/YQ_2013), and a few additional AfricaArray (https://doi.org/10.7914/SN/ZP_2007) and permanent stations (<https://doi.org/10.7914/SN/II>,

<https://doi.org/10.7914/SN/IU>, <https://doi.org/10.7914/SN/GT>, <https://doi.org/10.7914/SN/ID>). In Mozambique, 24 stations from the Mozambique Rift Tomography (MOZART) project provided valuable observations from the eastern-most portion of the region. Covering a large area, from Zimbabwe to South Africa, 75 stations from the SASE network deployed from 1997-1999 provided useful data (https://doi.org/10.7914/SN/XA_1997), in addition to 5 permanent stations (<http://www.fdsn.org/networks/detail/IU>; <https://doi.org/10.7914/SN/II>; <https://doi.org/10.7914/SN/GT>; <https://geofon.gfz-potsdam.de/doi/network/GE>; and <https://doi.org/10.7914/SN/ID>). In total, 278 stations were used for the P-wave model and 273 stations were used to develop the S-wave model (Table E-1).

For this investigation, we used P and S phase body wave arrival times from $M > 5.5$ teleseismic earthquakes at epicentral distances ranging from $30\text{-}90^\circ$ for P-waves, and $30\text{-}84^\circ$ for S-wave measurements. Waveforms were first corrected for instrument response and then filtered between 0.5-5 Hz for P-waves and 0.04-2 Hz for S-waves. Processed P- and S-wave arrivals were picked on a prominent phase before applying a multi-channel cross-correlation approach to measure more precise relative arrival times for events with 3 or more manual picks (VanDecar and Crosson, 1990). This technique uses a three-second window for P-waves and a 12-second window for S-waves around the initial picks, and cross-correlates all combinations of traces for each event to find the ensemble correlation maxima. Events with cross-correlations values >0.70 for all combinations of windowed traces were used, resulting in a total of 693 useful events for P-waves and 493 events for S-waves (Fig. B-1). These events yielded 13,326 unique P-wave and 9,242 unique S-wave travel-time measurements.

The model domain consists of a series of intersecting knots spaced relative to lines of latitude and longitude, and in kilometers with depth. The model ranges from 37.5°S to 7.5°S with knots spaced at 0.5° increments, and from 8.0°E to 41°E with knots also at 0.5° intervals. Knots were spaced at 20 km intervals between the surface and 200 km depth, knots were spaced at 33

km intervals between 200-700 km depth, knots were spaced at 50 km intervals from 700-1400 km depth, and knots were spaced at 100 km intervals from 1400-1600 km depth. In total, the model includes 59 knots in latitude, 65 knots in longitude and 42 knots in depth.

To solve for a 3D velocity model, we first numerically calculated partial derivatives at each knot with respect to slowness using perturbations from the 1D IASP91 model (Kennett and Engdahl, 1991). Initial travel-time residuals were calculated by ray tracing event-receiver paths through the 1D model. During the inversion process, we iteratively updated the 3D model using a conjugate-gradient approach through reducing the travel-time residuals until changes in the model made insignificant (<0.01 s) changes to the RMS travel-time residual (VanDecar, 1991). The inversion simultaneously solves for 3D changes to the velocity model, station static terms, and event relocation terms. Station static terms account for structure in the shallowest part of the model where there is limited ray crossing, while the event relocation terms absorb location error and structure outside of the model domain. To prevent overfitting of the data, the inversion was regularized by smoothing and damping terms. Smoothing and damping weights were chosen using a tradeoff curve, providing 96.7% rms travel-time residual reduction in the P-wave model and 86.5% travel-time residual reduction in the S-wave model (Fig. B-2). We note that the large reduction in the rms travel-time residual is a product of the contributions from the event relocation terms (median = 7.3 s), the station static terms (Fig. B-8), and the model velocity perturbations (Fig. 3-2).

Model Results

Model results are shown in Figure 3-2, where P-wave velocities (V_p) and S-wave velocities (V_s) are shown as percent variations. Velocity structure in the top 50 km of the models is not shown because ray crossing is limited at these depths. We note that the actual mean of the

model could have shifted from the starting model during the inversion process and so absolute velocities are unconstrained. To first-order, the P-wave and S-wave models are similar and anomalies in both models are well correlated with terranes shown in Figure 3-2. In the following paragraphs, we summarize the velocity structure in both models.

The Kaapvaal Craton is the largest high wave speed anomaly (Anomaly A) in the models. In the upper 600 km, the average P-wave velocity in this region is $\sim+0.5\%$, with a maximum of $+0.8\%$ at 300 km depth. The S-wave velocity is also higher than average across the Kaapvaal Craton in the upper 600 km, with a peak anomalous velocity of $+1.0\%$ at 400 km depth. There is, however, a region in the upper 400-500 km within the northern Kaapvaal Craton, with lower than average V_p and V_s (Anomaly B) that correlates with the Bushveld Igneous Complex and extends to the northwest into central Botswana. The Zimbabwe Craton has higher than average velocity (V_p and V_s) in the west and lower than average velocities in the east bordering the Mozambique Belt.

In the southern part of the model, both the P- and S-wave velocities are lower than average beneath the Cape Fold Belt. North of that, beneath the Namaqua-Natal Belt, the velocities are near average in the top 300 km, except in a region directly south of the Kheis Belt, where both the P-wave and S-wave velocities are higher than average between 300-500 km depth. Within the Kheis Belt, the P-wave and S-wave models have average velocity structure. To the west of the Kheis Belt, there is strong similarity between the P-wave and S-wave models beneath the Rehoboth Province, with an increasing trend in velocities in the upper 400 km from -0.25% V_p and -0.5% V_s in the west to $+0.3-0.4\%$ V_p and $+0.5\%$ V_s in the east of the terrane.

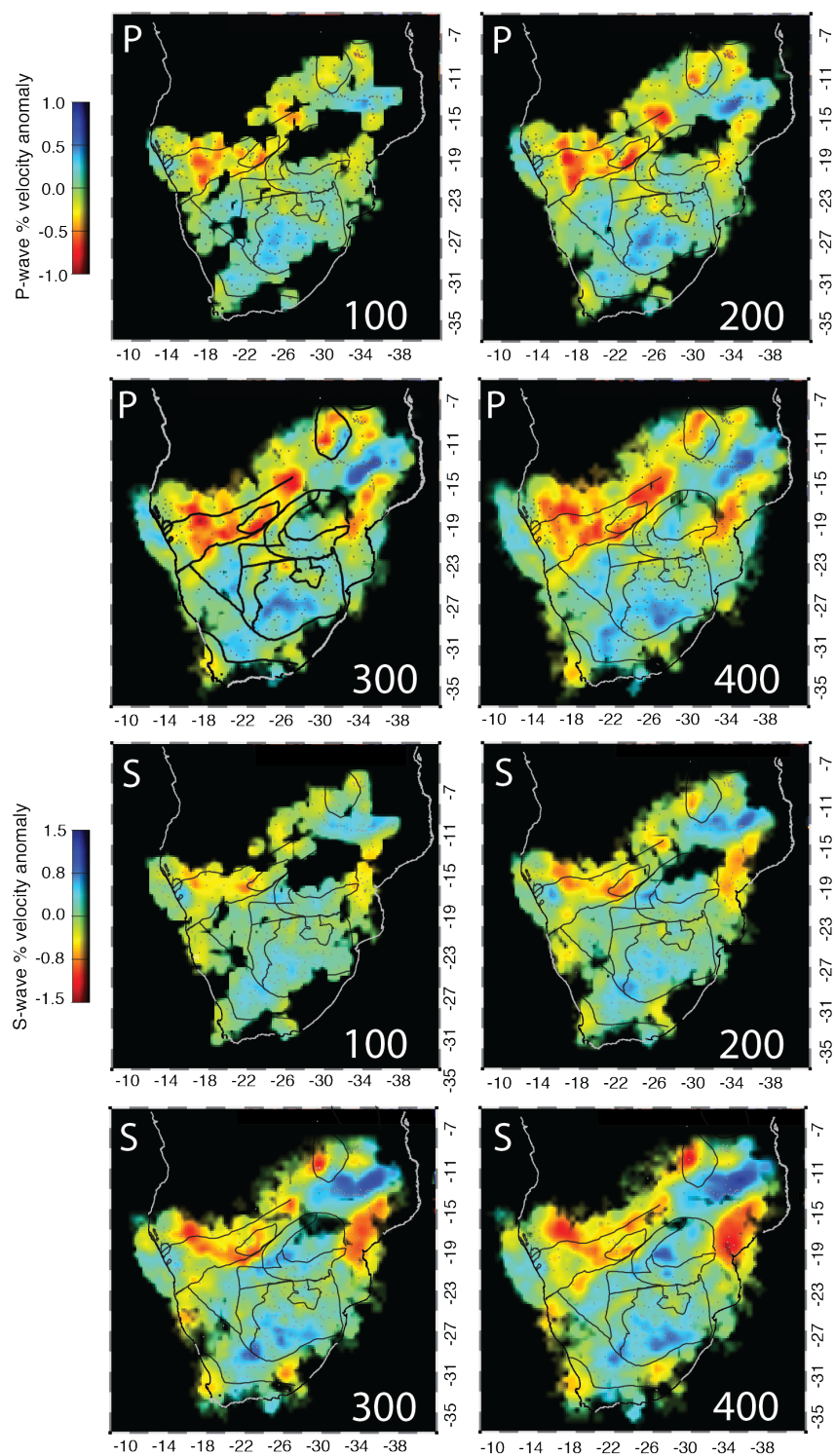


Figure 3-2: Horizontal cross-sections through the P-wave (top) and S-wave (bottom) models at 100 km increments. Tectonic boundaries correspond to those in Fig. 3-1.

Within the Damara Belt, a low wave speed anomaly is present throughout most of the upper mantle (Anomalies C, D, and F). There is a consistent -0.3% to -0.75% V_p and -0.5 to -0.8% V_s anomaly in the upper ~400 km of the model, with the lowest velocities (-0.75% V_p and -0.9% V_s) at ~250 km depth. The low velocity anomaly extends northward beneath southern Angola at depths greater than 400 km. There is a strong spatial correlation between the southern edge of the LVZ and the boundary between the Damara Belt and Rehoboth Province (Fig. 3-2).

Within the Okavango Rift Zone, both the P-wave and S-wave models have lower than average velocities (-1.0%, Anomaly C) in the upper 400 km. This structure is separated by a region of higher velocities from the LVZ extending to the NW from the Bushveld Complex into central Botswana. Unlike the majority of the Damara Belt, beneath the Etendeka Flood Basalt Province in northwestern Namibia, P-wave velocities are +0.25% in the top 200 km of the mantle (Anomaly G). Velocities beneath this region are also higher than average in the S-wave model, with a peak amplitude of +0.7% at 200 km depth.

Beneath the Damara Belt in southcentral Zambia, the P-wave model has a low wave speed anomaly extending to a depth of ≥ 800 km (Anomaly D), with maximum negative velocities of -0.9% between 600-800 km depth (Fig. 3-3 a,d). This feature is also present in the S-wave model, but slightly weaker with a peak negative anomaly of -0.7%. The deepest structure present in both the P-wave and S-wave models is a large low wave speed anomaly at ≥ 700 km depth (Anomaly K) centered beneath the Irumide Belt in northern Zambia with peak V_p of -0.5% and V_s of -1.5% V_s .

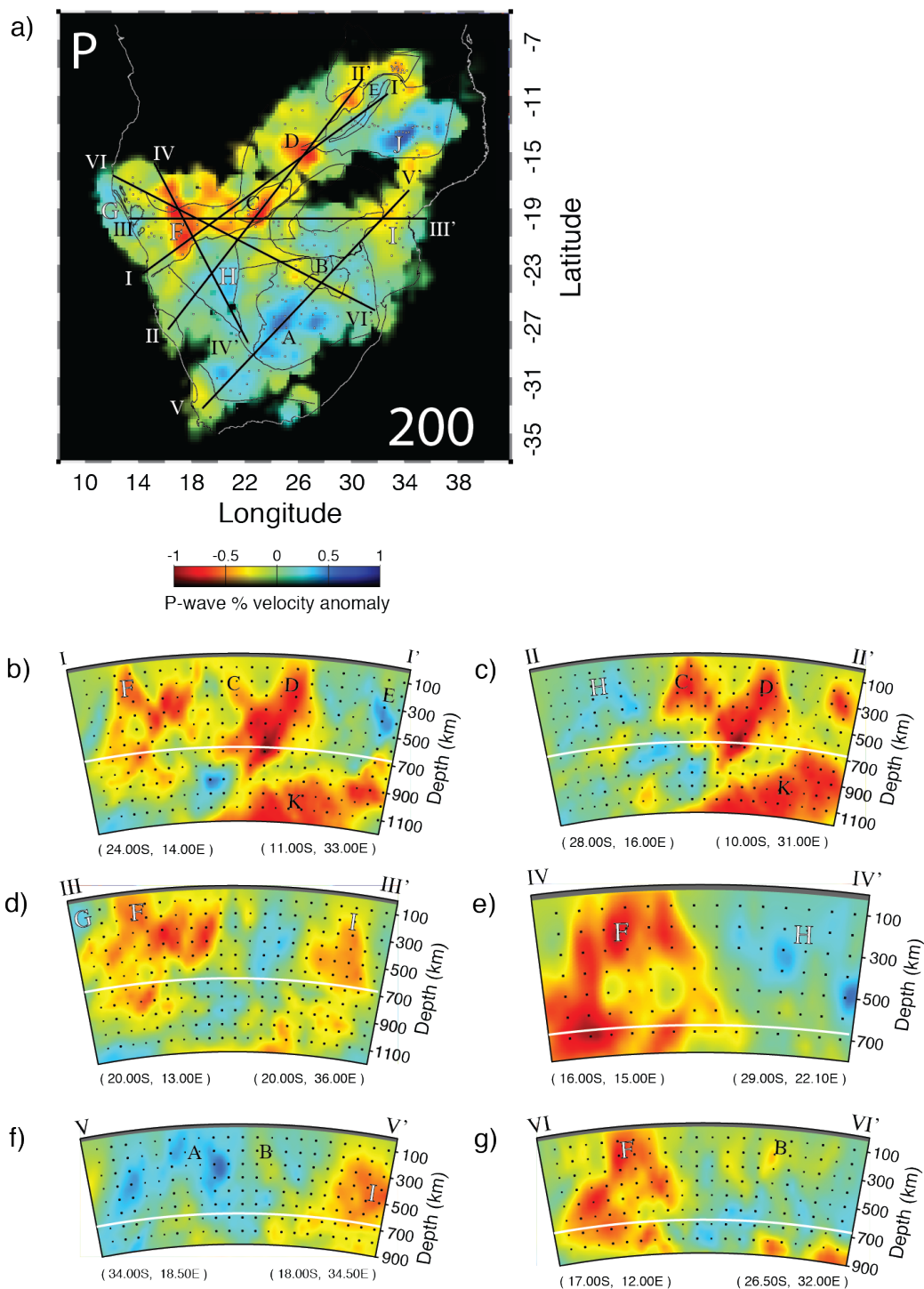


Figure 3-3: a) Horizontal cross-section through the P-wave model at 200 km depth. Major velocity anomalies are labeled A-K. Surface intersections of cross-sections I-VI are shown with black line segments. Tectonic boundaries are the same as those in Fig. 3-1. b-g) Vertical cross-sections taken through the P-wave model corresponding to black line segments from (a). Intersected anomalies (A-K) are labeled.

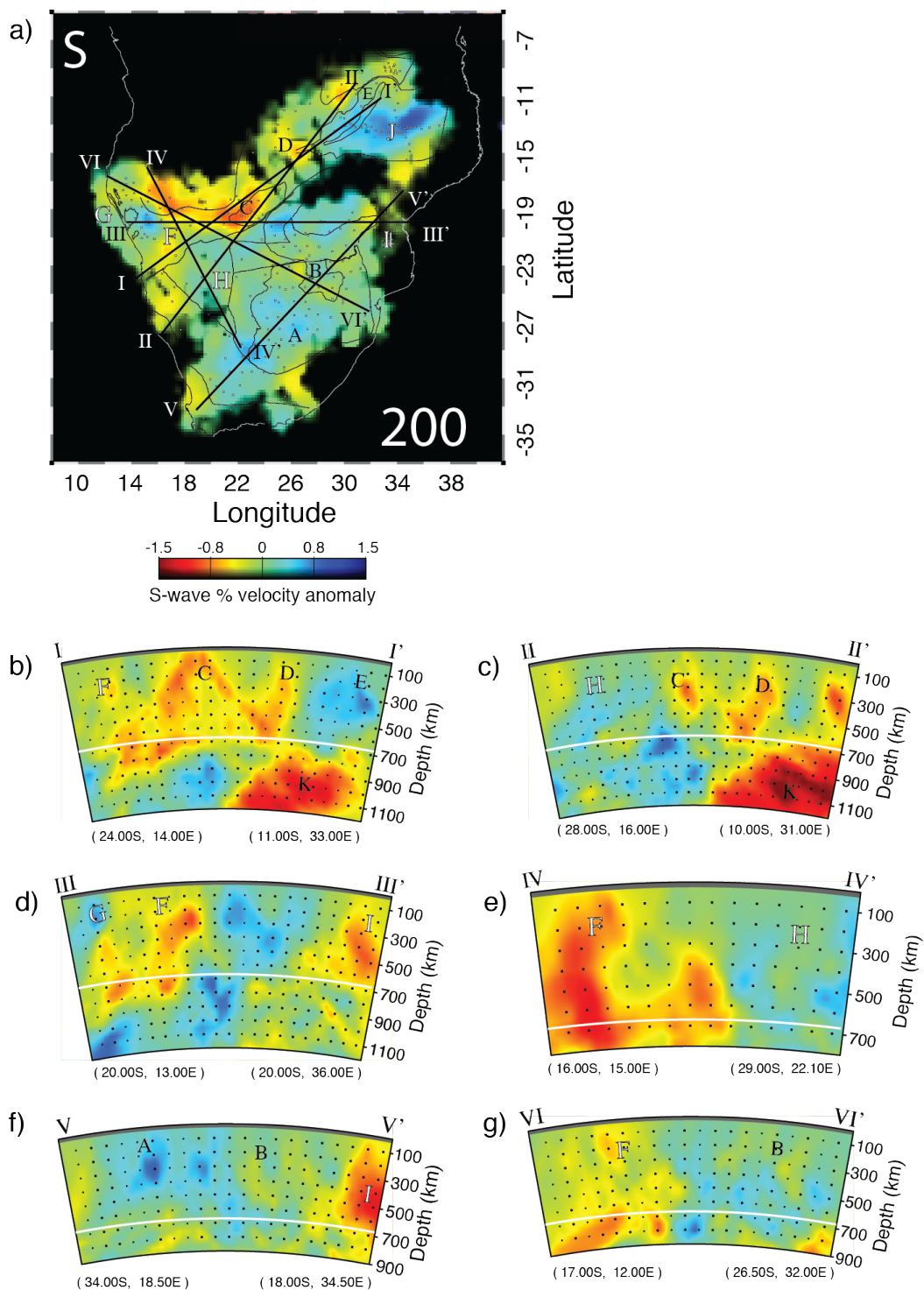


Figure 3-4: a) Horizontal cross-section through the S-wave model at 200 km depth. Major velocity anomalies are labeled A-K. Surface intersections of cross-sections I-VI are shown with black line segments. Tectonic boundaries are the same as those in Fig. 3-1. b-g) Vertical cross-sections taken through the S-wave model corresponding to black line segments from (a). Intersected anomalies (A-K) are labeled.

In the upper mantle between 200-450 km depth, at the edge of resolution in the models, the western side of the Bangweulu Block is characterized by lower than average velocities. There is a high velocity anomaly (Anomaly E) in the upper 400 km along the eastern side of the Bangweulu Block and beneath the Irumide Belt. Within the Malawi Rift, beneath the northern edge of Lake Malawi, a focused negative velocity anomaly (-0.5% V_p and -0.25% V_s) is present in the upper 300 km. Within the Southern Irumide Belt, the P-wave model has a high velocity anomaly with peak velocities of +1.0% between depths of 400-500 km (Anomaly J). In the S-wave model, Anomaly J and Anomaly E merge together to form a broad high velocity anomaly covering a wide portion of the Irumide Belt and Southern Irumide Belt. South of the Irumide Belt. Beneath the Mozambique Belt in central Mozambique, both models have a low wave speed anomaly (Anomaly I) that extends to ≥ 700 km depth. The P-wave model has a peak anomalous velocity of -0.7% and the S-wave model has a peak anomalous velocity of -0.8%. In southern Mozambique, both the P- and S-wave models have $< 0.3\%$ variation from average.

Model Resolution

To assess the vertical and horizontal resolution of our P- and S-wave velocity models, we inverted a series of synthetic datasets to check for recoverability. To evaluate the spatial resolution of the model at various depth ranges, we raytraced our event and station geometry through checkerboard models to create synthetic travel-time datasets. A normal distribution of noise was added to the synthetic travel-times, centered at the origin with a standard deviation of 0.04 sec for the P-waves and 0.10 sec for the S-waves. Checkerboard models were designed with alternating high and low anomalies. The spherical anomalies had a Gaussian shape, with a maximum anomalous amplitude of $\pm 5\%$ and a width at half maximum of 200 km. The centers of the anomalies were spaced 3° apart in both latitude and longitude. The results of the checkerboard

inversion are shown in Figure 3-4 and Figure 3-5. Regions with the recovered pattern are considered areas in which the model is able to resolve structures 200-300 km-wide or wider. Only larger-scale features are considered interpretable in regions where the pattern is not recovered. Below 600 km depth, we increased the half-max width of the anomalies to 400 km to test for recoverability of structures between 400-600 km in diameter or greater (Fig. B-5 and B-6).

Regions of high recoverability are in areas with denser station coverage (i.e., northern Namibia, Botswana, within Kalahari craton, and Malawi). While recovery of input structures centered at 100 km depth is limited in most regions, at deeper depths the checkerboard pattern is better resolved, particularly at depths ≥ 200 km. From 200-600 km depths, the P-wave model has good recoverability of the ~ 200 km-wide input anomalies in most regions with the exception of northern Zimbabwe, Mozambique, and the southern coast of South Africa. Recovery of the larger checkerboards at ≥ 700 km depth is largely ubiquitous, with some northeast-southwest smearing. Vertical smearing, common in body wave tomography, is evident, with checkerboard structures stretching ~ 150 km upward and downward (Fig. 3-5 e-f, Fig. 3-6 e-f). Overall, the pattern of recovery in the S-wave model is similar to the P-wave model, with the best recovery in the Kalahari region, Namibia, and southern Tanzania. The maximum amplitude of the input anomalies is not fully recovered, with both the P-wave and S-wave models recovering ~ 30 -40% of the input amplitudes, but this is consistent with other body wave tomography studies using relative travel-time residuals (Bastow et al., 2005). Station static terms are removed during the inversion to account for structure at < 50 km depth, where ray crossing is minimal. The distribution of station static term is centered at the origin with a standard deviation of 0.36 s. Negative station static terms are generally correlated with regions of Archean crust and positive station static terms are correlated with regions outside of the Kalahari Craton (Fig. B-8).

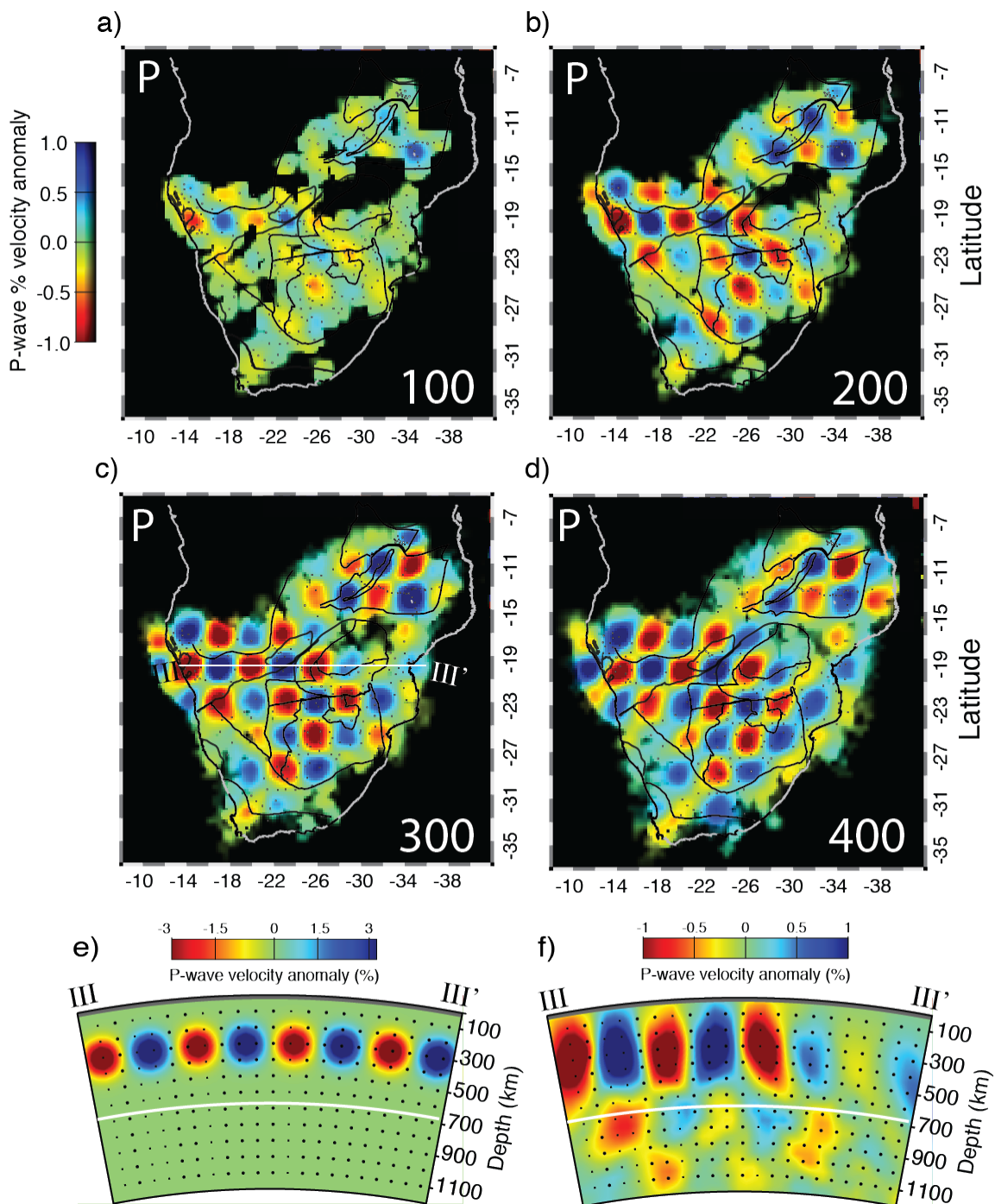


Figure 3-5: a-d) Horizontal cross-sections of P-wave checkerboard resolution tests taken at 100 km intervals (100-400 km). Intersection line of the III vertical cross-section shown in (e) and (f) is labeled in (c). e) Synthetic P-wave velocity model used to create an artificial travel-time dataset. Inversion results from this synthetic dataset are shown in (c) and (f).

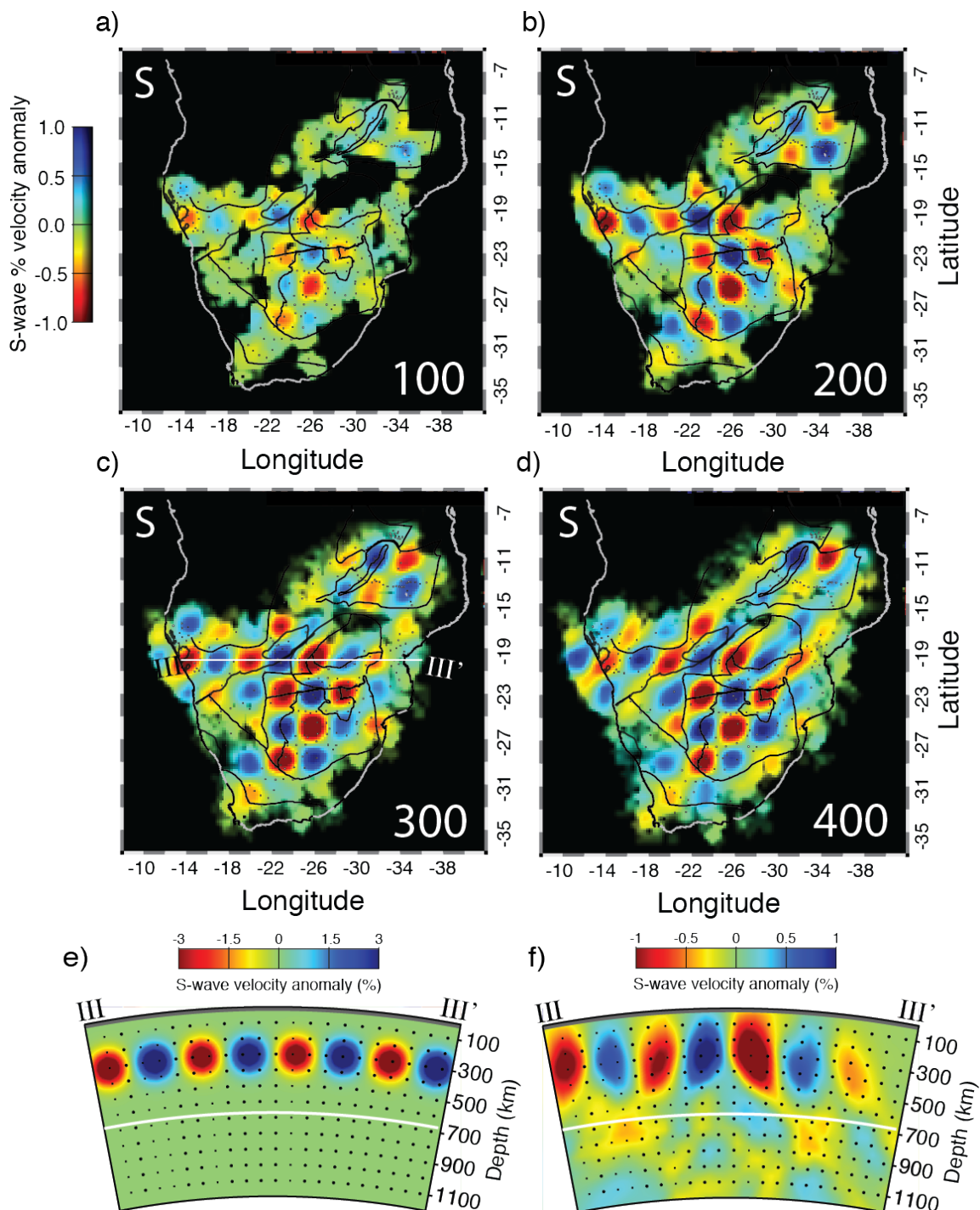


Figure 3-6: a-d) Horizontal cross-sections of S-wave checkerboard resolution tests taken at 100 km intervals (100-400 km). Intersection line of the III vertical cross-section shown in (e) and (f) is labeled in (c). e) Synthetic S-wave velocity model used to create an artificial travel-time dataset. Inversion results from this synthetic dataset are shown in (c) and (f).

Discussion

To summarize, the P-wave and S-wave models are similar and show several anomalies in the upper mantle seen in previous body wave velocity models, as well as several new anomalies. We first discuss anomalies that have been imaged previously using body wave data (as reviewed in Previous Geophysical Studies), and then discuss the new anomalies.

Anomalies Reported in Previous Studies

The Kaapvaal Craton has higher than average seismic velocity in the upper 400 km (Anomaly A). Beneath the Kaapvaal Craton, a region of lower than average velocity (Anomaly B) is present under the Bushveld Complex, and extends to the northwest into central Botswana. Within the Damara Belt in northwestern Botswana, there is a lower than average velocity anomaly (Anomaly C) in the upper mantle under the Okavango Rift Zone. To the south of the Kaapvaal Craton, in the Namaqua-Natal Belt, the velocity structure is nearly average, with slightly lower than average velocity structure near the Gariiep Belt and slightly higher than average velocity in a region directly south of the Kheis Belt. There is a low velocity anomaly beneath the Cape Fold Belt.

As argued by Ortiz et al. (2019), the higher than average upper mantle velocities beneath the greater Kalahari Craton, including portions of the Okwa Terrane and Magondi Belt, are consistent with the northwestern boundary of the Kalahari Craton aligning with the southern boundary of the Damara Belt in Northern Botswana and Namibia. Also noted by Ortiz et al. (2019), the LVZ (Anomaly B) beneath the Bushveld Complex and central Botswana indicates that the upper mantle in this region may have been altered during the Bushveld or other igneous events.

Beneath the Damara Belt in southern and central Zambia, our models also show a previously reported, deep-seated upper mantle LVZ (Anomaly D). Our model is consistent with the Mulibo and Nyblade (2013b) study, which attributed this anomaly to a whole-mantle, thermochemical structure (i.e., the African Superplume) extending from the lower mantle beneath southern Africa to the upper mantle beneath eastern Africa.

At the northmost edge of our model, the western side of the Bangweulu Block is characterized by lower than average velocities in the upper 400 km. To the southeast, beneath the eastern side of the Bangweulu Block and the Irumide Belt, higher than average velocities (Anomaly E) are imaged in the upper 400 km. This transition between lower than average velocities beneath the western side of the Bangweulu Block and higher than average velocities beneath the Irumide Belt was seen previously in the body wave tomography model reported by Mulibo and Nyblade (2013a).

New Anomalies

Outside of the footprint of previous body wave investigations, our models reveal several new anomalies (G, F, H, I, and J; Fig. 3-3). To further investigate the spatial extent and depth of these anomalies, several tabular body resolution tests have been conducted. For these tests, we created velocity anomalies to represent a difference in lithospheric thickness between cratonic and non-cratonic lithosphere. Parameters for the test were based on the depth of the conductive lithosphere determined using mantle xenolith data (Janney et al., 2010). The base of the non-cratonic lithosphere is set to 130 km and the base of the thick, cratonic lithosphere is set to 200 km depth. The velocity anomaly within the 130-200 km depth range was constrained by the difference in temperature between the cratonic geotherm and the mantle adiabat at the depth midpoint between the base of the cratonic lithosphere and the base of the non-cratonic lithosphere

(i.e. 165 km). The temperature difference ($\sim 250\text{-}300\text{ K}$) was then converted to P-wave and S-wave velocities following the velocity-temperature relationships in Cammarano et al (2003). This yielded velocity differences of $\sim 2.25\%$ for V_p and $\sim 3.9\%$ for V_s . However, because mantle velocity is also sensitive to the difference in composition between cratonic lithosphere and sublithospheric mantle (Jordan, 1979; Schutt and Lesher, 2010), P-wave velocity anomalies of 4% and S-wave velocity anomalies of 6% were used for tabular body models. These anomalies are within the range of synthetic tests used by other studies for southern and eastern Africa (Ortiz et al., 2019; Grijavla et al., 2018; Mulibo and Nyblade, 2013). Below we discuss the new anomalies along with the results of the tabular body resolution tests.

Within the Damara Belt, previously imaged low velocity anomalies beneath the Okavango Rift Zone and southern Zambia (C and D; Yu et al., 2017; Ortiz et al., 2019) are part of a more extensive low velocity anomaly, including a large area within the Damara Belt in northern Namibia (Anomaly F). Anomaly F is present in both the P-wave and S-wave models in the upper 400 km, extending from the central Namibian coast to the Okavango Rift Zone, and further northeastward into the LVZ in Zambia. Almost the entire upper mantle beneath the Damara Belt has lower than average velocity structure. The southern boundary of Anomaly F tracks remarkably well with the mapped southern boundary of the Damara Belt within Namibia and Botswana (Fig. 3-3 a), providing additional strong evidence that the Damara Belt marks the northwestern boundary of the greater Kalahari Craton.

To test the source of this broad anomaly beneath the Damara Belt, we constructed a tabular body resolution test to determine the effect that differences in lithospheric thickness alone would have on the models. Along the length of the Damara Belt, we placed a tabular body to represent thinner ($\sim 130\text{ km}$) lithosphere compared to thicker ($\sim 200\text{ km}$) cratonic lithosphere to the south (Fig. 3-7 and 3-8). Results of the synthetic tests show that within the Damara Belt, from the Okavango Rift Zone to the Namibian coast, thin lithosphere (i.e., 130 km vs 200 km), can

account for the majority of the anomalous velocity in the model, with the exception of a deeper anomaly in northernmost Namibia. In the tabular body test, the lower velocities associated with the thinner lithosphere smear to depths of ~700 km (Fig. 3-5 b-c). A contrast in lithospheric thickness of ~70 km in this region is consistent with continental-scale surface wave tomography studies (e.g., Emry et al., 2019; Fishwick, 2010; Priestley et al., 2006). We therefore interpret the LVZ in the upper 400 km along the Damara Belt (Anomaly F), including the LVZ beneath the Okavango Rift Zone, as a difference in lithospheric thickness compared to the greater Kalahari Craton, and argue that thermochemically perturbed sublithospheric mantle, associated with the African Superplume, is not necessary to explain Anomaly F.

In both the P-wave and S-wave models, at depths between 500-800 km, there is a low velocity anomaly beneath northernmost Namibia and southern Angola (Figs. 3-3 e, B-3, B-4). This anomaly lies along the northern edge of our model where resolution degrades. A low velocity anomaly in the upper mantle beneath southern Angola has been imaged using ambient noise tomography (Emry et al., 2019). Emry et al. (2019) linked this anomaly to the Angola (Bie) Dome. Our results suggest that the upper mantle anomaly imaged by Emry et al. (2019) under the Bie Dome may extend as deep as the transition zone over a fairly large area.

Anomaly F in the Damara Belt has an abrupt western boundary in northern Namibia. West of Anomaly F, there is a high velocity Anomaly G (Fig. 3-2) in the upper 300 km along the northwestern Namibian coast. Receiver functions from this region have been interpreted to show a thick, depleted lithospheric mantle beneath the Etendeka Flood Basalt Province (Yuan et al., 2017). Depleted and thicker lithosphere under this region, resulting from the interaction with the Tristan Da Cunha mantle plume, would result in an upper mantle with seismic velocities that are higher than the surrounding region. Following Yuan et al. (2017), we therefore attribute the higher velocities of Anomaly F to localized lithospheric alteration from the Etendeka magmatic

event. An alternative interpretation, however, is that a lobe of thick cratonic lithosphere extends south from the Angolan shield beneath northwestern Namibia.

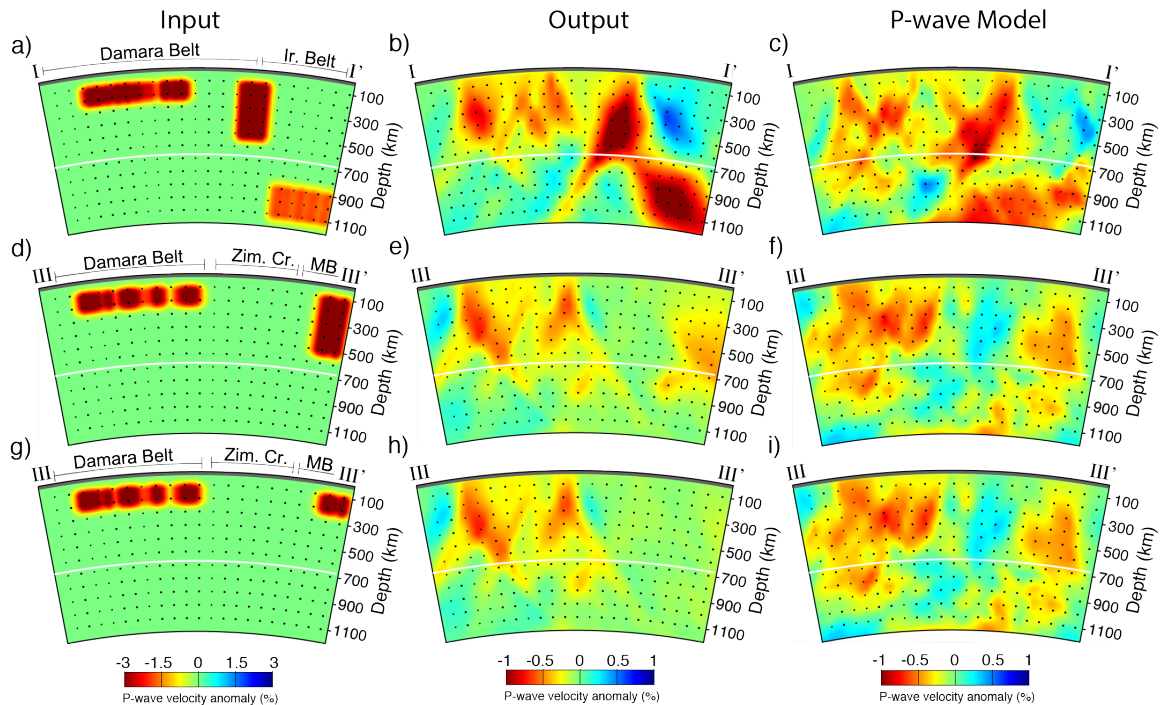


Figure 3-7: a) Tabular body model used to create a synthetic P-wave travel-time dataset representing relatively thin lithosphere (~ 130 km) adjacent to relatively thick lithosphere (~ 200 km) beneath the Damara Belt (left of image). A deeper synthetic anomaly is required beneath central Zambia (center of image) and a lower mantle anomaly is required beneath northern Zambia (right of image). The vertical cross-section is taken along transect I (Fig. 3-3). Damara Belt, Zimbabwe Craton (Zim. Cr.) and Mozambique Belt (MB) are labeled. b) Inversion results from synthetic travel-times created using model (a). All anomalies are smeared vertically. c) Vertical cross-section from P-wave model taken along transect I (see Fig. 3-3). d) The same initial tabular model at (a) with a relatively thin lithosphere beneath northern Namibia (left of image) and a deeper low velocity anomaly beneath Mozambique (right of figure). The vertical cross-section is taken along transect III (Fig. 3-3).

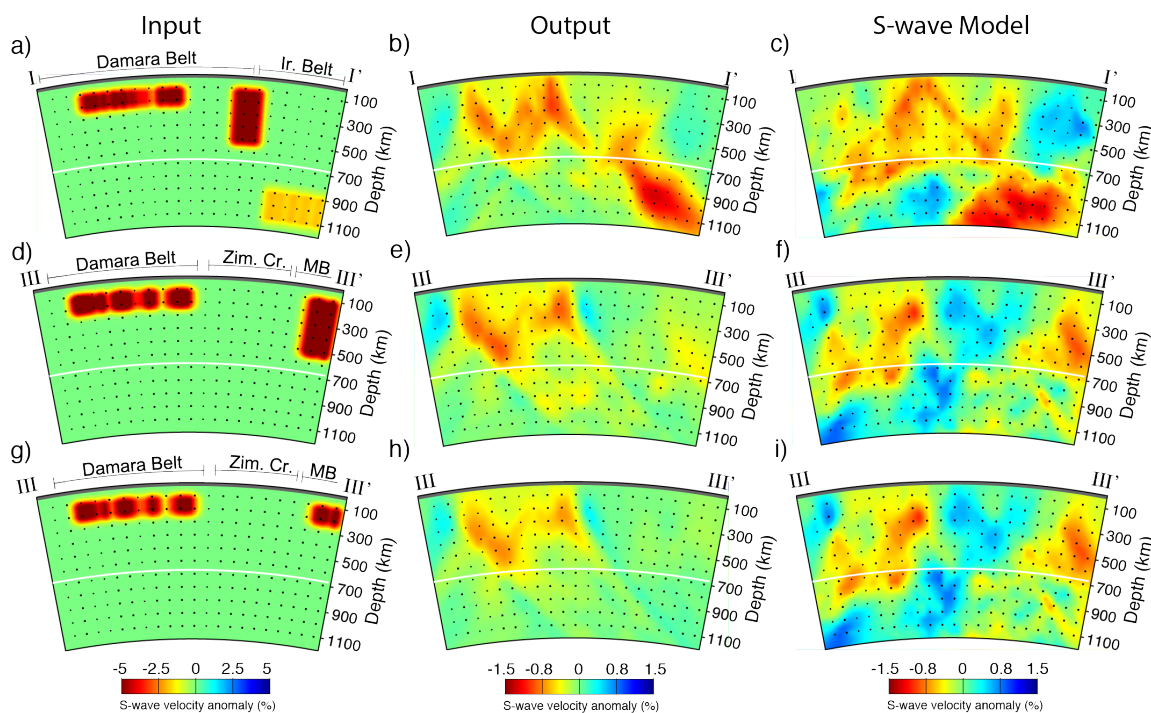


Figure 3-8: a) Tabular body model used to create a synthetic S-wave travel-time dataset representing relatively thin lithosphere (~130 km) adjacent to relatively thick lithosphere (~200 km) beneath the Damara Belt (left of image). A deeper synthetic anomaly is required beneath central Zambia (center of image) and a lower mantle anomaly is required beneath northern Zambia (right of image). The vertical cross-section is taken along transect I (Fig. 3-3). Damara Belt, Zimbabwe Craton (Zim. Cr.) and Mozambique Belt (MB) are labeled. b) Inversion results from synthetic travel-times created using model (a). All anomalies are smeared vertically. c) Vertical cross-section from P-wave model taken along transect I (see Fig. 3-3). d) The same initial tabular model at (a) with a relatively thin lithosphere beneath northern Namibia (left of image) and a deeper low velocity anomaly beneath Mozambique (right of figure). The vertical cross-section is taken along transect III (Fig. 3-3).

In general, the Rehoboth Province is characterized by higher than average seismic velocity (Anomaly H) within our models. In addition to Archean-age detrital zircons collected in the Rehoboth Province (van Schijndel et al., 2011) and high resistivity from MT to a depth of ~180 km (Muller et al., 2009), the faster than average velocity structure in our models suggests that some portion of the Rehoboth lithosphere is cratonic and predates the amalgamation of the Rehoboth Province during the Paleoproterozoic. One possibility is that the faster than average structure is part of the Archean Maltahohe Microcraton (Begg et al., 2009). The velocities

beneath the Rehoboth Province increase from west-to-east, suggesting that some alteration of the cratonic-like lithosphere could have occurred along the western boundary with the Damara Belt during the Pan-African orogeny.

Within central Mozambique, there is a low velocity anomaly (Anomaly I) that extends from the surface to 700 km depth (Fig. 3-3 c). There are several features that point toward the EARS extending southward into the Mozambique Belt in central Mozambique. Fonesca et al. (2014) showed a continuation of active seismicity from the Malawi Rift south along the Urema Graben into central Mozambique. Also using the MOZART data, Domingues et al. (2016) correlated a boundary in crustal velocity with active seismicity that continues into southern Mozambique. In the 500 km depth slice (Fig. B-3), this structure looks very similar to the deep-seated structure beneath southern Zambia (Anomaly D), however we note that it is present in an area of the model with less resolution (Fig. 3-5). We employed synthetic tabular bodies to assess the possible sources of the anomalous velocities on our models (Figs. 3-7 d-i, 3-8 d-i). Results of these tests indicate that thin lithosphere alone cannot account for the structure imaged between 400-700 km depths, and that additional structure extending >200 km is required to fit the P-wave data (Fig. 3-7 d-f). Recovery of the 6% synthetic anomaly in the S-wave model (Fig. 3-8 d-i) indicates that the anomaly may have a larger magnitude in Vs. We suggest that the upper mantle in this region is thermally perturbed to depths ≥ 200 km, and that the perturbation could be geodynamically linked to the African Superplume structure in the lower mantle.

No mapped portions of the Congo Craton or Angolan Shield lie within the footprint of seismic stations used in this study. However, a region of higher than average velocity is present near the northwestern boundary of the Okavango Rift Zone. High conductivity (Bufford et al., 2012), high seismic velocity (Yu et al., 2017), and crustal thickening (Fadel et al., 2018) all point toward the southwestern boundary of the Congo Craton extending into northwestern Botswana along of the northwestern boundary of the Okavango Rift Zone. Our models support this

conclusions, namely that the southeastern boundary of the Congo Craton may extend to the south along the northwestern edge of the Okavango Rift Zone.

Beneath a large portion of the Southern Irumide Belt, velocities in the upper 400 km are higher than average (Anomaly J) and comparable in amplitude to the velocities imaged beneath the southern Kaapvaal Craton (Anomaly A). Several arguments have recently been made for the presence of cratonic-like lithosphere beneath the Southern Irumide Belt, based on a suite of geophysical evidence. Adams et al. (2018) imaged fast structure beneath the Irumide and Southern Irumide Belts, but were unable to distinguish structure between the two belts. Using ambient noise tomography, Emry et al. (2019) imaged fast velocity structure in the upper ~230 km beneath the Southern Irumide Belt and argued for the presence of cratonic fragments (i.e., the Niassa and Lurio Cratons). Modeling lithospheric thickness using magnetotelluric and aeromagnetic data, Sarafian et al. (2018) show thin (~120 km) lithosphere separating thicker (~150 km) lithosphere beneath the Irumide Belt and even thicker (>200 km) lithosphere beneath the Southern Irumide Belt. We therefore attribute the higher than average velocities (Anomaly J) beneath the Southern Irumide Belt to a cratonic fragment, possibly the Niassa Craton.

Summary and Conclusions

In summary, the P-wave and S-wave velocity structure in our models is consistent with other models in regions imaged previously using body wave tomography. For example, the upper mantle velocity structure in our models beneath the Kaapvaal Craton, Limpopo Belt, Zimbabwe Craton, and portions of the Okwa and Magondi Belts (i.e., the greater Kalahari Craton) is higher than average (Anomaly A) and comparable to models from previous studies (e.g., Ortiz et al., 2019; Fouch et al., 2004; James et al., 2001). A low velocity anomaly is present beneath the

Bushveld Complex, extending to the northwest into central Botswana as reported by Ortiz et al. (2019) (Anomaly B). The velocity structure beneath the Namaqua-Natal Belt is nearly average and the upper 400 km beneath the Cape Fold Belt is lower than average, similar to the Ortiz et al. (2019) and Fouch et al. (2004) models. Consistent with previous investigations (i.e., Ortiz et al., 2019; Mulibo and Nyblade, 2013a, 2013b), there is a deep-seated LVZ (Anomaly D) beneath southcentral Zambia that extends at least as deep as the mantle transition zone. Beneath the Okavango Rift Zone, a LVZ is present in the upper 400 km of the mantle (Anomaly C) and is a distinct anomaly from the LVZ beneath the Bushveld Complex and central Botswana (Anomaly B).

There are several new anomalies in our models in regions that have not been imaged previously by body wave tomography. Extending to the southwest from the Okavango Rift Zone in the Damara Belt in northern Namibia, there is a LVZ (Anomaly F) in the upper 400 km of the mantle. Together, anomalies F and C can be explained by thinner lithosphere (~130 km) beneath the Damara Belt compared to thick, cratonic lithosphere (~200 km) to the south, and does not require a thermal perturbation in the upper mantle either from Cenozoic rifting under the Okavango Rift Zone or from the African Superplume. To the west of the Damara Belt, in northwestern Namibia, there is a high velocity anomaly (Anomaly G) beneath the Etendeka Flood Basalt Province. This can be explained by the lithosphere in this region having been altered by Cretaceous volcanism, or from a southern lobe of thick Congo Craton lithosphere. The upper mantle velocity structure beneath the Rehoboth Province is higher than average (Anomaly H) and may reflect the presence of a cratonic fragment, the Maltahohe Microcraton, within the province. A deep-seated LVZ (Anomaly I) is present beneath the Mozambique Belt in central Mozambique, similar in depth extent to the LVZ beneath southcentral Zambia. Thinner lithosphere compared to the adjacent cratons in this region cannot fully explain this anomaly, indicating that the upper mantle may be thermochemically perturbed and linked to the African Superplume. A high

velocity anomaly (Anomaly J) is located to the north of Anomaly I within the Southern Irumide Belt. In addition to Anomaly J in our models, other lines of geophysical evidence indicate the presence of cratonic lithosphere (the Niassa Craton) in this region (Emry et al., 2019; Safarian et al., 2018; Adams et al., 2018).

A major question that can be addressed with our results is whether the upper mantle beneath southern Africa shows signs of a thermochemical perturbation linked to the lower mantle African Superplume structure. While there is a large LVZ throughout the upper mantle beneath the Damara Belt, resolution tests show that thinner lithosphere beneath the Damara Belt (~130 km), compared to thicker cratonic lithosphere (~200 km) to the south, can fully explain the anomalous velocities in our models beneath the Damara Belt, and there is no need to invoke a thermal anomaly in the upper mantle or a geodynamic connection to the African Superplume. Beneath central Mozambique, however, Anomaly I in our models cannot be fully explained by differences in lithospheric thickness alone, indicating that the upper mantle may be thermochemically perturbed, and that the perturbation may be associated with the African Superplume.

With these conclusions, we argue that the source of buoyancy support for the excess elevations of the southern African Plateau likely resides in the mid-to-lower mantle. In contrast, while much of central and southern Mozambique lacks excess rates of uplift and dynamic topography, compared to the rest of southern Africa, the African Superplume anomaly may be providing additional heat to the upper mantle beneath the Mozambique Belt in central Mozambique.

Chapter 4

Surface wave tomography of southern Africa: craton vs off-craton upper mantle structure

Abstract

In Chapter 3, I presented body wave tomography models (P-wave and S-wave) for southern Africa and parts of eastern Africa. From these models, I concluded that, outside of central Mozambique, velocity anomalies in southern Africa primarily arise from differences in lithospheric thickness and that there is little indication of a thermochemical perturbation of the sublithospheric upper mantle. In this chapter, I test that interpretation by creating an independent velocity model, using surface wave tomography, with improved depth resolution compared to the models from Chapter 3. Using a similar group of seismic stations as in Chapter 3, Rayleigh wave phase velocity maps for 30-200 s period were derived using eikonal and Helmholtz tomography. Phase velocity dispersion curves extracted from the maps for 0.5°-by-0.5° cells were inverted for upper mantle shear wave velocity using a Monte Carlo and iterative linearized inversion approach. Crustal properties (i.e., Moho depth and average velocity) were constrained by previous seismic and gravity studies of the crust.

The resulting shear wave velocity model reveals faster and thicker lithospheric mantle beneath Archean terranes than beneath Proterozoic mobile belts. Regional average 1D velocity profiles show a +2-4% velocity difference between the lithospheric root beneath the Kalahari Craton and the adjacent sublithospheric mantle beneath the Damara Belt in northern Botswana and Namibia. At sublithospheric depths, the upper mantle varies little ($\sigma=0.05$ km/s or ~ 80 K) in southern Africa, but is faster than in southern Zambia, eastern Africa, and central Mozambique. The sublithospheric mantle beneath parts of eastern Africa and central Mozambique are ~ 2 -3% slower than southern Africa, outside of central Mozambique, representing a ~ 150 -230 K difference in upper mantle temperatures.

This independent model corroborates the results from Chapter 3, supporting my interpretation that upper mantle velocity anomalies beneath southern Africa arise primarily from differences in lithospheric structure. Compared to eastern Africa, central Mozambique, and AK135, overall sublithospheric mantle velocity structure in southern Africa is faster, providing no indication of a thermochemical perturbation in the upper mantle and therefore no connection to the African Superplume structure.

Introduction

In Chapter 3, I interpreted anomalous structure in my P-wave and S-wave velocity models as signatures of differences in lithospheric thickness between thick, cratonic lithosphere and thinner, mobile belt lithosphere, except for beneath central Mozambique. The models provide little evidence for thermochemical perturbations in the sublithospheric mantle beneath the mobile belts in Botswana and Namibia. In this chapter, I test that interpretation by creating a surface wave tomography model of the same region. Surface wave tomography, with higher depth resolution than body wave tomography, allows me to better constrain the depth extent of the velocity anomalies imaged in the upper mantle in Chapter 3.

To create the surface wave model, I inverted Rayleigh wave phase delays from from 499 $M \geq 6$ earthquakes (Fig. 4-2) using the eikonal and Helmholtz equations to produce phase velocity maps. The earthquakes were recorded on stations from a similar combination of seismic networks as used in Chapter 3 (Fig. 4-1). Dispersion curves were then modeled using a Monte Carlo and iterative linearized inversion approach (Jin et al., 2015; Herrmann, 2013) to obtain 1D velocity models at every half degree across the study area for depths from the Moho to 400 km.

Using my results, I discuss the upper mantle velocity structure within four regions spatially defined in Chapter 3, the Damara Belt in northern Botswana and Namibia, the Kalahari

Craton in southern Africa, the Southern Irumide Belt in eastern Africa, and the East African Rift System in eastern Africa. These four regions allow me to compare velocity differences within depth ranges assessed with synthetic testing in Chapter 3, and to provide independent evidence for or against the conclusions from Chapter 3, that thermochemical perturbations of the upper mantle, possibly connected to the lower mantle African Superplume structure, are limited to eastern Africa and possibly central Mozambique.

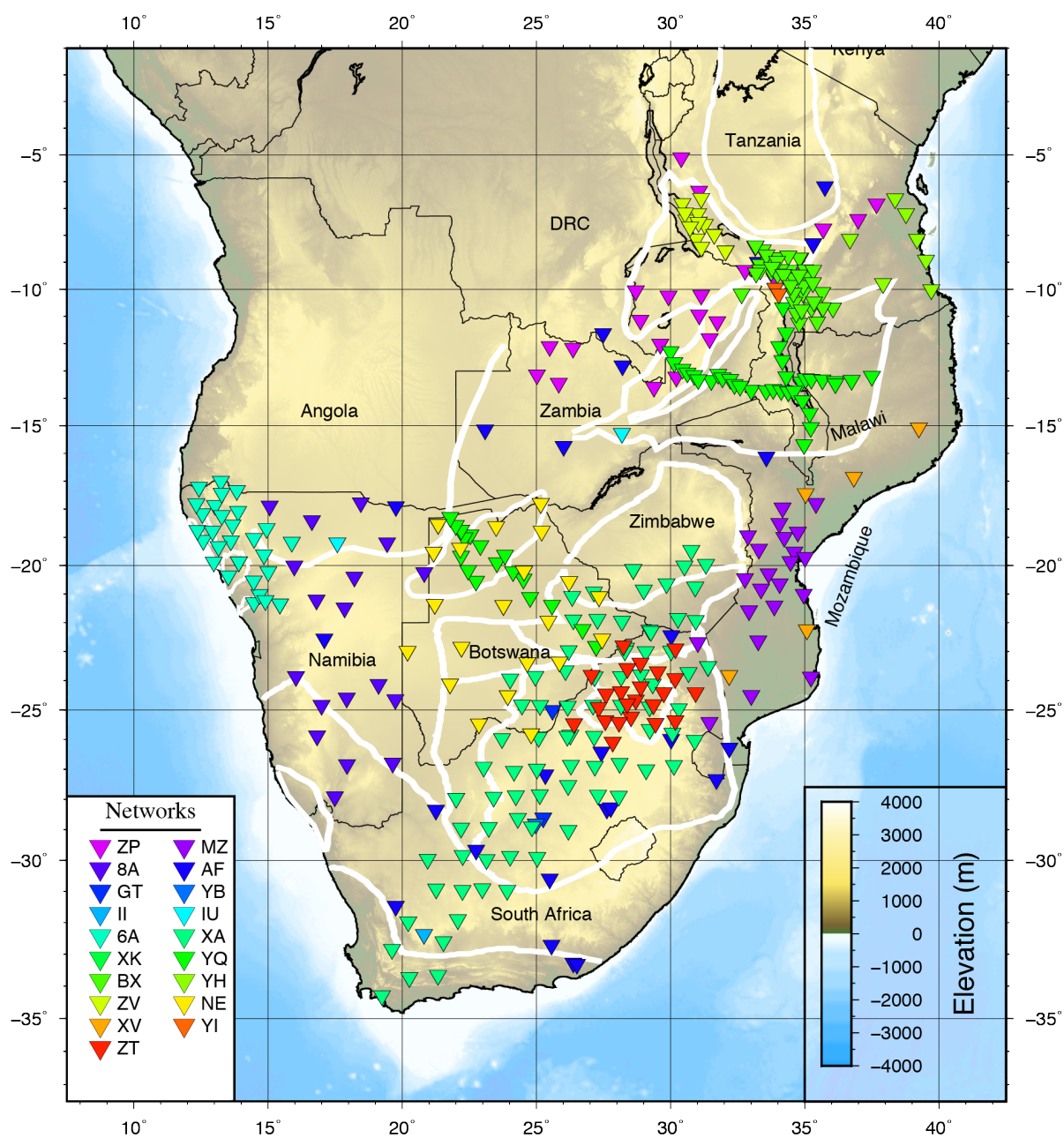


Figure 4-1: Topographic map showing location of seismic stations used in this study. Corresponding seismic network abbreviations are labeled. Tectonic boundaries (white lines) are from labeled in Figure 3-1.

Tectonic Background

The geologic and tectonic context for the study area is reviewed in Chapter 3, where the lithospheric structure and evolution of southern and eastern Africa is described. In summary, southern Africa consists of a patchwork of Archean cratons stitched together by Proterozoic mobile belts and blanketed by Phanerozoic sediments (Fig. 4-1). There are three relevant igneous provinces in southern Africa, the c. 130 Ma Etendeka Flood Basalt Province within the Damara Belt in northwestern Namibia, the c. 180 Ma Karoo large igneous province covering much of the southern African subcontinent, and the c. 2.1 Ga Bushveld Complex within the Kaapvaal Craton in South Africa (Fig. 4-1). Continental rifting is active in the East Africa Rift System and incipient rifting is underway in the Okavango Rift Zone in northwestern Botswana and within the Mozambique Belt in central Mozambique (Fig. 4-1).

Several mechanisms have been proposed as the source of buoyant support for the ~1 km high Southern African Plateau (Fig. 4-1), including density anomalies and flow associated with the African Superplume in the mid-to-lower mantle (Forte et al., 2010; Gurnis et al., 2000; Lithgow-Bertollini and Silver, 1998) and thermally perturbed upper mantle beneath the Kalahari Craton (Li and Burke, 2004).

Previous Geophysical Studies

A comprehensive discussion of previous geophysical studies was provided in Section 3.3. A summary of the most relevant investigations is given below.

Global shear wave velocity models from surface wave tomography initially characterized the large anomalous structure in the mid-to-lower mantle beneath southern Africa. Using a variety of techniques, previous studies were able to make inferences on the thermal and chemical state

(e.g., McNamara and Zhong, 2005; Simmons et al., 2007) and geometry (Ni et al., 2002; Ritsema et al., 1999) of the superplume. In the upper mantle, global surface wave tomography studies primarily imaged fast velocity structure in southern Africa representative of thick, Archean lithosphere, and slow velocity structure in eastern Africa linked to elevated temperatures and partial melt.

Resolution of upper mantle structure was improved by continental-scale surface wave tomography. Sebai et al. (2006) modeled a large region $\sim 1\text{-}4\%$ faster than a 1D reference model in southern Africa and a $\sim 1\%$ low velocity anomaly beneath eastern Africa. In the model developed by Fishwick (2010), cratonic structure became more distinguishable; $2\text{-}4\%$ fast velocity structure beneath the Kalahari Craton was distinct and separate from similarly fast velocity structure beneath the Congo Craton. These images, in turn, provided an estimate of lithospheric thickness beneath Africa, with cratonic lithosphere extending to $\sim 200\text{-}250$ km depth (Fishwick, 2010). A model of lithospheric thickness reported by Priestley et al. (2008) also showed ~ 250 km thick lithosphere beneath the Kalahari Craton, ~ 100 km thicker than the lithosphere beneath the Damara Belt to the northwest. Capitalizing on the ambient noise wavefield, Emry et al. (2019) developed a shear wave velocity model that revealed smaller regions of high velocity correlated with cratonic fragments in eastern Africa (i.e., the Niassa and Lurio Cratons). In their model, cratonic lithospheric mantle had an average shear wave velocity of $\sim 4.60\text{-}4.70$ km/s and the lithospheric mantle beneath the Proterozoic mobile belts had, on average, shear wave velocities of $4.30\text{-}4.50$ km/s.

There have been several surface wave tomography investigations using data from the SASE network in southern Africa. Across all of these studies, a fast velocity lithospheric lid was imaged beneath the Kaapvaal Craton (e.g., Li and Burke, 2006; Chevrot and Zhao, 2007; Adams and Nyblade, 2012). However, these models show differences in the velocity structure of the sublithospheric mantle beneath the Archean lithosphere. Li and Burke (2006) argued for a 4%

reduction in shear wave velocity in the 160-260 km depth range beneath the region. The model developed by Adams and Nyblade (2012), however, showed little indication of a LVZ beneath the cratonic lithosphere. There is also little evidence for a LVZ under the cratonic lithosphere in the continental-scale models (Emry et al., 2019; Fishwick, 2010; Priestley et al., 2008).

The upper mantle velocity structure beneath eastern Africa has also been imaged by regional-scale surface wave tomography. The model developed by O'Donnell et al. (2013), constrained using the two-plane wave method, revealed a focused region of low velocity (~ 4.35 km/s) beneath northern Lake Malawi, a fast velocity lithospheric lid beneath the Tanzanian Craton, equally fast (~ 4.70 km/s) lithospheric mantle beneath the Southern Irumide Belt and slow lithospheric mantle (~ 4.30 km/s) to the east and west of the Tanzania Craton. Using interstation methods, Adams et al. (2018) showed comparable results for eastern Africa.

Complementing the surface wave investigations are a suite of other geophysical studies aimed at characterizing the crustal structure of southern and eastern Africa. The crustal structure of southern Africa has been extensively examined using a range of seismological observations and models. Consistent across these studies is a range of crustal thicknesses, within cratonic regions and the surrounding mobile belts, of ~ 33 - 45 km (for references see Chapter 3). Average crustal velocities in southern and eastern Africa have a narrow distribution, between 3.60 - 3.70 km/s for unrifted crust (Tugume et al., 2013). Of particular note, crustal thicknesses in the two incipient rift zones (Okavango and central Mozambique) fall in the 33 - 45 km range (Yu et al., 2015; Tugume et al., 2013).

Rayleigh wave phase velocities

We constructed a 3D shear wave velocity model for southern Africa by inverting Rayleigh phase velocity for an area between -10°S to -40°S and 10°E to 40°E . Phase velocity ($30, 40, 50, 60, 70,$

80, 90, 100, 110, 120, 135, 150, 170, and 200 s) measurements were made using the Automated Surface Wave Measuring System (ASWMS; Jin and Gaherty, 2016). Data were gathered from a total of 397 broadband seismic stations from 19 different networks (Fig 4-1; Supp. Table 1). Waveform data were collected for ≤ 50 km deep and $M \geq 6.0$ earthquakes with epicentral distances between 20° to 160° over the years of 1997 to 2018. In total, waveforms were collected from 1,419 earthquakes on all stations deployed within the study area at the time of the event. Of these, 499 events provided waveforms with coherent signal within the frequency band of interest (Fig. 4-2).

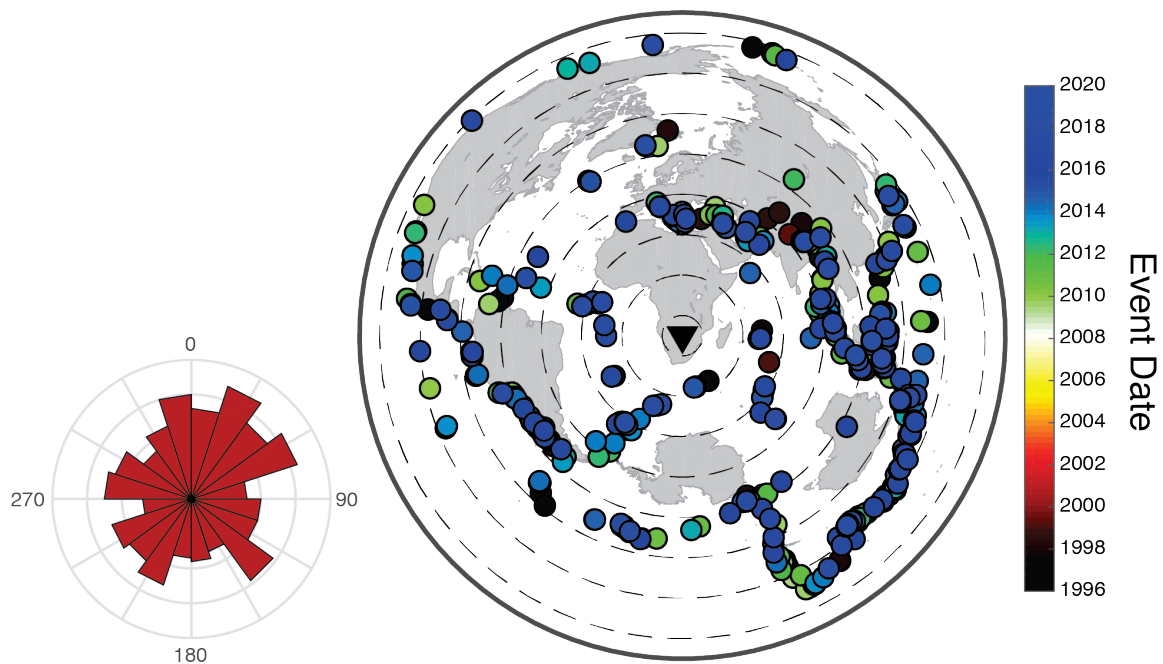


Figure 4-2: Location, event origin time, and back-azimuth for earthquakes used for the final inversion. Additional source information can be found in Table F-2.

After correcting waveforms for instrument response, the ASWMS workflow uses a Generalized Seismological Data Function approach to measure phase delays (Gee and Jordan, 1992), replacing the synthetic waveform with the waveform recorded on a nearby station, windowed between a group velocity arrival window of 5.0-2.0 km/s (Fig. 4-3 a-b). Cross-

correlograms between the waveforms recorded on the two stations are then filtered by a series of narrow-band filters centered around the periods of interest (Fig. 4-3 c-d). Interstation distances were limited to a maximum of 850 km to increase path coverage. For comparison, we also limited the maximum interstation distance to 250 km (Fig. C-5). Correlograms with coherences ≥ 0.5 were fit with a 5-parameter Gaussian wavelet (Jin and Gaherty, 2016) to retrieve phase delays and amplitude estimates at each period. Phase delays greater than 10 s from the predicted phase velocity were rejected to prevent measuring phase delays on skipped cycles. To correct for possible bias imposed by the windowing function, the phase delays were corrected by a time shift measured on a windowed autocorrelation.

Corrected phase delays were then inverted for apparent phase velocity using the eikonal equation and a smoothing of 25% of the wavelength at each period (Fig. C-1). A minimum of three measurements were required for the phase velocity measurements of a cell to be used in further calculations (Fig. C-2). The effects of multipathing, common in the surface wavefield, were corrected for by inverting amplitude measurements using the Helmholtz equation (Jin and Gaherty, 2016). This results in a series of structural phase velocity maps for the study area (Fig. 4-4; Fig. C-3). Phase velocity dispersion curves were then extracted across all periods from each 0.5° -by- 0.5° map cell with at least 3 measurements.

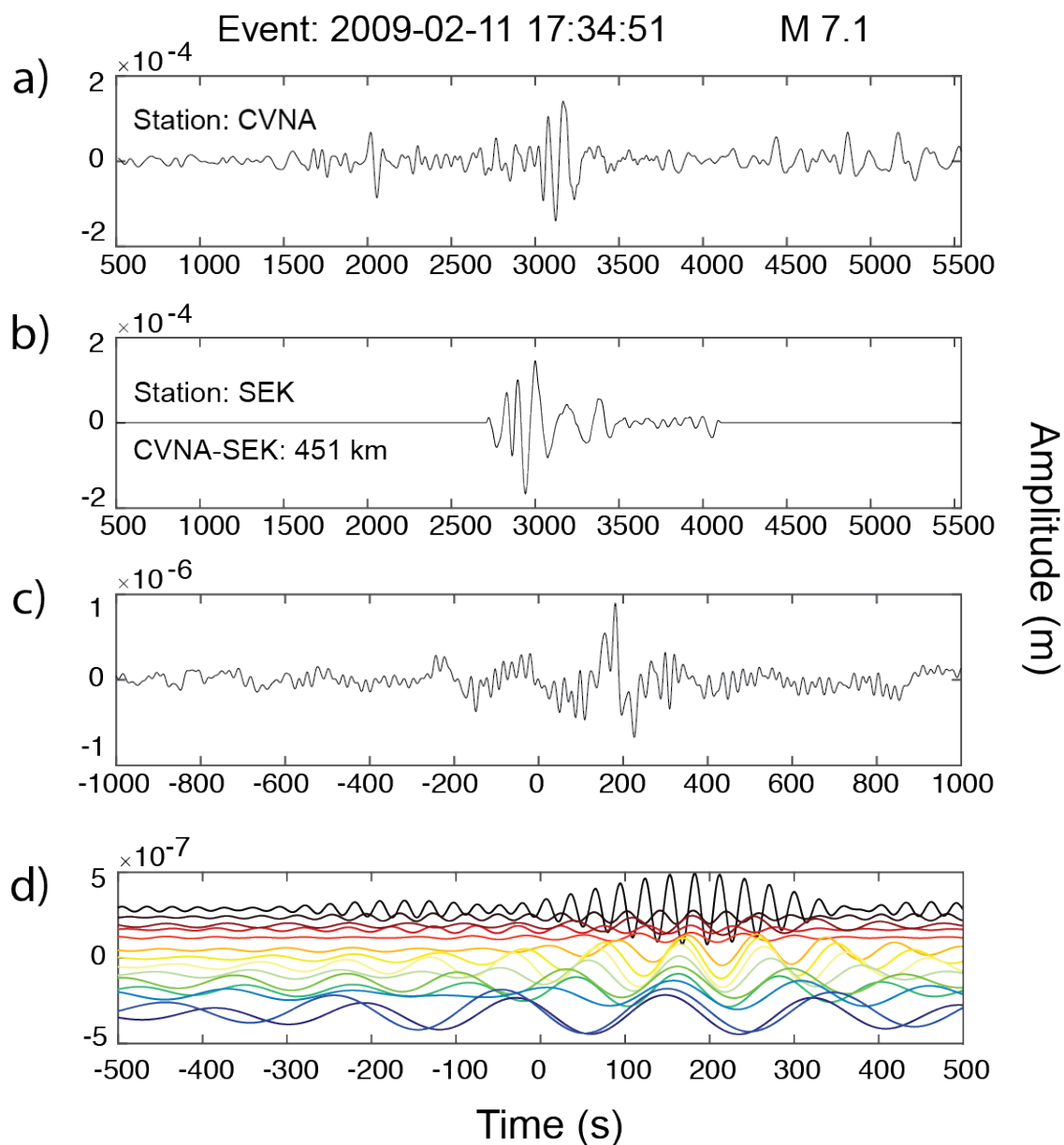


Figure 4-3: a) Teleseismic earthquake recorded on AfricaArray station CVNA filtered between 30-200 s. b) Earthquake waveform recorded on AfricaArray station SEK filtered between 30-200 s and windowed between a 5.0-2.0 km/s group velocity window. c) Cross-correlogram of the waveforms from (a) and (b). d) Cross-correlogram from (c) filtered by a series of narrow band filters with center periods from 30-200 s and offset from the origin for visibility. Warmer colors are for shorter period filters and cooler colors are from longer period filters.

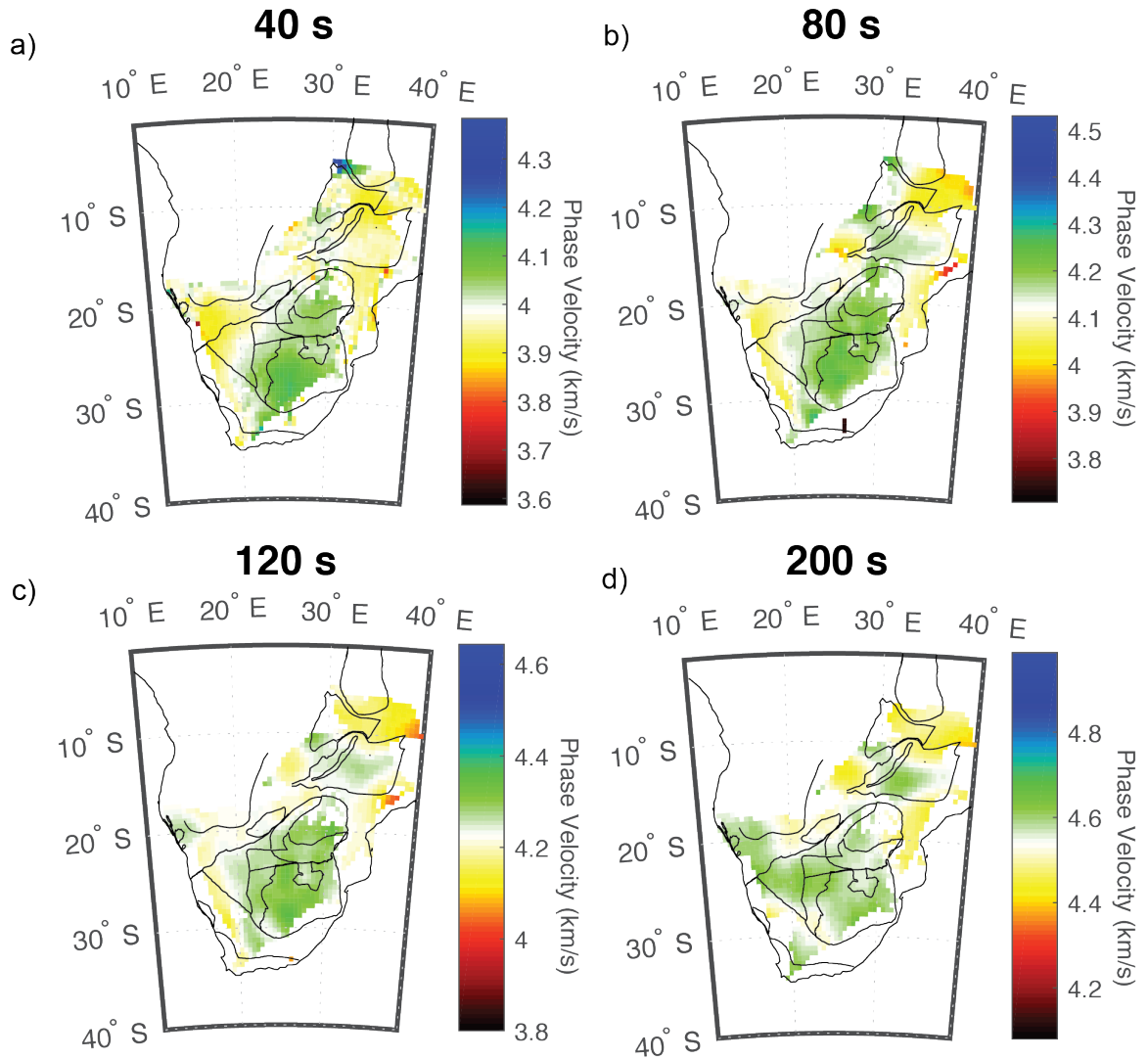


Figure 4-4: Structural phase velocity maps for periods 40 (a), 80 (b), 120 (c), and 200 (d) seconds. Map cells with less than three measurements are not colored.

Inversion for shear wave velocity

Shear wave velocity profiles at each cell in the grid were obtained by inverting the structural phase velocity dispersion curves. The inversion of dispersion curves for velocity can be

sensitive to the initial velocity model, so a 3-layer starting model at each cell was developed using a grid search approach over a limited parameter space (Table 4-1). The top layer (layer 1) was used to represent a sedimentary layer, the middle layer (layer 2) represents the crust, and the bottom layer (layer 3) represents the upper mantle. Crustal thickness at each cell was constrained by a continental-scale crustal thickness model (Tugume et al., 2013). The starting 3-layer model with the smallest misfit between observed and predicted phase velocity (Herrmann, 2013) was kept for each cell. Before applying the Monte Carlo methods to the starting model, the bottom depth was increased to 550 km, where from 400-500 km depth the mantle velocity from the grid search linearly approached the velocity of the AK135 model (Kennett et al., 1995). From 500-550 km depth, the model was set to the AK135 model. To assess the sensitivity of the inversion to the starting model, and reduce its influence on the final result, a Monte Carlo approach was then used to create a suite of 100 initial models for each cell by randomly perturbing the three layers in the starting model independently. Perturbations followed a uniform distribution within 30% of the starting sedimentary layer velocity, 10% of the starting mantle velocity and 5 km of the starting crustal thickness. Average crustal velocity (layer 2) was held at 3.7 km/s due to the narrow distribution of crustal velocities found in southern Africa (Tugume et al., 2013).

Table 4-1: Parameter spaced used in grid search for best fitting starting 3-layer model.

Layer	Parameter
1	[1.0, 2.0] (thickness, km)
1	[2.5] (velocity, km/s)
2	Tugume et al. (2015) (thickness, km)
2	[3.7] (velocity, km/s)
3	[400] (thickness, km)
3	[4.4, 4.5, 4.6] (velocity, km/s)

Each of the 100 initial models was then inverted using an iterative linearized inversion scheme (Herrmann, 2013) to solve for a 1D shear wave velocity model at each cell. Smoothing

was enforced in the inversion except at the velocity jump at the base of the crust and below 500 km depth, where damping forced the model to the input, perturbed AK135 velocities. Of the resulting 100 velocity models, those within 30% of the average misfit of all 100 models were used to calculate the mean and standard deviation of the distribution of the 1D velocity models at each cell (Fig. 4-5).

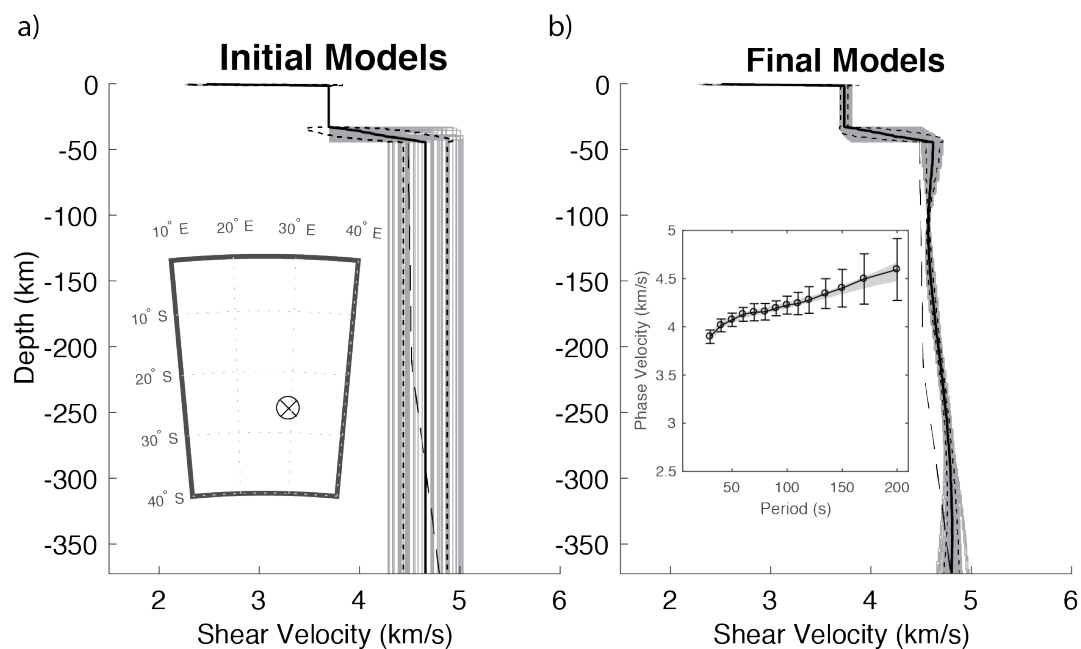


Figure 4-5: a) Starting model from the grid search (black line) and 100 perturbed initial models (gray lines). One standard deviation above and below the mean is marked (dotted lines). AK135 Earth reference model shown with dashed line (Kennett et al., 1995). Cell location marked on inset map. b) Model results from the inversion with mean (black line), one standard deviation above and below the mean (dotted lines), and individual output velocity models (gray lines). Inset: Phase velocities used to constrain the inversion (a-b) along with their uncertainties from Helmholtz tomography. Phase velocities forward calculated for the individual velocity models are shown with gray lines.

Results

Phase velocity maps from the Helmholtz tomography for several periods are shown in Figure 4-4. Stacked apparent and structural phase velocity maps for all periods are shown in Figure C-1 and Figure C-3. Estimates of standard deviation of the resulting phase velocities from Helmholtz tomography (Fig. C-4) are generally <0.02 km/s. Phase velocities range from ~ 3.95 km/s at 40 s to ~ 4.65 km/s at 200 s. Variation in phase velocity is predominantly correlated with tectonic terrane (Fig. 4-4). At 40 s (Fig. 4-4 a), the primary distinguishable structure is the Kalahari Craton, a region ~ 0.20 km/s faster than the surrounding model. At 120 s (Fig. 4-4 c), a region in southeast Tanzania has the slowest phase velocity, while fast structure is present beneath the Kalahari Craton and the Southern Irumide Belt. At 200 s (Fig. 4-4 d), the phase velocity pattern changes, with faster velocities beneath Namibia, in contrast to the relatively slower velocity at shorter periods, and slower phase velocity beneath southern Zambia, central Mozambique, and southeastern Tanzania.

Horizontal cross-sections through the final model are shown in Figure 4-6. Additional horizontal cross-sections can be seen in Figure C-8. The Kaapvaal Craton has the fastest shear wave velocity (~ 4.80 km/s) at 50 km depth. At 120 km depth, the maximum velocity beneath the Kaapvaal Craton is slightly lower (~ 4.70 km/s). In the northern Kaapvaal Craton, beneath the Bushveld Complex, the velocity structure is slightly slower, ~ 4.55 km/s at 50 km depth and 4.60 km/s at 120 km depth. Below 200 km depth, the entire Kaapvaal Craton has a shear wave velocity between 4.70-4.80 km/s.

Shear wave velocity structure beneath the Rehoboth Province is ~ 4.40 -4.50 km/s at 50 km depth, increasing to ~ 4.60 km/s at 120 km depth and 4.75 km/s at 250 km depth. The western portion of the Province is slower than the eastern part of the province, similar to the results from Chapter 3. To the north of the Rehoboth Province, beneath the Damara Belt in Namibia, shear

wave velocity structure is <4.40 km/s at 50 km depth. In northernmost Namibia, the velocities are slightly faster than in central and west-central Namibia. At 120 km depth, the region beneath the Damara Belt in Namibia is almost entirely <4.50 km/s. This region increases in velocity below 120 km to ~ 4.60 km/s at 200 km and ~ 4.70 km/s at 250 km depth. A region of fast structure is present beneath the Etendeka Flood Basalt Province in the Damara Belt in northwestern Namibia. Beneath the Okavango Rift System in northwestern Botswana, velocity structure is ~ 4.55 km/s to a depth of 200 km, below which it begins to increase. Beneath the Damara Belt in southcentral Zambia, the velocity structure is ~ 4.50 km/s at all depths <250 km. Beneath central Zambia and southeastern Democratic Republic of Congo, the shear wave velocity structure is faster than the surrounding Damara Belt. Between 50-200 km depth, the average velocity beneath this area is ~ 4.70 km/s.

The primary pattern in shear wave velocity in eastern Africa is slower in the northeast, beneath northern Lake Malawi and southeastern Tanzania, and faster beneath the Southern Irumide Belt. At 120 km depth, the velocity structure beneath southeastern Tanzania is as low as 4.30 km/s, while at 200 km depth, the region is generally ~ 4.40 km/s. Beneath southern Lake Malawi and the Southern Irumide Belt, the velocity structure is ~ 4.60 km/s at 120 km depth, increasing to 4.75 km/s at 250 km depth.

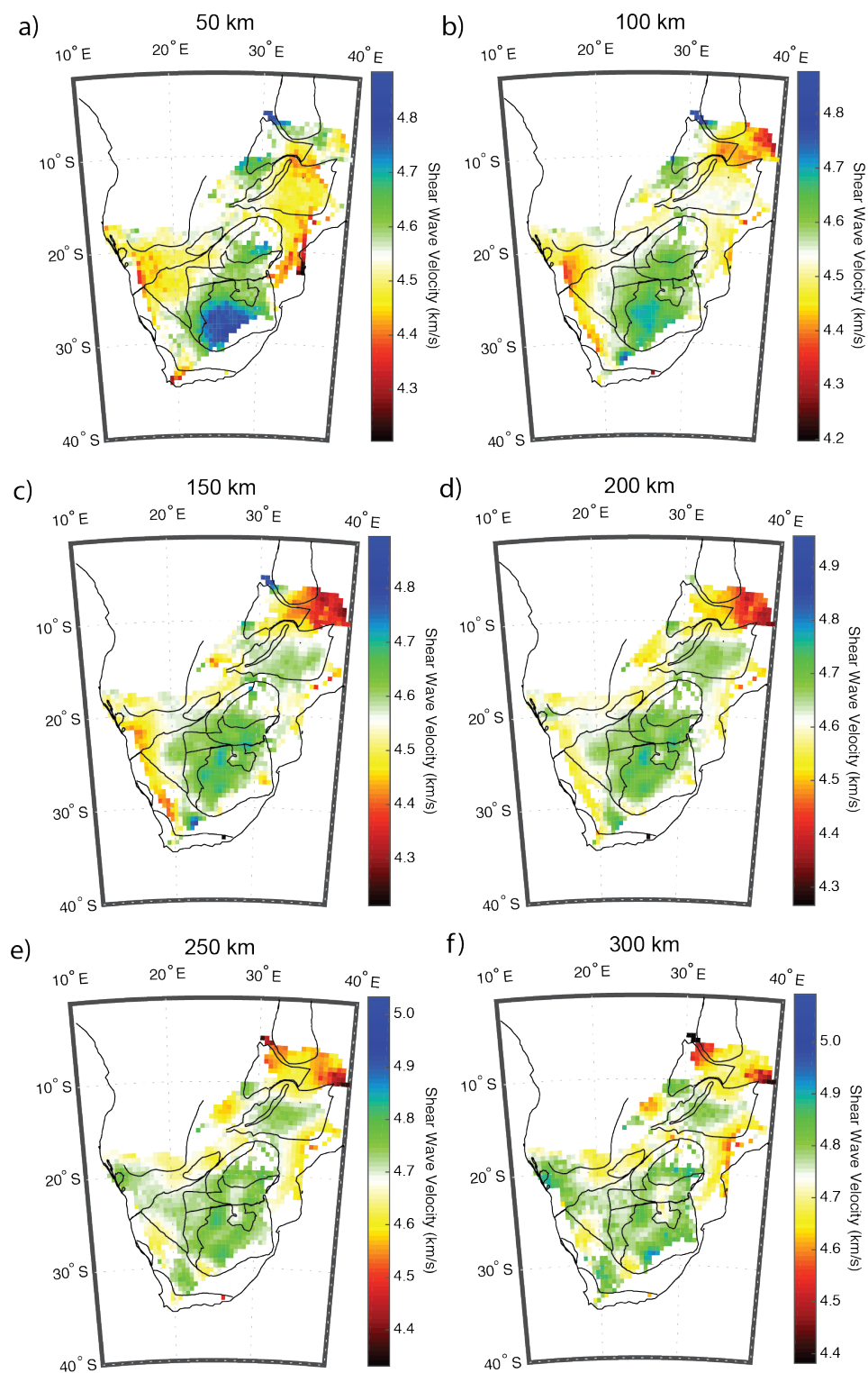


Figure 4-6: Horizontal cross-sections through the final velocity model at 50 km intervals.

Discussion

A large portion of the study area has been imaged previously with surface wave tomography, either at continental- or regional-scale, however given the increase in data coverage used in this study, the resolution in many parts of my model should be improved over previous models. Below, I briefly compare my model with models from previous studies for similarities, and therefore consistency. I then test the conclusions from Chapter 3 against my surface wave model, focusing on four regions, the Damara Belt, the Kalahari Craton, the EARS, and the Southern Irumide Belt. In order to test previous conclusions, and better compare velocity differences with depth, I constructed average 1D velocity profiles for each region (Figure 4-7).

First-order features in my model are very similar to previous continental-scale seismic images of the upper mantle in southern Africa (e.g., Emry et al., 2019; Fishwick, 2010; Priestely et al., 2008; Sebai et al., 2006). In comparison to the most recent model (Emry et al., 2019) at 100 km depth, velocities in my model are within 0.10 km/s of that model, with slightly faster (~ 0.10 km/s) velocity beneath the Kalahari Craton and slightly slower (~ 0.10 km/s) beneath southern Tanzania. At 235 km depth, my model is within 0.05 km/s of the model from Emry et al. (2019) beneath the Kalahari Craton, the Southern Irumide Belt, southeastern Tanzania, and beneath the Etendeka Flood Basalt Province in northwestern Namibia. At 225 km depth, the two models deviate >0.15 km/s in two regions with low velocity, southern Zambia and central Mozambique. However, both of these regions are in areas of my model with higher than average variance (Figure C-4). The shear wave velocity of the uppermost mantle (50-100 km depth) beneath the Kaapvaal Craton is the distinguishingly fast feature in my model. From just below the Moho to ~ 150 km depth, there is a fast lithospheric lid beneath the Kaapvaal Craton with a shear wave velocity of 4.70-4.75 km/s (Fig. 4-6 a), ~ 4 -5% faster than AK135. A fast lid has been estimated previously through modeling regional seismic waveforms. Brandt et al. (2012) modeled the upper

lithosphere to have a shear wave velocity of ~ 4.8 km/s at 50 km depth that decreased to ~ 4.7 km/s at 150 km depth. Similarly fast velocities have been recorded in other cratonic regions. Chen et al. (2007) modeled the upper lithospheric mantle beneath the Slave Craton to have shear wave velocities ~ 4.71 km/s from 50-100 km depth, $\sim 5\%$ faster than AK135 at these depths. Other estimates of upper lithospheric mantle shear wave velocity have a similar range, e.g., 4.77 km/s from 60-150 km depth also for the Canadian Shield (Grand and Helmberger, 1984) and 4.72-4.77 km/s for eastern Europe (Matzel and Grand, 2004). Variability in the shear wave velocities of the lithosphere within the Kalahari Craton has been previously correlated with chemistry of the cratonic lithosphere, where areas with high Forsterite concentrations ($>92\%$) correlate with regions of high upper mantle velocity (Griffin et al., 2003). At >200 km depth, my model is faster than earlier models (Adams et al., 2011; Li and Burke, 2006) and shows no indication of a LVZ beneath the lithosphere.

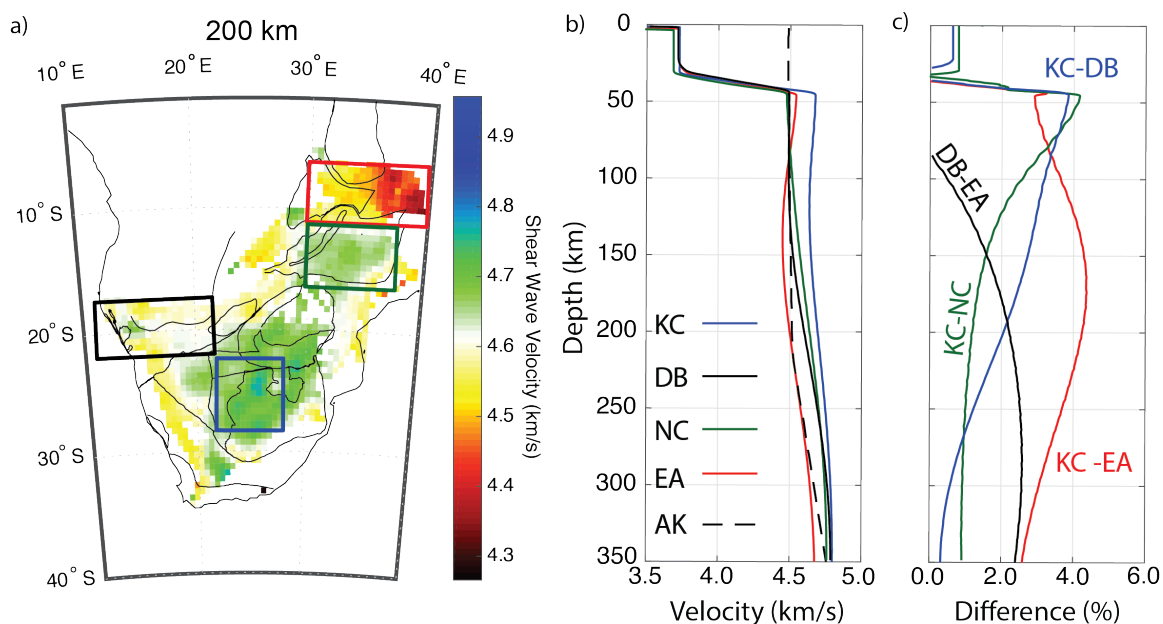


Figure 4-7: a) Areas used to calculate regional average 1D velocity models. KC – Kalahari Craton; DB – Damara Belt; EA – East Africa; NC – Niassa Craton. b) Average 1D velocity profiles calculated for the regions boxed in (a). AK – AK135 (Kennett et al., 1995). c) Percent shear wave velocity difference between 1D velocity profiles in (b).

In eastern Africa, my model is consistent with the model from Adams et al. (2018), created using a similar methodology (i.e., ASWMS; Jin and Gaherty, 2016). For example, Adams et al. (2018) report 80 s phase velocity beneath the Southern Irumide Belt of 4.20 km/s and beneath southern Tanzania of ~ 4.00 km/s, consistent with my phase velocity model (Fig. 4-4). In Chapter 3, the body wave tomography models show 1% higher than average V_p and 1.5% higher than average V_s in the upper mantle beneath the Southern Irumide Belt (Fig. 3-2).

Consistent with previous model interpretations (e.g., Emry et al., 2019; Sarafian et al., 2018; O'Donnell et al., 2013), I attribute the fast velocities beneath the Southern Irumide Belt to structure associated with the cratonic fragment of the pre-Mesoproterozoic Niassa Craton. Interestingly, when I compare the shear wave velocity structure of the Southern Irumide Belt and the Kalahari Craton (Fig. 4-7), the primary difference in velocity resides at <100 km depth. The upper mantle velocity structure of the Rehoboth Province follows a similar pattern, with distinguishable differences ($>2\%$) from the Kalahari Craton only in the upper 100 km of the mantle. Anisotropy in the lithospheric mantle could manifest in velocity differences at these depths, however, the majority of mantle anisotropic indicators in southern and eastern Africa (e.g., shear wave splitting) are largely uniform and have been interpreted as evidence of anisotropy primarily associated with the sublithospheric mantle (Yu et al., 2015; Bagley and Nyblade, 2013; Silver et al., 2001). As previously noted, the Kaapvaal Craton is particularly fast in my model between 50-100 km depths, compared to other cratonic regions in southern and eastern Africa. This could be evidence of the chemical layer of the Kaapvaal Craton lithosphere (Yuan and Romanowicz, 2010) having distinguishable composition compared the cratonic lithosphere in other areas (i.e., the Rehoboth Province and Niassa Craton).

Another region that shows a similar pattern of upper mantle velocity structure as the Southern Irumide Belt and the Rehoboth Province, in both the body and surface wave models, is the upper mantle beneath the Etendeka Flood Basalt Province. In the top ~ 150 km of the surface

wave model, the Etendeka region has comparable velocities to the broader Damara Belt (Fig. 4-6), however the velocity structure diverges between ~150-250 km depth. Yuan et al. (2017), from modeling receiver functions in northwestern Namibia, argued for layering in the lithosphere. They suggested that the layering represents lithosphere that was thermally eroded during the interaction with the Tristan Da Cunha mantle plume c. 130 Ma, then subsequently thickened with depleted peridotite mantle. My model supports their interpretation in that, at lithospheric lid depths (i.e., <150 km), the lithospheric mantle beneath the Etendeka region is similar to the lithospheric mantle beneath the broader mobile belt, but the lower lithosphere (>150 km) is representative of a thickened lithosphere or a body of depleted, or chemically differentiated from melt extraction, mantle that has not been entrained in mantle convection, possibly because of the slow moving African plate.

In northwestern Botswana, a LVZ has been imaged in the upper 400 km by several previous body wave tomographic studies (Ortiz et al., 2019; Yu et al., 2017) including Chapter 3 in this thesis. While some previous authors have argued that the LVZ arises from excess temperatures in the asthenospheric mantle (Yu et al., 2017), our synthetic tests from Chapter 3 show that the imaged anomaly could be a result of differences in lithospheric thickness, and that the deeper depths at which the LVZ is imaged are caused by vertical smearing common in body wave tomography. We, therefore, treat the LVZ beneath the Okavango Rift Zone as part of the broader structure present throughout much of the Damara Belt in northern Namibia and Botswana. In Chapter 3, I determined that the $\pm 1\%$ Vs anomalies imaged in the upper 400 km between the Kalahari Craton and the Damara Belt in northern Botswana and Namibia (Fig. 3-3) could be attributed to a difference in lithospheric thickness between thicker (~200 km) cratonic lithosphere and thinner (~130 km) mobile belt lithosphere. Using synthetic tests constrained by xenolith data (i.e., 250-300 K difference between 130-200 km depth), I estimated that, along with possible compositional differences, there could be a 6% Vs difference between the two regions in

the 130-200 km depth range. Recovery of a dataset created through a 6% anomaly over these depths did indeed create a pattern similar to the real V_s model.

In the regional 1D velocity profiles (Fig. 4-7 c), the difference in shear wave velocity between the Kalahari Craton and the Damara Belt in northern Botswana and Namibia is maximum just below the Moho, at ~4%, and decreases with depth. At 200 km depth, the difference is ~2% and below ~275 km, it is less than 1%. While this is smaller in absolute magnitude than the 6% anomaly used in the synthetic tests in Chapter 3, it is spread over a larger depth range (~50-250 km) and integrates to a larger anomaly. Therefore, this depth distribution of anomalous velocities could result in a similar velocity structure imaged in the body wave models. At sublithospheric depths for both the Kalahari Craton and Damara Belt (i.e. >250 km), the difference in average shear wave velocity is <1%, which, following the same conversions used in Chapter 3, represents a <50 K temperature difference in the sublithospheric mantle between two the regions. Therefore, I argue that that the velocity model obtained from surface wave tomography is consistent with the velocity models from Chapter 3. Unfortunately, the limited resolution in the surface wave model prevents a similar comparison with the upper mantle imaged beneath central Mozambique in Chapter 3.

In Chapter 3, I also concluded that the sublithospheric mantle in most of southern Africa is not thermochemically perturbed, and, therefore, likely disconnected from the lower mantle African Superplume structure. To test this interpretation, I examine histograms from the horizontal cross-section at 300 km depth (Fig. 4-8) and the regional 1D velocity profiles (Fig. 4-7). Beneath southern Africa, in the horizontal cross-section, the distribution of velocities across southern Africa have a standard deviation of 0.05 km/s with a mean of 4.76 km/s. On average, they are faster than AK135 at this depth (Fig. 4-7), which is consistent with previous global models for the region (e.g., Sebai et al., 2006) and their variance is relatively small. In contrast, beneath the EARS, the average velocity at 300 km depth is 4.64 km/s, roughly 2% (0.11 km/s)

slower than the Damara Belt, 3% (0.14 km/s) slower than the Kalahari Craton, and 0.5% (0.03 km/s) slower than the AK135 model. The 2-3% velocity difference between the EARS and the southern African regions at 300 km depth translates to a ~150-230 K temperature difference (Cammarano et al., 2003). This finding corroborates the conclusions from Chapter 3, that outside of central Mozambique, the sublithospheric upper mantle beneath southern Africa is not thermochemically perturbed, at least not to the same extent as the upper mantle beneath eastern Africa.

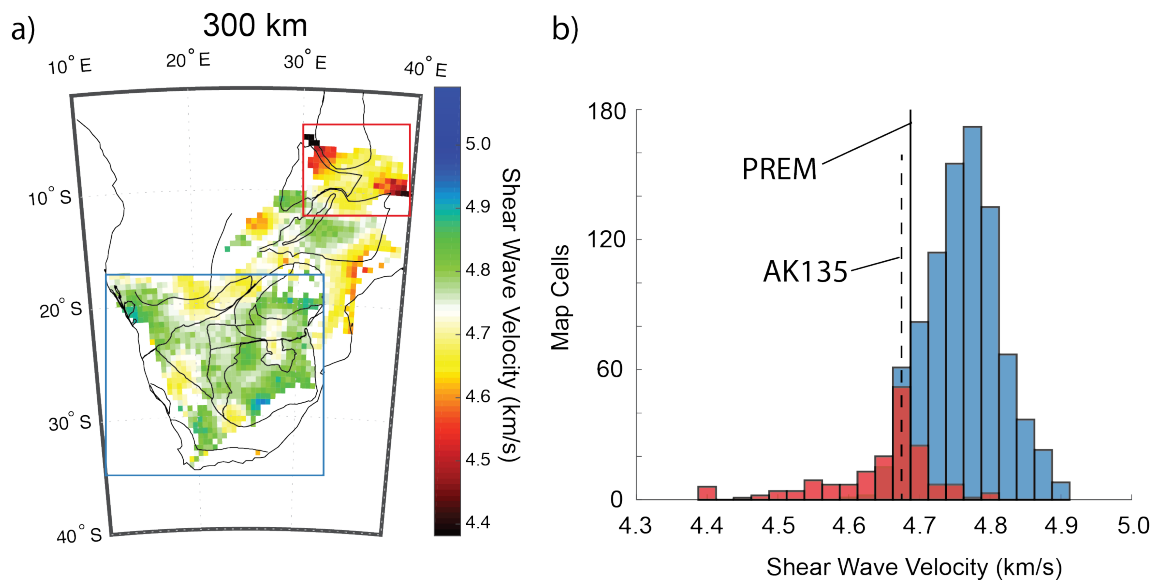


Figure 4-8: a) Horizontal cross-section through the shear wave velocity model at 300 km depth. Boxes encompass a general region for southern Africa (blue) and eastern Africa (red). b) Shear wave velocities of cells within the regional boxes from (a).

Summary and Conclusions

The upper mantle shear wave velocities derived in this model are consistent with previous continental-scale (e.g., Emry et al., 2019; Sebai et al., 2006) and regional-scale (Adams and Nyblade, 2012; Li and Burke, 2006) models of the study area. The velocity structure beneath

the Kalahari Craton is similar to previous models developed using the SASE dataset and does not indicate the presence of a LVZ in the sublithospheric upper mantle.

Regional average 1D velocity profiles (Fig. 4-7) show a difference in velocity between the Kalahari Craton region and the Damara Belt in northern Botswana and Namibia of ~4% just below the Moho, which decreases to less than 1% at 275 km depth. The velocity beneath an area in eastern Africa, however, is >2% slower than the Kalahari Craton at all depths, and ~2% slower than the Damara Belt below ~175 km depth. The velocity variations indicate that sublithospheric mantle temperatures may vary by ~80 K throughout southern Africa, but could be ~150-230 K higher beneath eastern Africa, if the majority of the velocity differences arise from thermal variations.

The newly developed surface wave model for southern and parts of eastern Africa corroborate interpretations from Chapter 3. The velocity difference between the Damara Belt in northern Botswana and Namibia and the Kalahari Craton is similar to the anomaly derived in synthetic tests in Chapter 3. The sublithospheric mantle shear wave velocities for most of southern Africa have a narrow distribution ($\sigma=0.05$ km/s; Fig. 4-8) and are significantly faster than velocities in eastern Africa and the AK135 model, providing little indication of a thermal anomaly in the upper mantle. Together, these results support conclusions from Chapter 3, that the velocity variations in the upper mantle in southern Africa arise primarily from differences in lithospheric structure and that there is no thermochemical connection to the lower mantle African Superplume structure beneath southern Africa, except for beneath central Mozambique.

Chapter 5

Conclusions

In this thesis, I applied regional-scale seismic tomography to data recorded on seismic stations from multiple temporary, semi-permanent, and permanent networks in Antarctica and Africa. Both of these regions have outstanding questions about residual topography, rifting, and volcanism, and the role the upper mantle plays in these processes. The new upper mantle velocity models that I present expand previously published model areas, covering multiple tectonic terranes, and allowing for the interpretation of velocity anomalies within these terranes to be discussed relative to the same reference velocity.

West Antarctica

In Chapter 2, I presented a P-wave relative velocity model that I developed using data collected from the RIS, TAMSEIS, TAMNET, and POLENET linear networks, complemented by data from regional POLENET and permanent stations in Antarctica. My model covers an area from Marie Byrd Land, across the Ross Sea Embayment, into East Antarctica. The model has improved resolution compared to previous models, enabling me to address whether the upper mantle LVZ beneath Marie Byrd Land connects to LVZs imaged in Northern Victoria Land, along the Terror Rift, and beneath Ross Island. Upper mantle LVZs imaged in the model are highly correlated with areas of active volcanism and rifting (Fig. 5-1). In addition, the upper mantle beneath the King Edward VII Peninsula is below average. Seismic activity in this area has previously been identified, suggesting that magmatic processes may be present in the area. The primary insight gained from my model comes from newly imaged structure in the upper mantle beneath the Ross Sea Embayment. Through the correlation of these anomalies with crustal

structure (Fig. 5-1), I interpreted the heterogeneity in upper mantle velocity in this region as evidence of three primary phases of rifting in the West Antarctica Rift System. I further argue that the magnitude and depth extent of the velocity variations in the model can be explained by differences in temperature or thickness of the lithospheric mantle. These differences, over length scales of 100s km, could represent $\sim\pm 10$ mW/m² differences in heat flow and 10^2 Pa s differences in mantle viscosity, and influence the West Antarctica Ice Sheet as it responds to climatic forcings.

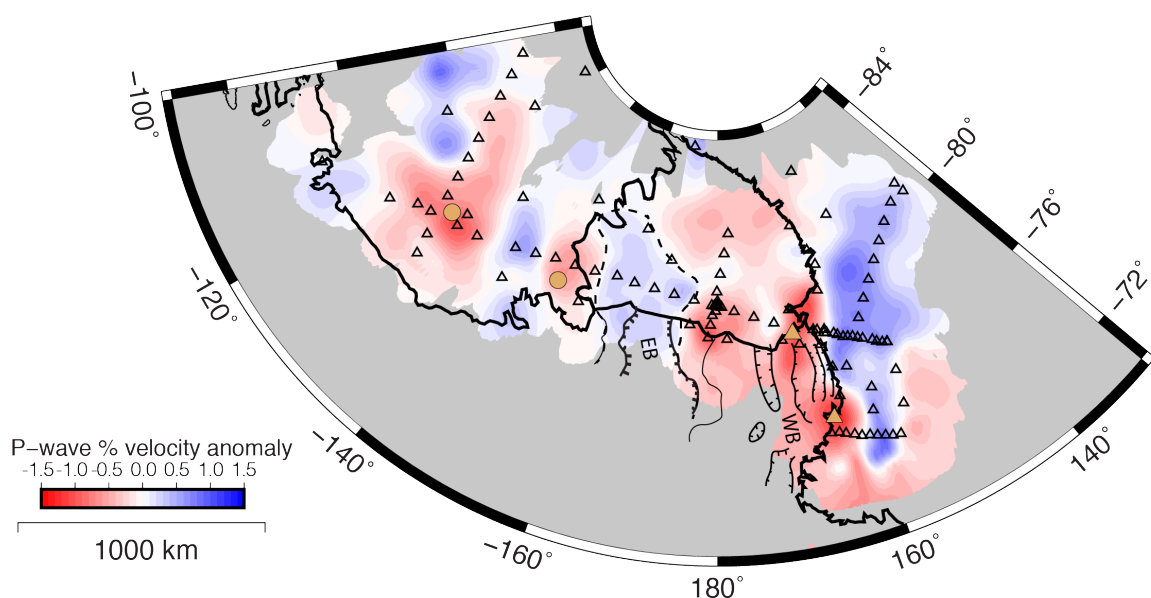


Figure 5-1: Depth slice at 200 km through P-wave model showing the eastern (EB) and western (WB) portions of the RSE, the locations of seismicity in MBL (orange circles), active volcanoes (orange triangles) and seismic stations (open triangles).

Southern Africa

In Chapters 3 and 4, I presented new upper mantle velocity models for a region covering southern and parts of eastern Africa. These models expand previous models into the Proterozoic mobile belts adjacent to the Kalahari Craton. This is important because many of the outstanding

questions of the tectonic development of southern Africa, including what forces support the high elevations of the Southern African Plateau and how the African Superplume affects continental rifting and volcanism, require strong constraints on upper mantle properties. A large obstacle in imaging the sublithospheric upper mantle has been the thick lithosphere beneath the Kalahari Craton. The new data collected on the adjacent mobile belts, used in Chapters 3 and 4, provide important constraints on the sublithospheric upper mantle structure away from the Kalahari Craton.

In Chapter 3, I presented new body wave (P-wave and S-wave) tomographic models for the region. In these models, the high spatial resolution of body wave tomography provides clear boundaries on upper mantle architecture. In one area of interest, there is a distinct horizontal gradient that follows the southern boundary of the Damara Belt. Using synthetic tests, I show that velocity anomalies in this region can be explained by differences in lithospheric thickness between the Damara Belt and the Kalahari Craton including the Rehoboth Province. Beneath the Mozambique Belt in central Mozambique, a deeper-seated structure appears that cannot be fully explained by differences in lithospheric thickness alone, requiring some thermochemical perturbation in the sublithospheric mantle. However, in these models, this area has decreased resolution resulting from reduced station coverage. My interpretation is that the majority of the new anomalies in southern Africa, outside of central Mozambique, can be fully explained by differences in lithospheric thickness and that there is little, if any, indication of a thermochemical anomaly in the upper mantle. Therefore, with the exception of central Mozambique, the upper mantle in southern Africa is likely disconnected from the thermochemical African Superplume structure and the source of buoyant support of the Southern Africa Plateau likely resides in the mid-to-lower mantle.

In Chapter 4, I test my interpretations from Chapter 3 by creating a surface wave tomography model over the same region of southern Africa. Using eikonal and Helmholtz

tomography, I created phase velocity maps from interstation measurements of Rayleigh waves (30-200 s) from teleseismic earthquakes. I inverted phase velocity dispersion curves for shear wave velocity using a Monte Carlo and iterative linearized inversion approach. My model is consistent with previously published results and provides new constraints on the upper mantle velocity structure beneath the mobile belts. Using average velocity profiles for four regions, the Damara Belt, including the Okavango Rift Zone, in northern Botswana and Namibia, the Kalahari Craton in southern Africa, the Southern Irumide Belt in eastern Africa, and the East Africa Rift System in southeastern Tanzania, I compare velocity structure at several relevant depths. These profiles show significant differences in lithospheric velocity between the Kalahari Craton, the Damara Belt, and the EARS. In the sublithospheric mantle, there is a narrow distribution of velocities ($\sigma = 0.05$ km/s) across southern Africa, outside of central Mozambique. However, the upper mantle structure at the same depths beneath the EARS is significantly slower and possibly ~ 150 - 230 °C hotter. By adapting the synthetic tests from Chapter 3 with results from Chapter 4 (Figs. 5-2 and 5-3), I show that velocity variations imaged within the upper mantle using surface wave tomography are consistent with the velocity variations imaged using body wave tomography. This comparison supports my interpretations from Chapter 3, that 1) the majority of the upper mantle velocity anomalies in southern Africa, outside of central Mozambique, can be explained by differences in lithospheric structure, 2) that the upper mantle beneath southern Africa, outside of central Mozambique, shows no indication of a thermochemical anomaly or connection to the lower mantle African Superplume structure, and 3) it is unlikely that buoyant support for the Southern African Plateau is provided by thermally-induced density anomalies in the upper mantle.

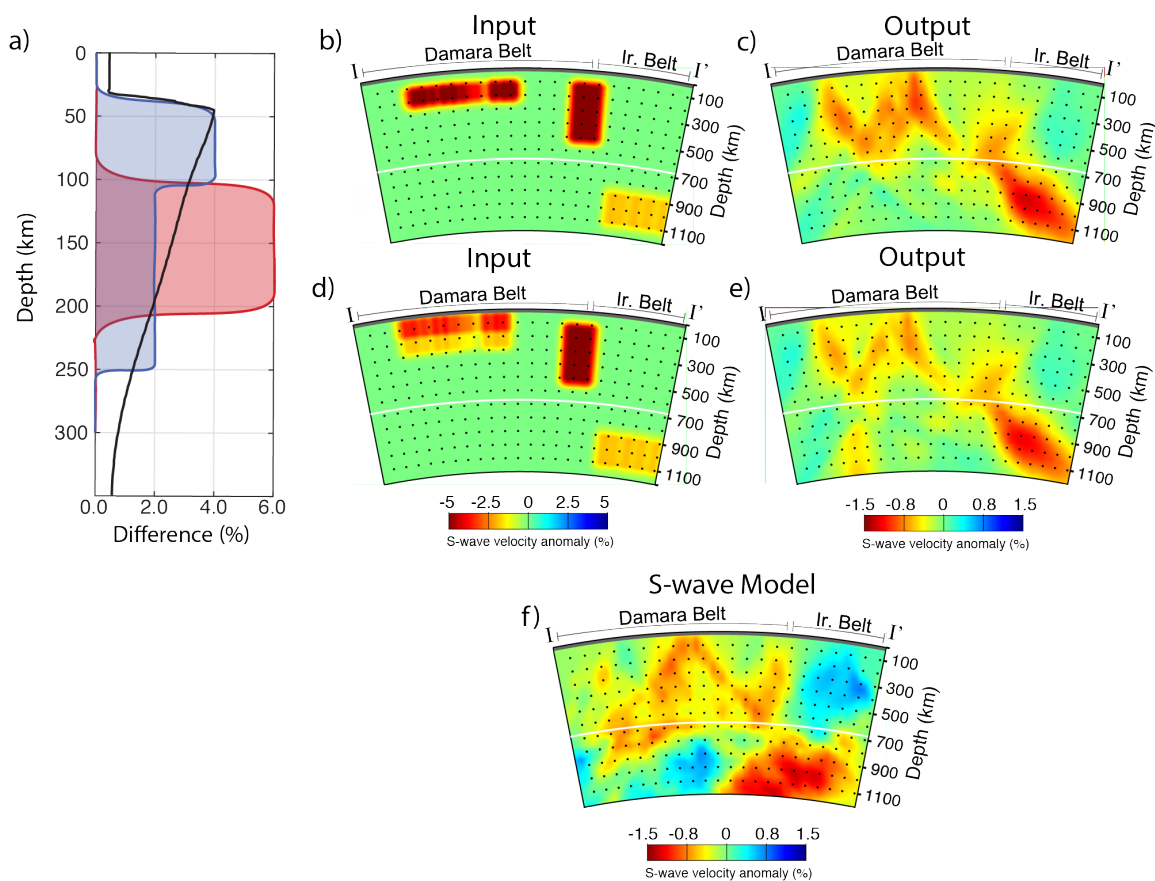


Figure 5-2: a) Shear wave velocity difference between the Kalahari Craton and Damara Belt (black line). 1D velocity profiles through the synthetic velocity structure, or tabular bodies, used in Fig. 3-8 a (red) and the adapted profile (blue), more closely representing the black line. b) Synthetic velocity structure from Fig. 3-8 used to create a synthetic dataset of relative travel-times. c) Results from inverting the dataset calculated through (b) d) Synthetic velocity structure created to represent the velocity difference between the Kalahari Craton and Damara Belt from Chapter 4. e) Results from inverting the synthetic dataset created through (d). f) Vertical cross-section through the S-wave model (same as Fig. 3-4 b).

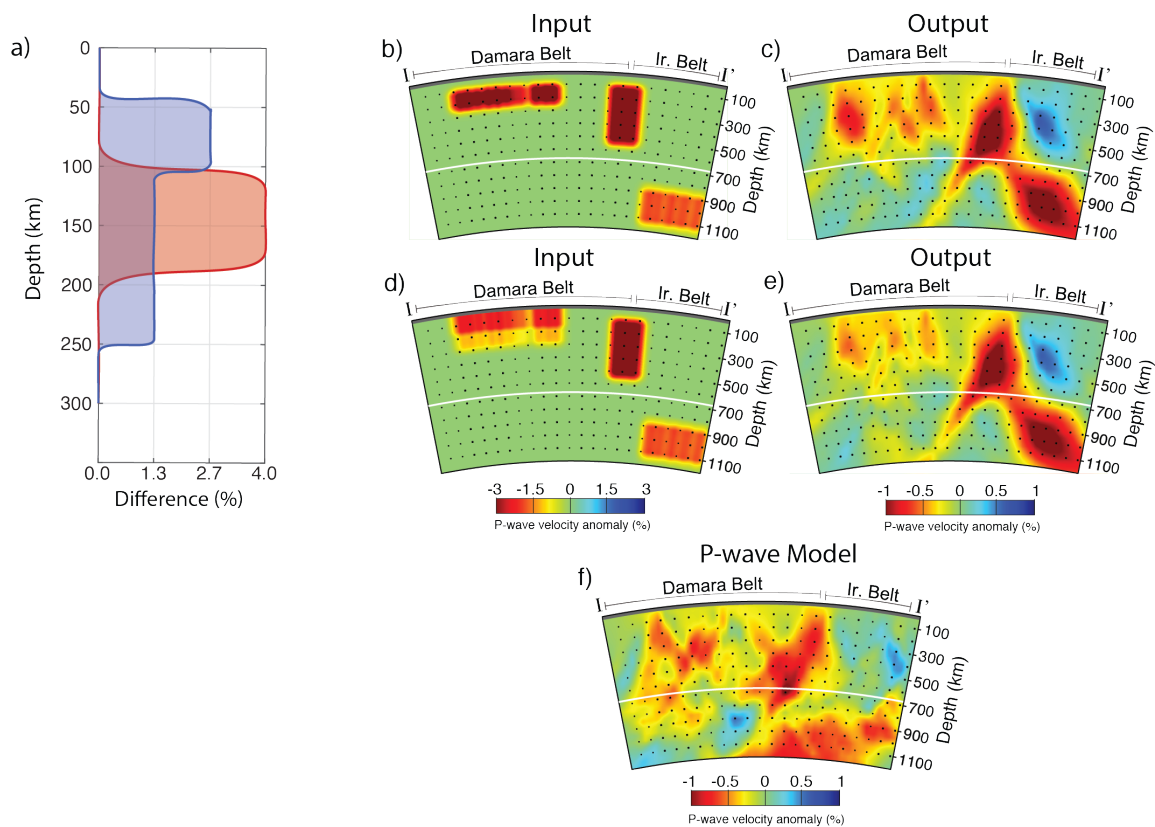


Figure 5-3: a) P-wave velocity difference between the Kalahari Craton and Damara Belt from Chapter 3 (red) and by making similar adjustments to Fig. 5-2 a. b) Synthetic velocity structure from Fig. 3-7 used to create a synthetic dataset of relative arrival times. c) Results from inverting the dataset calculated through (b). d) Synthetic velocity structure created to represent the velocity differences between the Kalahari Craton and Damara Belt from Chapter 4. e) Results from inverting the synthetic dataset created through (d). f) Vertical cross-section through the P-wave model (same as Fig. 3-3 b).

Future Work

Antarctica

The upper mantle P-wave velocity model presented in Chapter 2, along with other recently published models of upper mantle velocity structure, have greatly increased the resolution and footprint of tomographic images of the upper mantle in West and East Antarctica. Gaps still remain, however, in a few key areas and I will discuss several regions in which future work would be valuable.

The model presented in Chapter 2 now provides images of the upper mantle seismic structure referenced to a single velocity mean and with the spatial resolution of 100-200 kms across a large portion of West Antarctica including the Ross Sea Embayment. Inferences from this model have improved our understanding of the upper mantle velocity structure within the West Antarctic Rift System (WARS), from which we have both interpreted the evolution of the rift system and constrained the areas in West Antarctica that have likely thinned in the recent past. However, the model does not cover the entire WARS, so a natural next step would be to expand the model into the central portion of the WARS so that the entire rift system could be imaged within the same model and with comparable spatial resolution. This future work would provide a comprehensive image of the heterogeneity in the upper mantle structure of the entire WARS and showcase any areas that have undergone rifting the last ~60 Ma.

Another area that deserves future investigations is the Wilkes Subglacial Basin in East Antarctica. In the model presented in Chapter 2, the upper mantle beneath the region has velocities that are lower than average, atypical for East Antarctica. Considering that the Wilkes Subglacial Basin has very low topography, well below sea level, better constraining the spatial

extent of the LVZ beneath the Wilkes Subglacial Basin would provide important information on the viscoelastic properties of the upper mantle beneath the basin for future cryospheric studies.

Africa

In Chapters 4 and 5, I presented models of the upper mantle velocity structure for a large region covering most of southern Africa and parts of eastern Africa. Broad conclusions were drawn for the state of the sublithospheric upper mantle for most of southern Africa, but the upper mantle beneath central Mozambique was exempted from these conclusions. That came in large part from a more deep-seated LVZ imaged beneath central Mozambique, an area associated with the southern propagation of the East African Rift System (EARS). I believe that future work on the characterization of the upper mantle in southern Africa should focus on better constraining this LVZ beneath central Mozambique. This would require additional seismic stations to be deployed in Mozambique, as well as central Zimbabwe, to improve data coverage in this region. The Niassa Craton has now been imaged by a variety of geophysical techniques north of central Mozambique and lies in the path of the EARS between northern Lake Malawi and central Mozambique. A key question remains as to how the forces driving both the active and incipient rifting are able to migrate through, around, or under the Niassa Craton and into central Mozambique. In addition to improving resolution in body and surface wave tomography in central and southern Mozambique, as well as Zimbabwe, characterizing the thickness of the transition zone in the region, through receiver function analysis, would also provide valuable information on how the upper mantle LVZ beneath central Mozambique may be connected to the large thermochemical structures in the lower mantle and driving the propagation of the rift system.

In addition, much of this thesis has been focused on comparing the upper mantle structure between the Damara Belt and the Kalahari Craton. However, a large, adjacent region that would be useful for comparison is the upper mantle beneath the Congo Craton in Angola. I have shown evidence that the upper mantle seismic structure is highly correlated with the southern boundary of the Damara Belt, but how the upper mantle changes between the Congo Craton and the Damara Belt is difficult to determine and at the edge of my model. Further deployment of seismic stations into Angola would provide novel data and allow for a similar set of velocity models to encompass both the Kalahari Craton and the Congo Craton together, as well as the structure between.

Lastly, an interesting result of the surface wave model is that the upper 100 km of the mantle varies between the Kalahari Craton and the other regions in southern and eastern Africa. My best interpretation is that this arises from differences in composition within the chemical layer of the cratonic lithosphere. In order for this interpretation to be made more concrete, a surface wave analysis that constrains anisotropy would be useful for characterizing the source of the differences in velocity within the shallow lithospheric mantle, and provide useful insight into the tectonic development of southern Africa.

Appendix A

Supplemental Figures for Chapter 2

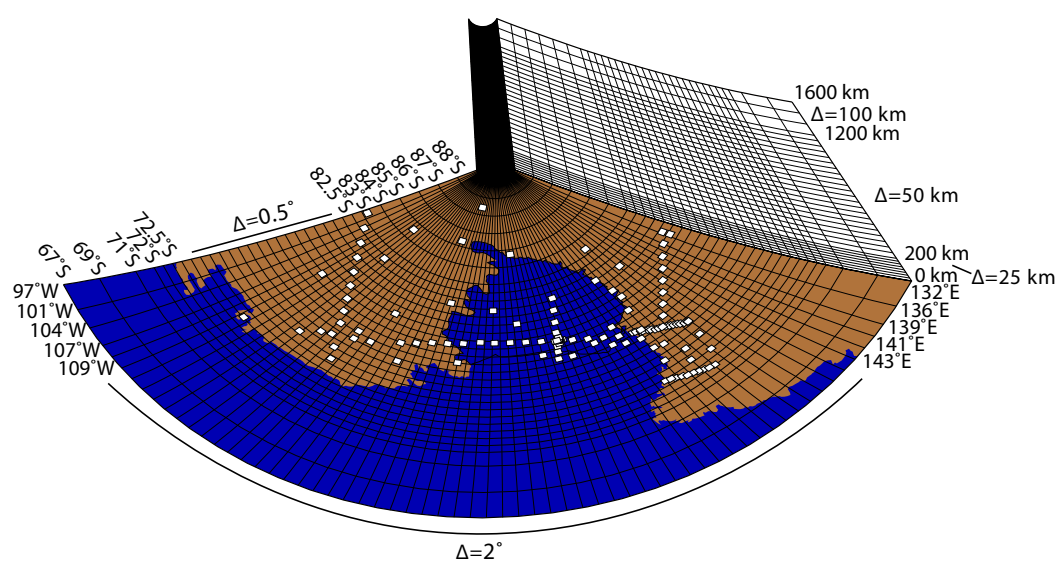


Figure A-1: Model domain showing location of knots in latitude, longitude, and depth. Location of seismic stations marked by white squares.

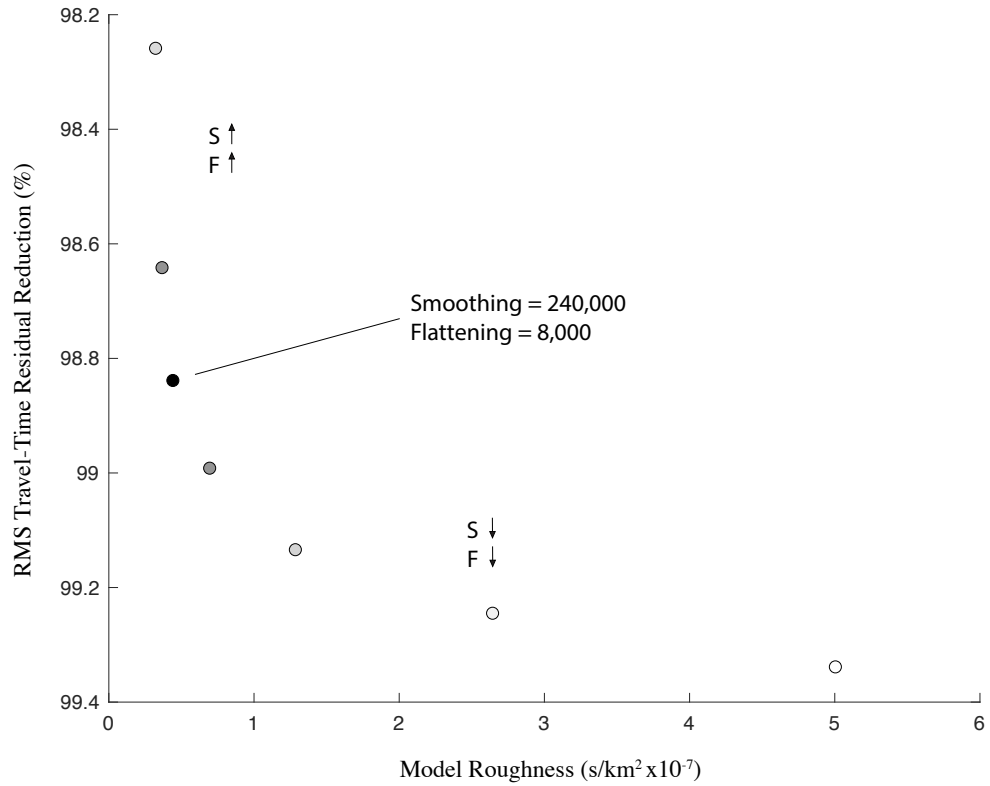


Figure A-2: Trade-off curve analysis for flattening and smoothing parameterization. Each circle represents a unique model run. Optimal parameterization decreases the RMS of travel-time residuals without increasing model roughness. Standard procedure is to choose parameterization that lies within the 'elbow' or bend of the trade-off curve (VanDecar, 1991).

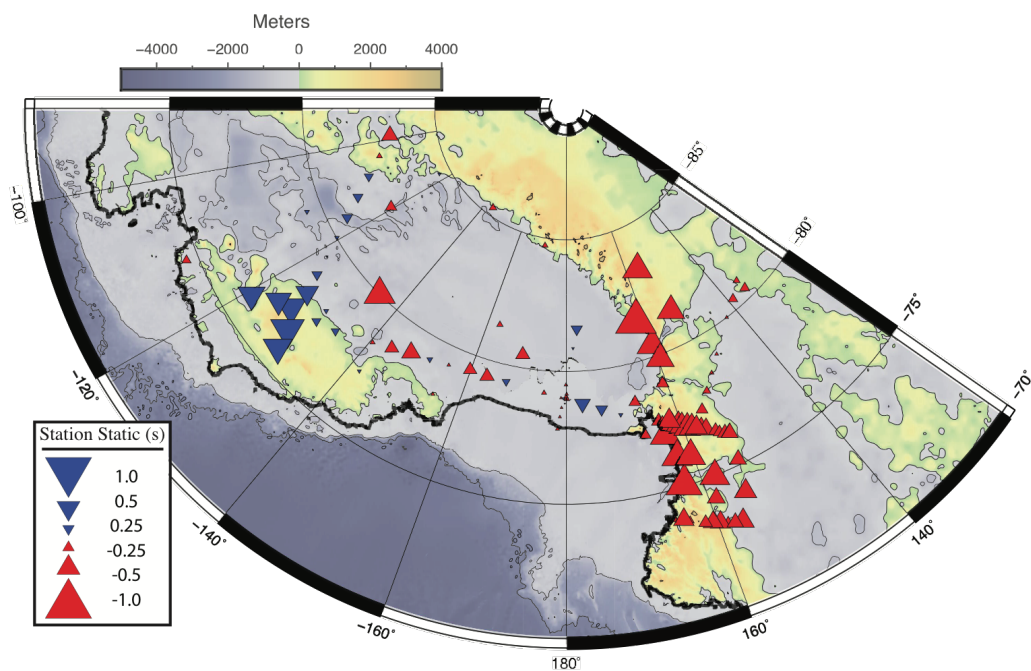


Figure A-3: Station static terms from the inversion output, plotted over bedrock topography from BEDMAP2 (Fretwell et al., 2013). These terms are subtracted from the relative arrival times to account for shallow structure. In regions with relatively thick, slow crust, positive station terms are subtracted from the arrival times, thereby reducing the overall relative arrival time for the given station. Likewise, for stations situated on thick, fast crust, negative station terms are subtracted, which relatively increase the arrival times.

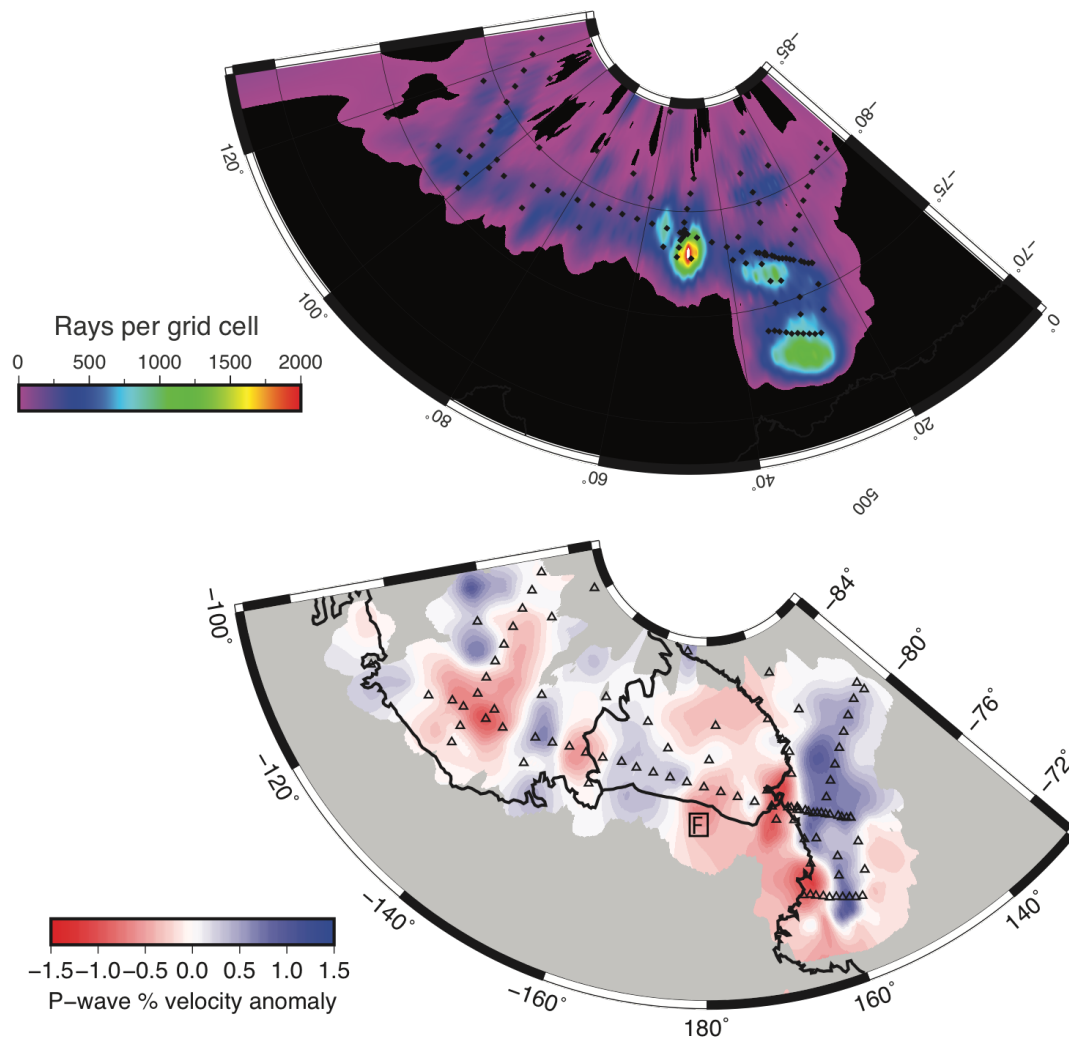


Figure A-4: (top) Rays per grid cell (Fig. A-1) determined from ray tracing using the station and event geometry employed in our final model. Warm colors represent regions with higher ray density. Note that in the central RIS, there is a small region with very high ray density due to the dense cluster of DRIS stations. (bottom) Model results obtained after removing the DRIS station observations. This was performed to decrease the ray density in the central RIS. Note that the high amplitude, low velocity feature (Anomaly F) in the central RIS is now diminished.

Appendix B

Supplemental Figures for Chapter 3

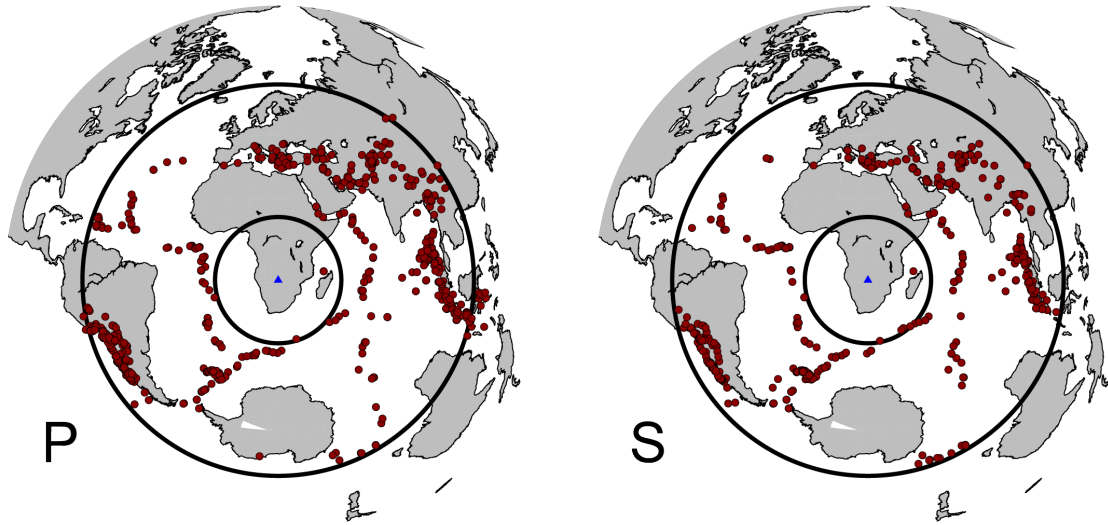


Figure B-1: Location of earthquakes used to measure relative arrival times for the P-wave (left) and S-wave (right) models.

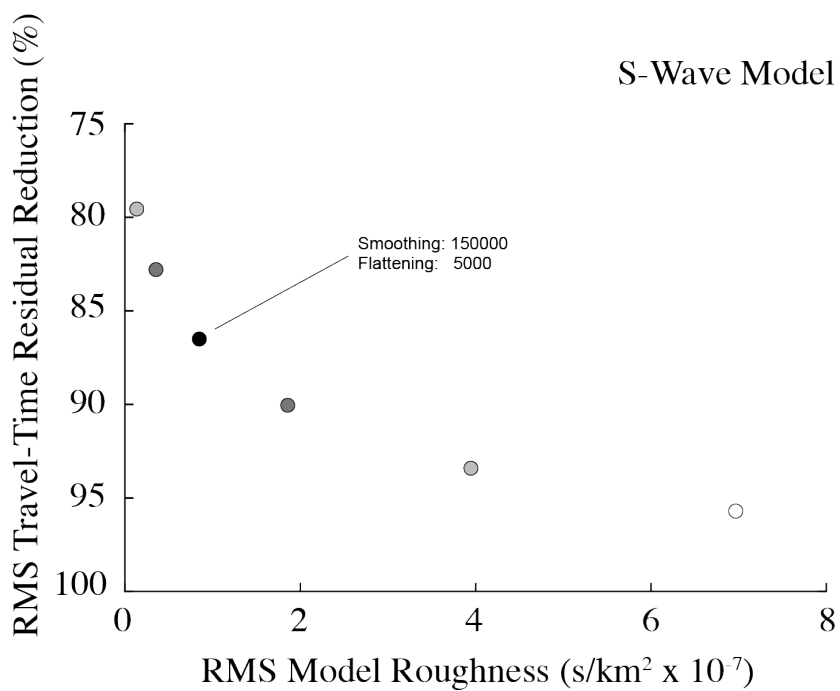
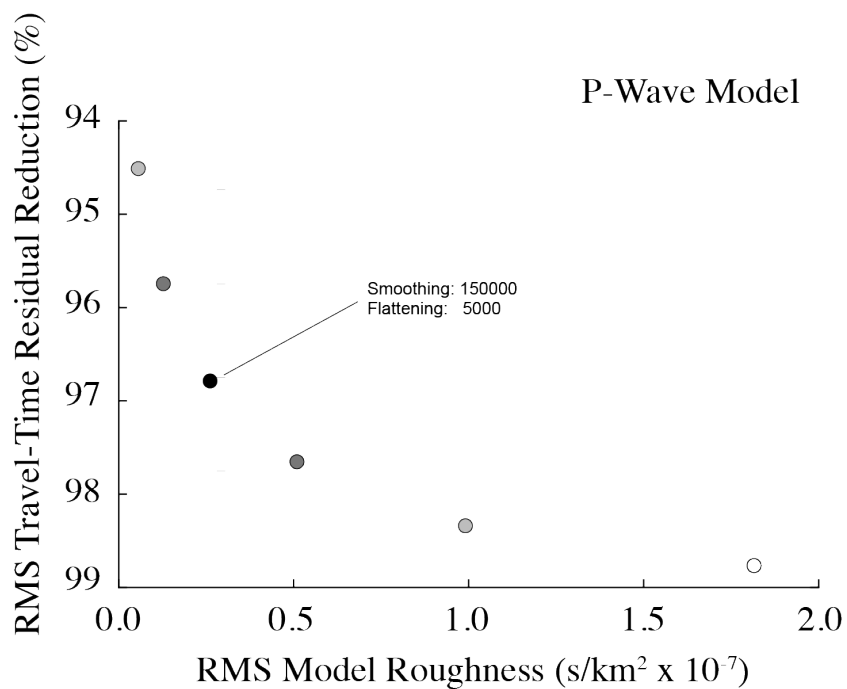


Figure B-2: Trade-off curves for regularization parameterization. The chosen parameterization is listed in the figure. The RMS travel-time residual reduction accounts for the station static terms, the event relocation terms, and the 3D velocity models.

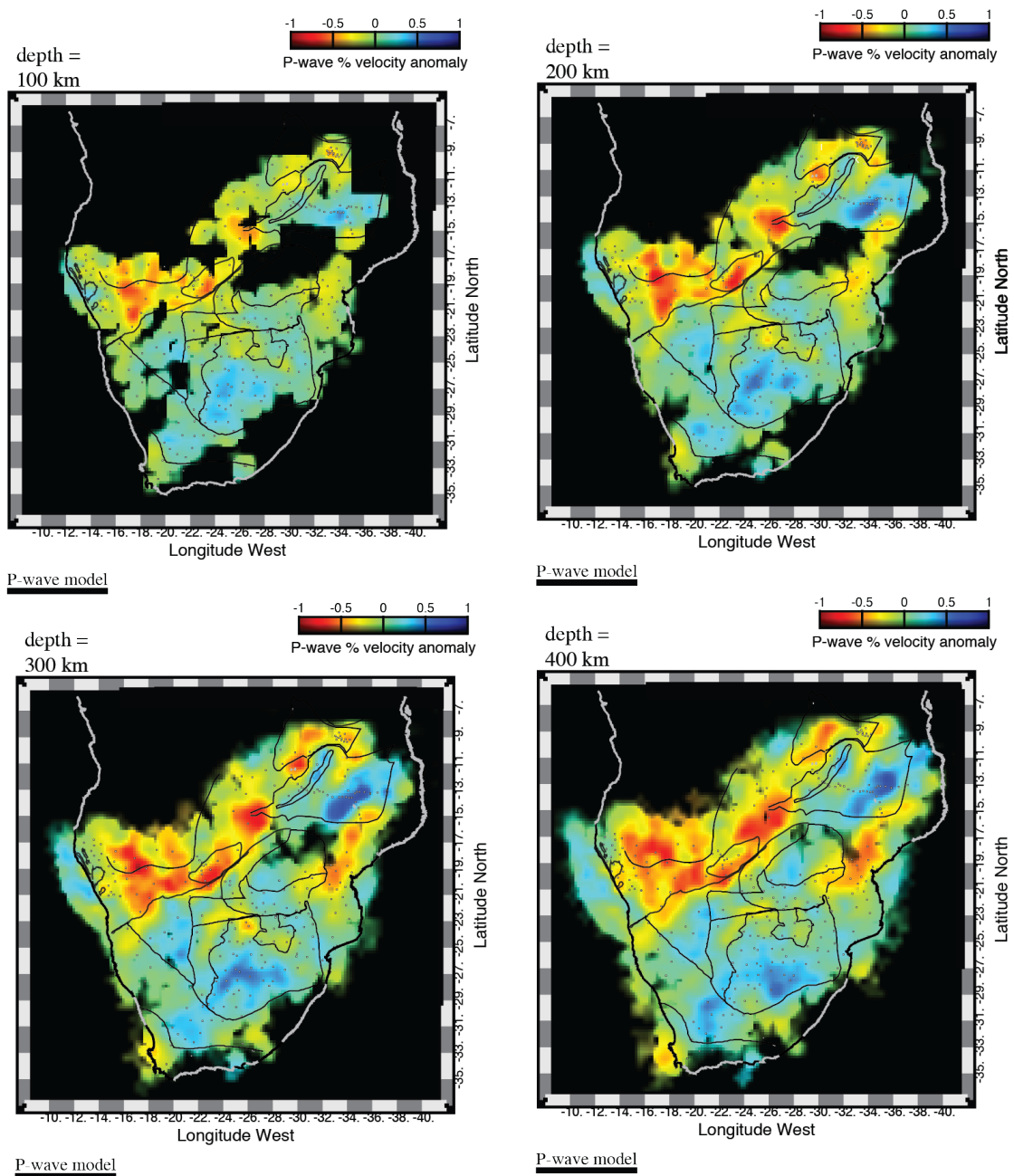


Figure B-3: Horizontal cross-sections through the P-wave model at 100 km intervals. Tectonic boundaries (Begg et al., 2009; Frimmel and Frank, 1998) are marked by black lines.

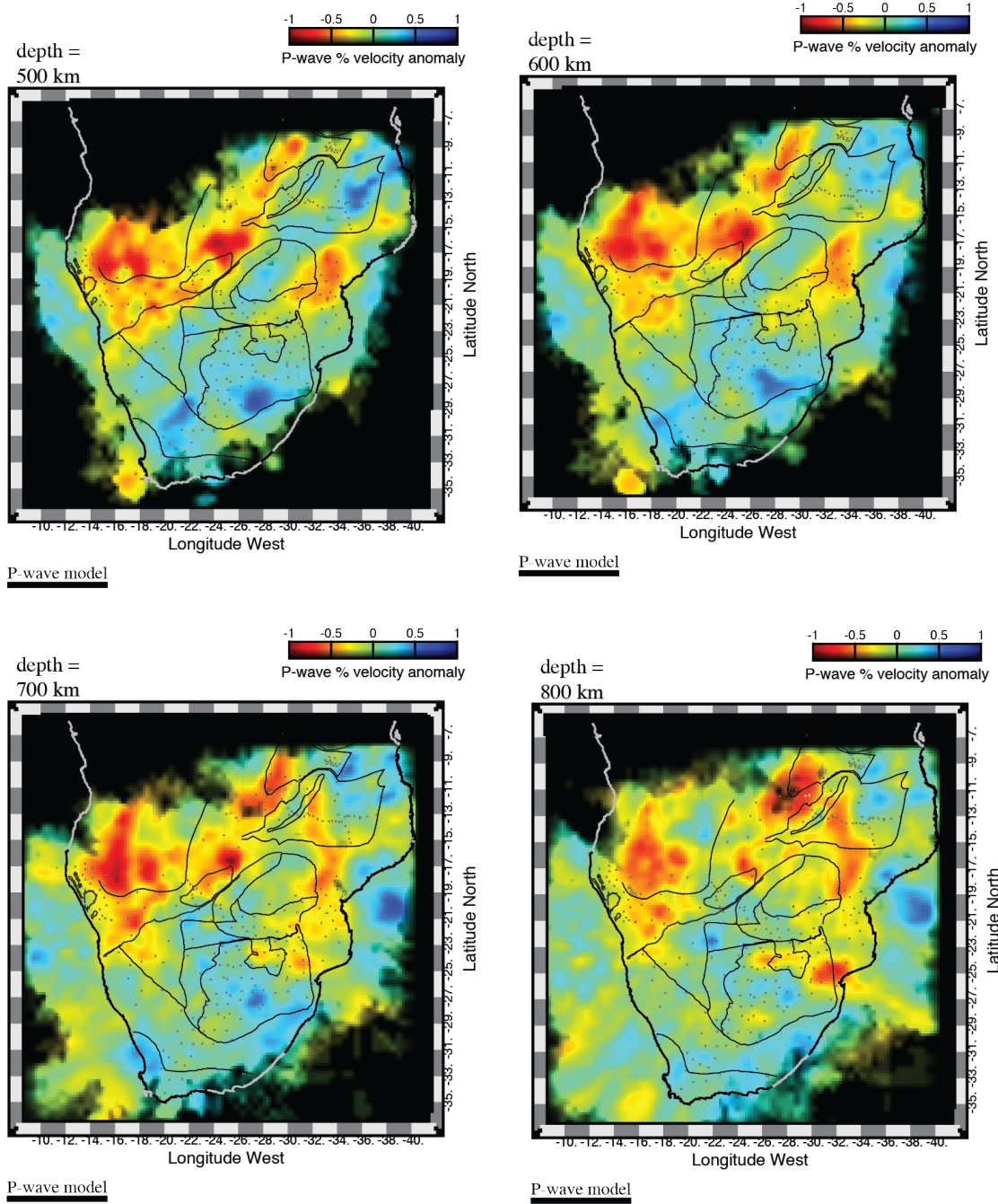


Figure B-3 continued: Horizontal cross-sections through the P-wave model at 100 km intervals. Tectonic boundaries (Begg et al., 2009; Frimmel and Frank, 1998) are marked by black lines.

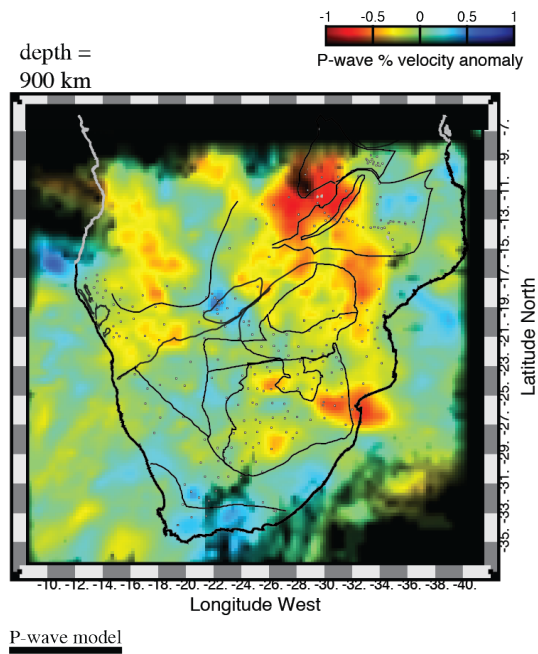


Figure **B-3 continued**: Horizontal cross-sections through the P-wave model at 100 km intervals. Tectonic boundaries (Begg et al., 2009; Frimmel and Frank, 1998) are marked by black lines.

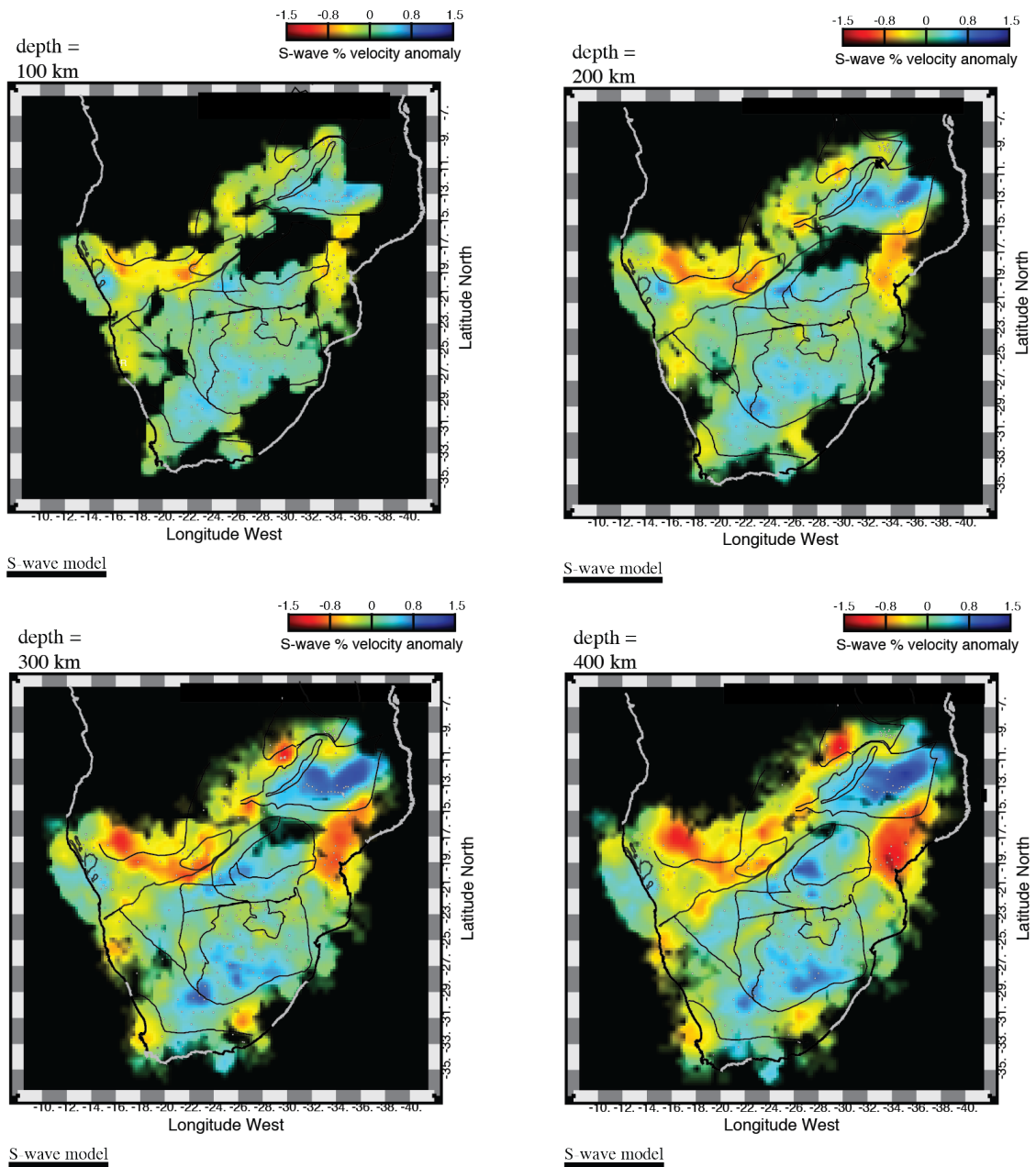


Figure B-4: Horizontal cross-sections through the S-wave model at 100 km intervals. Tectonic boundaries (Begg et al., 2009; Frimmel and Frank, 1998) are marked by black lines.

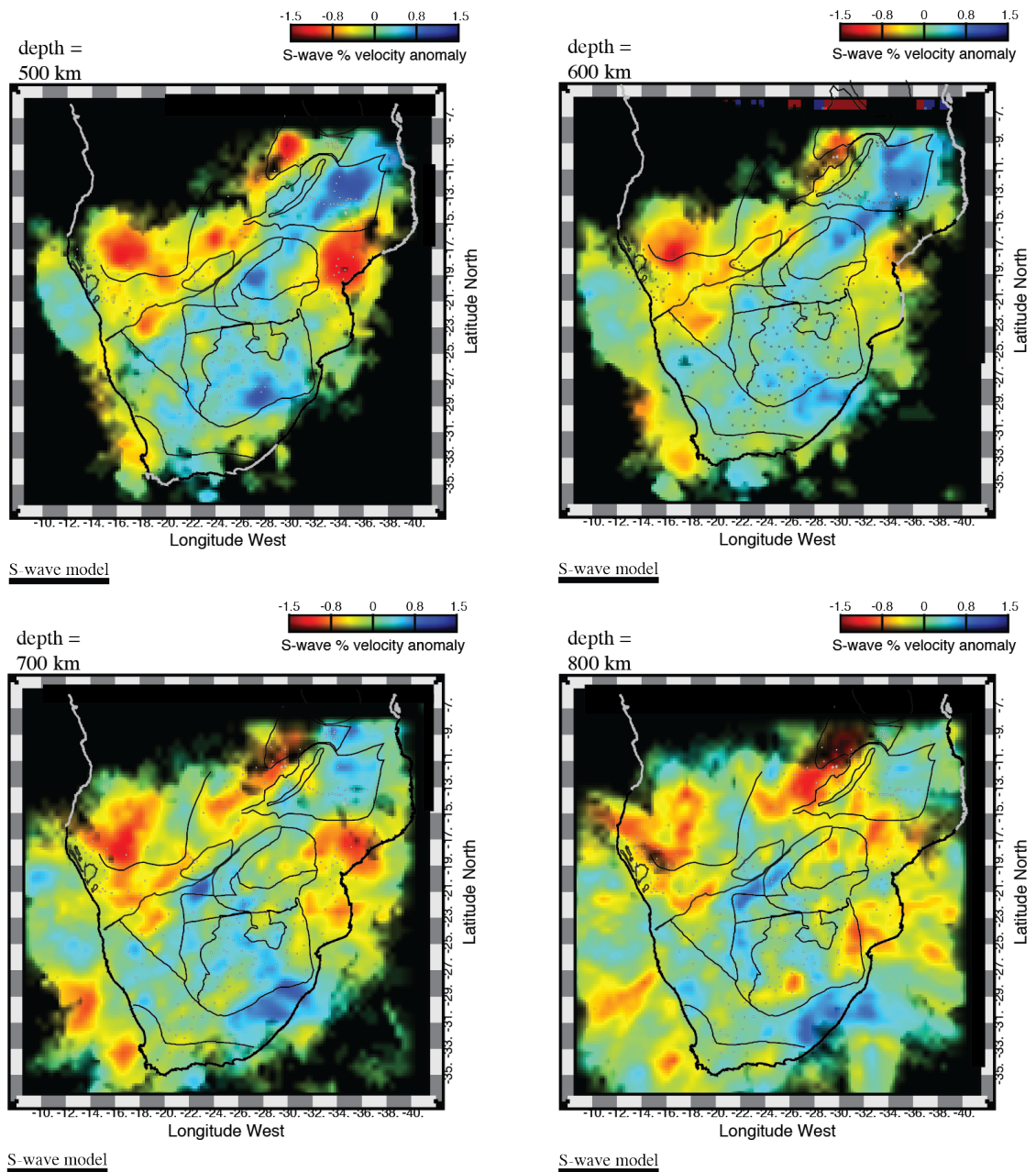


Figure **B-4 continued**: Horizontal cross-sections through the S-wave model at 100 km intervals. Tectonic boundaries (Begg et al., 2009; Frimmel and Frank, 1998) are marked by black lines.

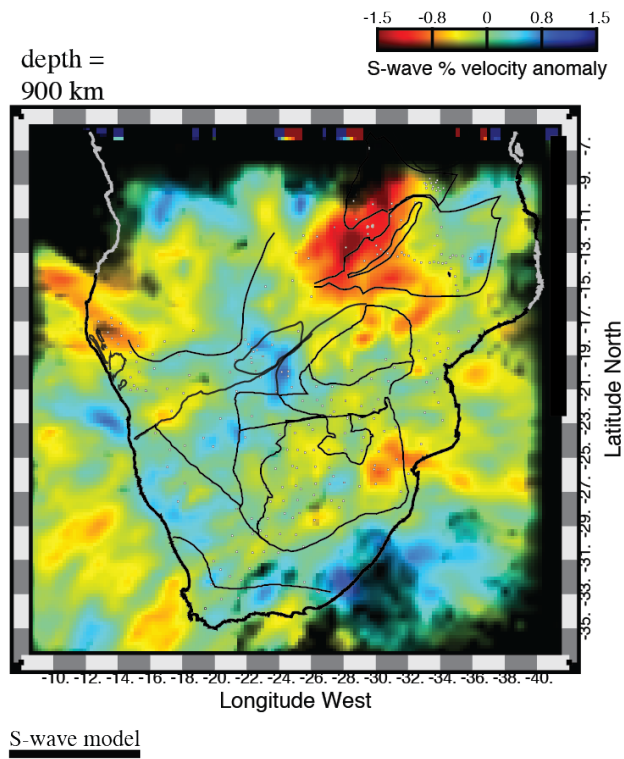


Figure **B-4 continued**: Horizontal cross-sections through the S-wave model at 100 km intervals. Tectonic boundaries (Begg et al., 2009; Frimmel and Frank, 1998) are marked by black lines.

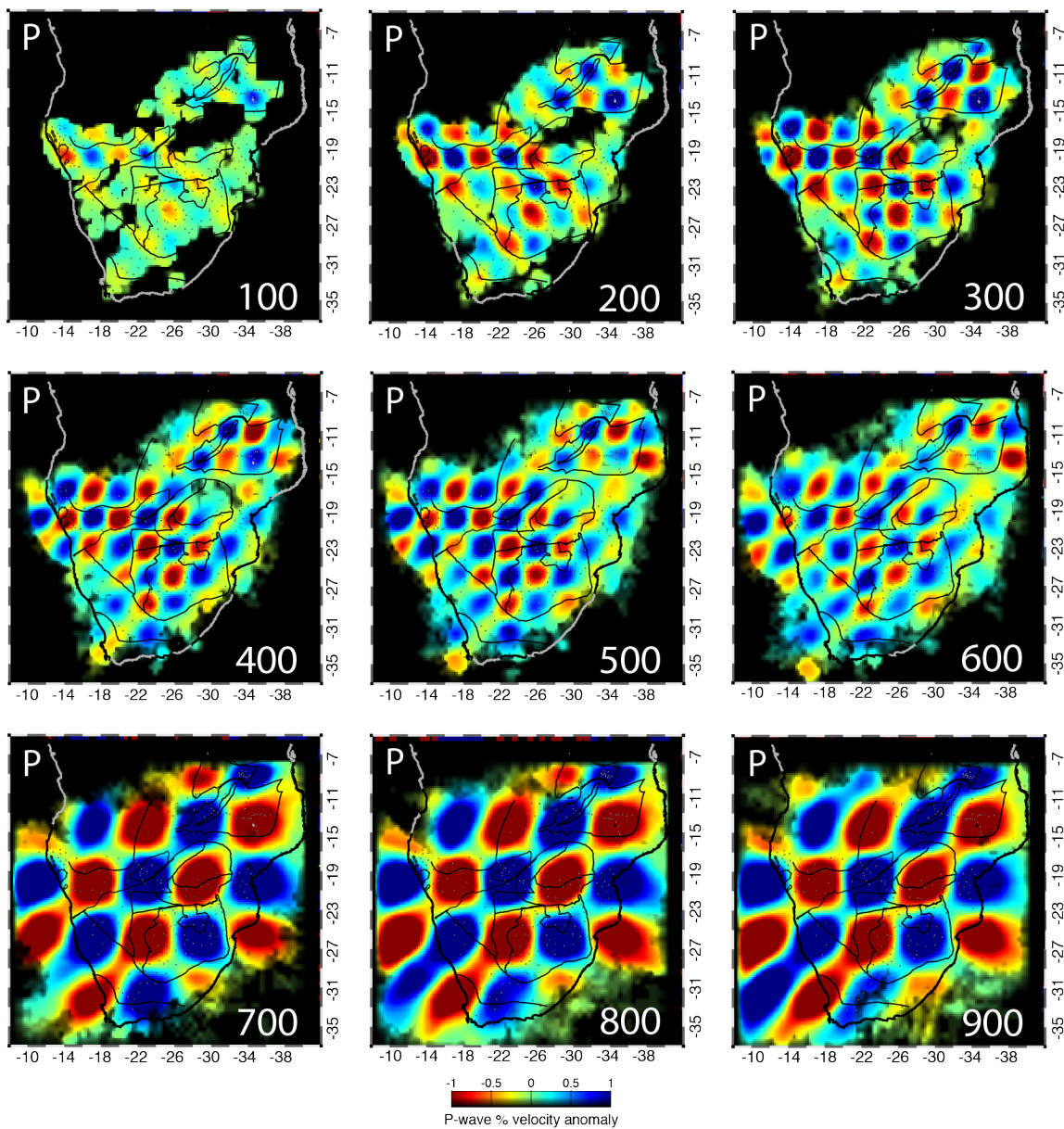


Figure **B-5**: Horizontal cross-sections through checkerboard synthetic test results for the P-wave model. The starting model consisted of $\pm 5\%$ spheres and a width at half maximum of 200 km. At 700 and greater depths, the width at half maximum was increased to 400 km.

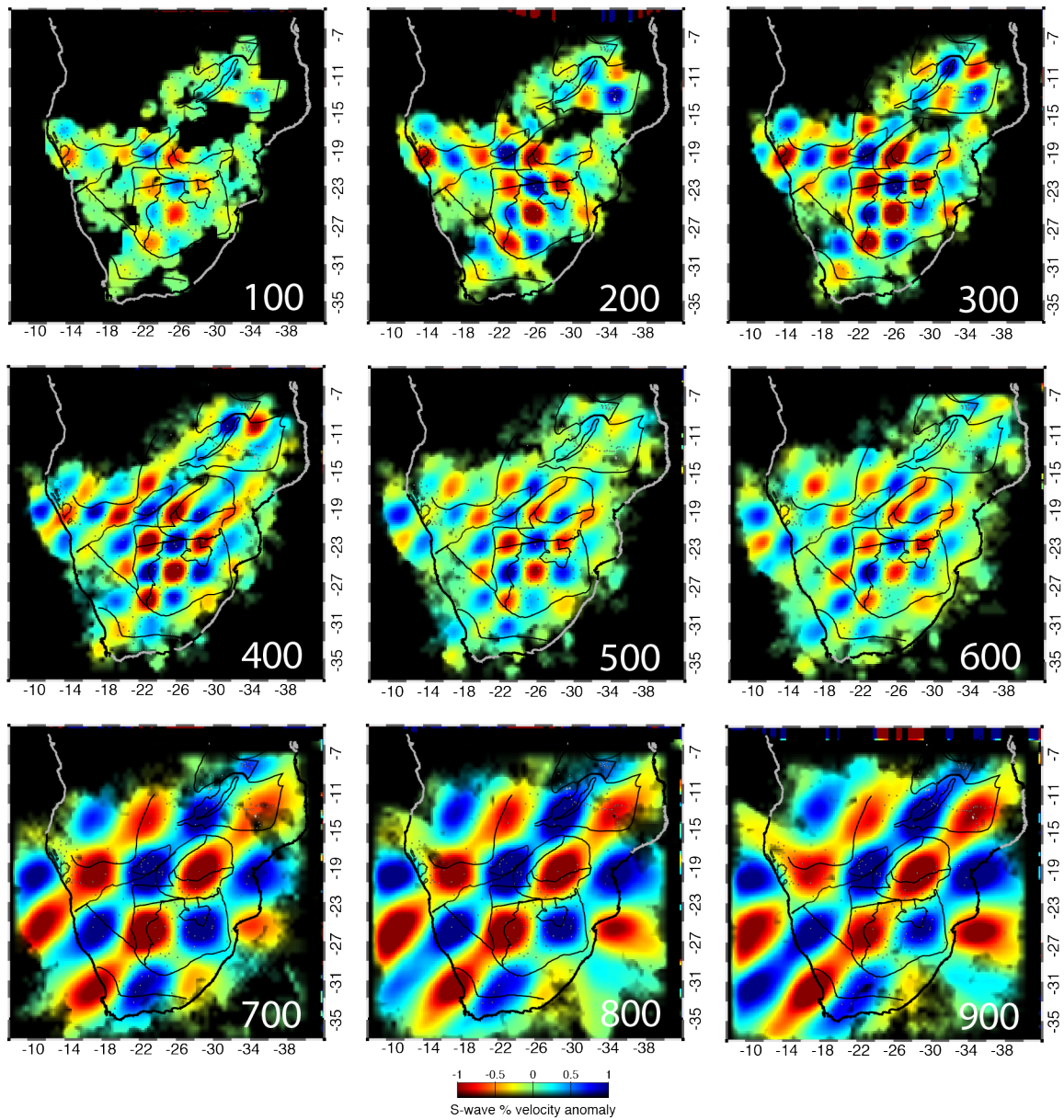


Figure B-6: Horizontal cross-sections through checkerboard synthetic test results for the S-wave model. The starting model consisted of $\pm 5\%$ spheres and a width at half maximum of 200 km. At 700 and greater depths, the width at half maximum was increased to 400 km.

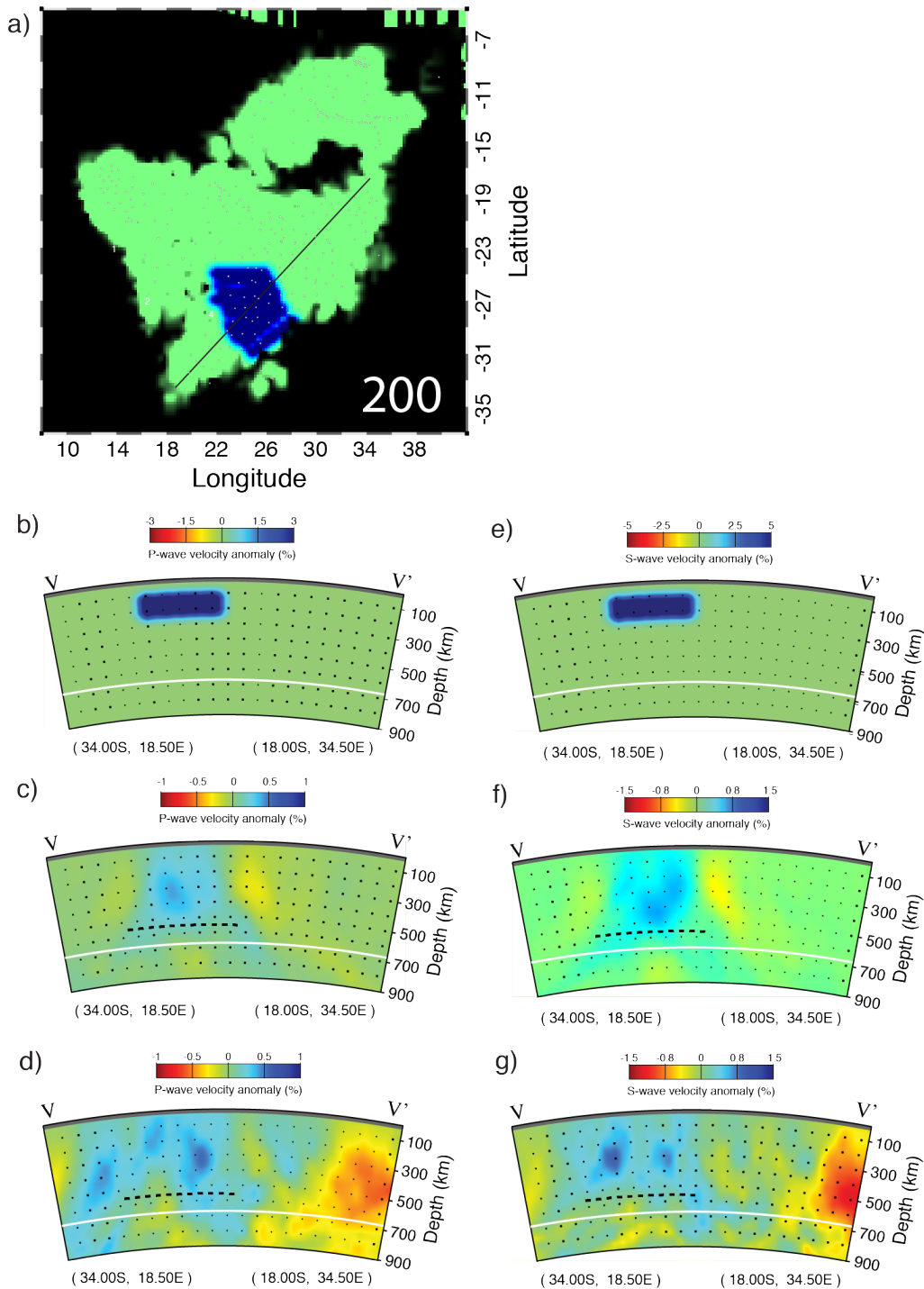


Figure B-7: a) Horizontal cross-section of a synthetic velocity model used to calculate relative travel-times. b) Vertical cross-section through a synthetic P-wave model. c) Results of the inversion of synthetic travel-times calculated through (b). d) Vertical cross-section V from the P-wave model. e) Vertical cross-section through a synthetic S-wave model used to calculate relative travel-times. f) Results of the inversion of travel-times calculated through (e). g) Vertical cross-section V through the S-wave model.

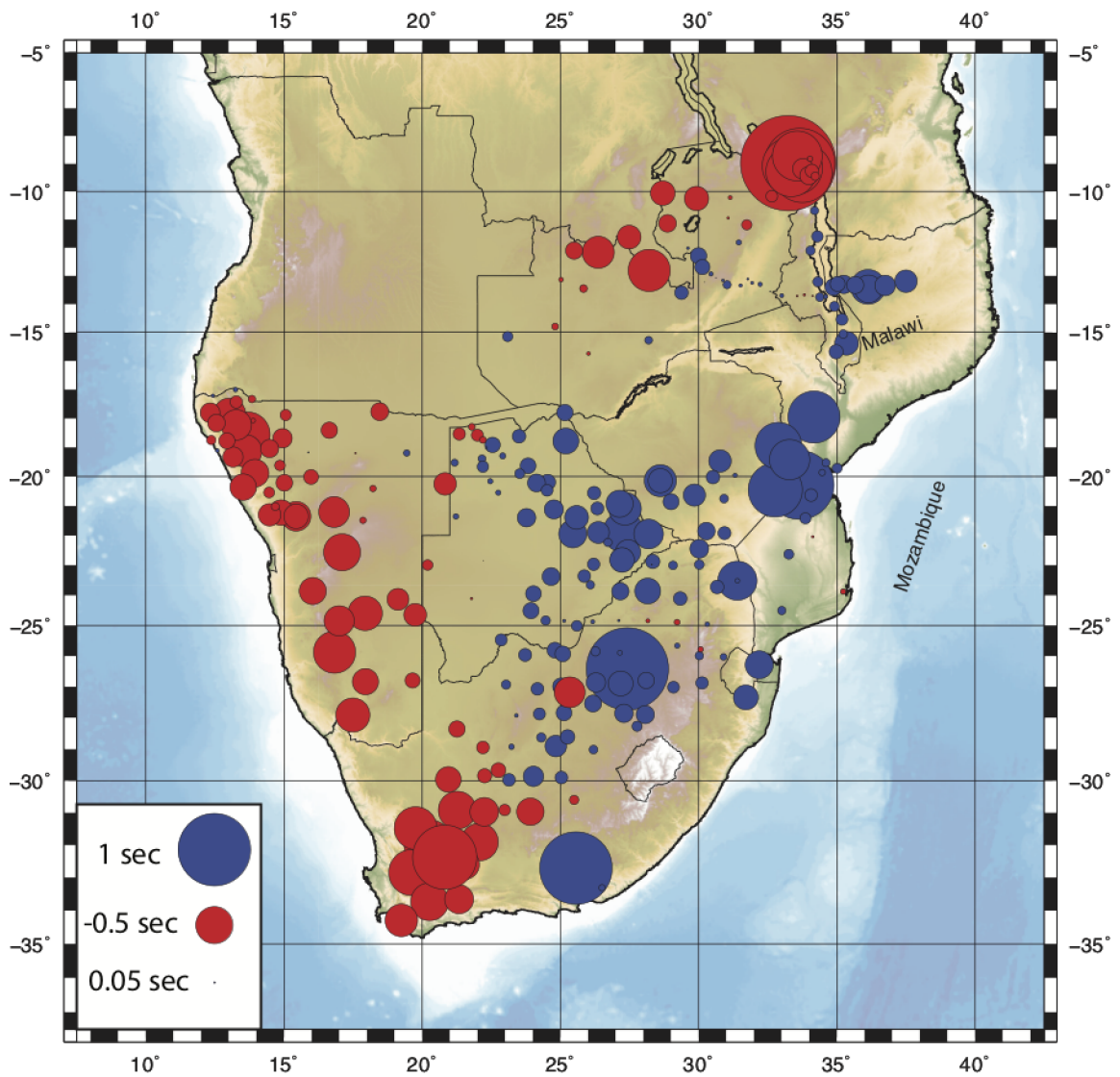


Figure B-8: Station static terms from the inversion output, plotted over topography from GEBCO (Weatherall et al., 2015). These terms are subtracted from the relative arrival times to account for shallow structure.

Appendix C

Supplemental Figures for Chapter 4

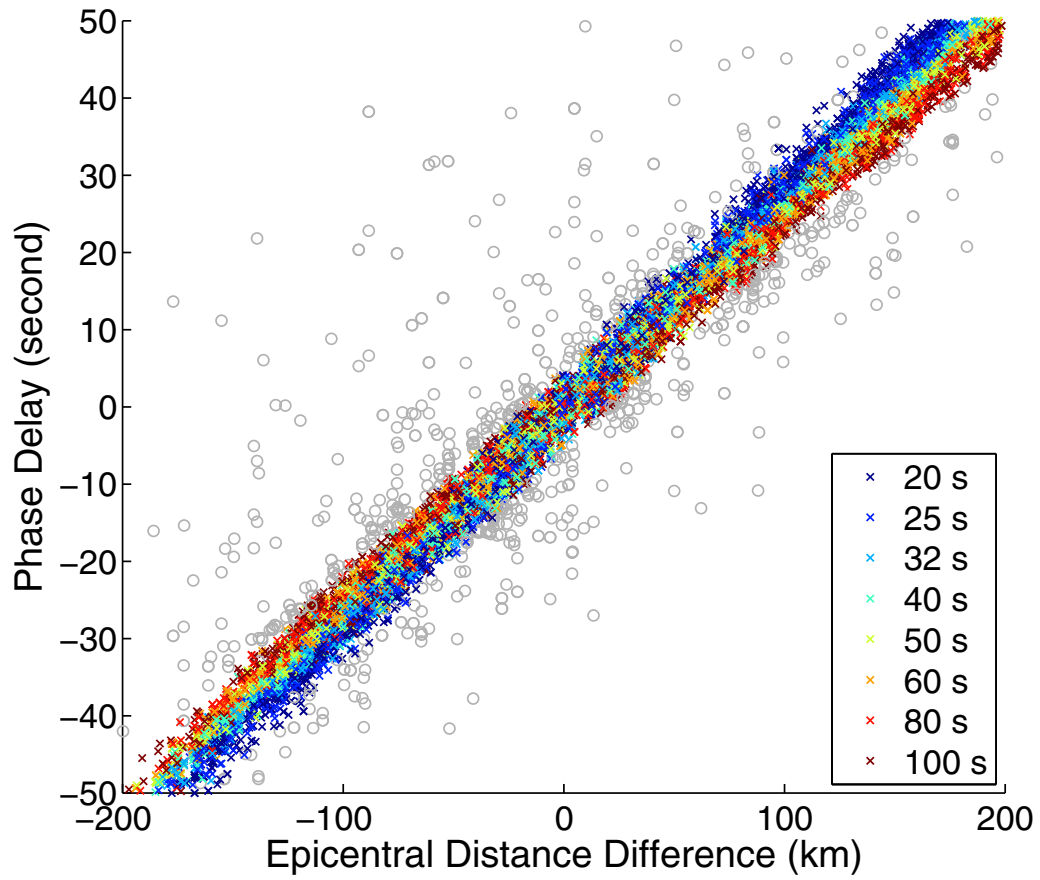


Figure C-1: Example relative phase delays versus epicentral distance difference between stations from Jin and Gaherty, 2015. Cooler colors show phase delay (seconds) measurements for shorter periods and warmer colors show phase delay measurements for longer periods. Gray circles show measurements that did not meet the quality control requirements outlined in Chapter 4. Differences in phase velocities manifest in different slopes in trend lines for the various periods. Negative epicentral distance differences occur when the reference station is further from the event hypocenter than the secondary station.

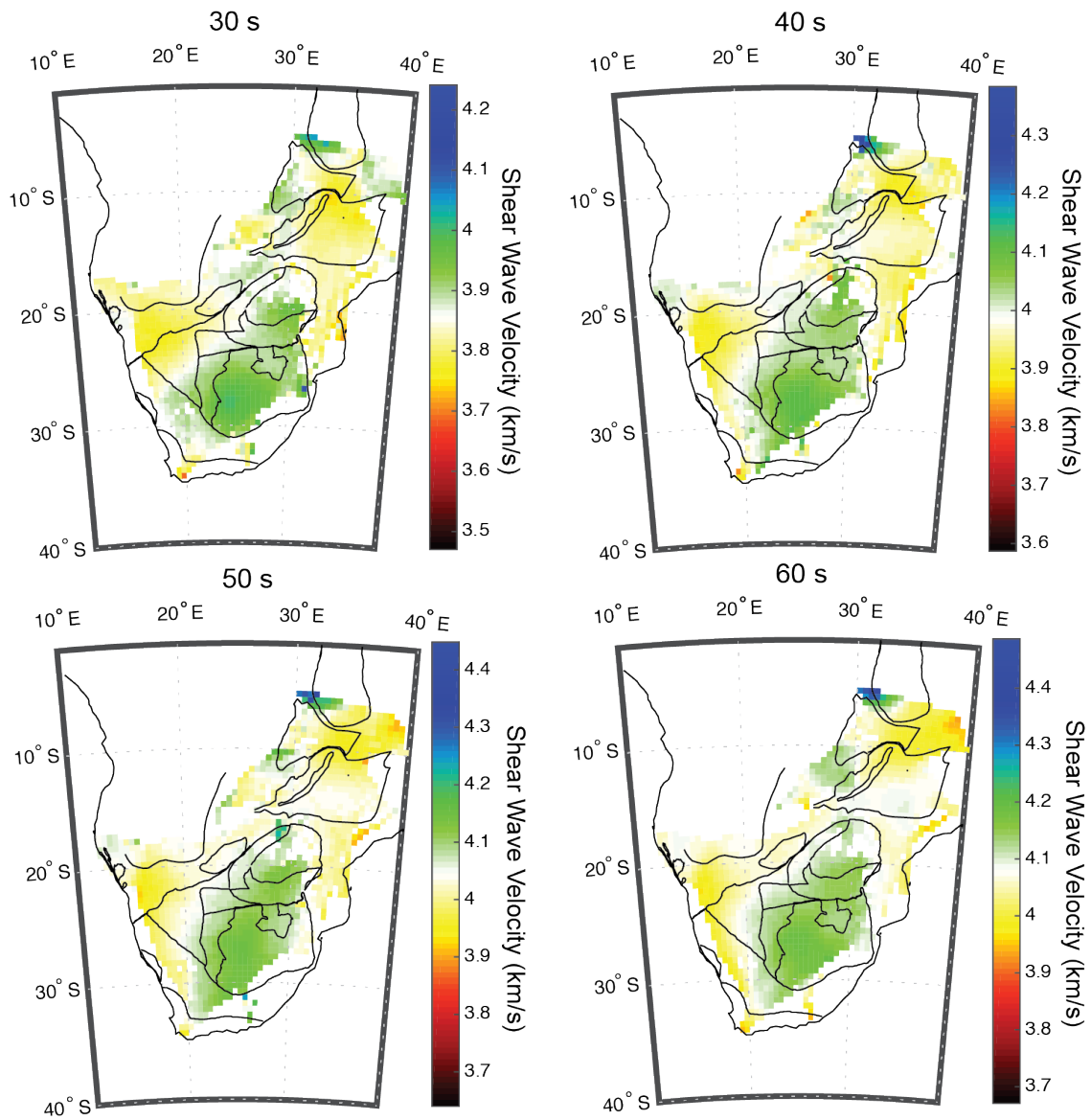


Figure C-2: Apparent phase velocity maps for all measured periods (30-200 s) from eikonal tomography. Tectonic boundaries (Begg et al., 2009; Frimmel and Frank, 1998) are marked by black lines.

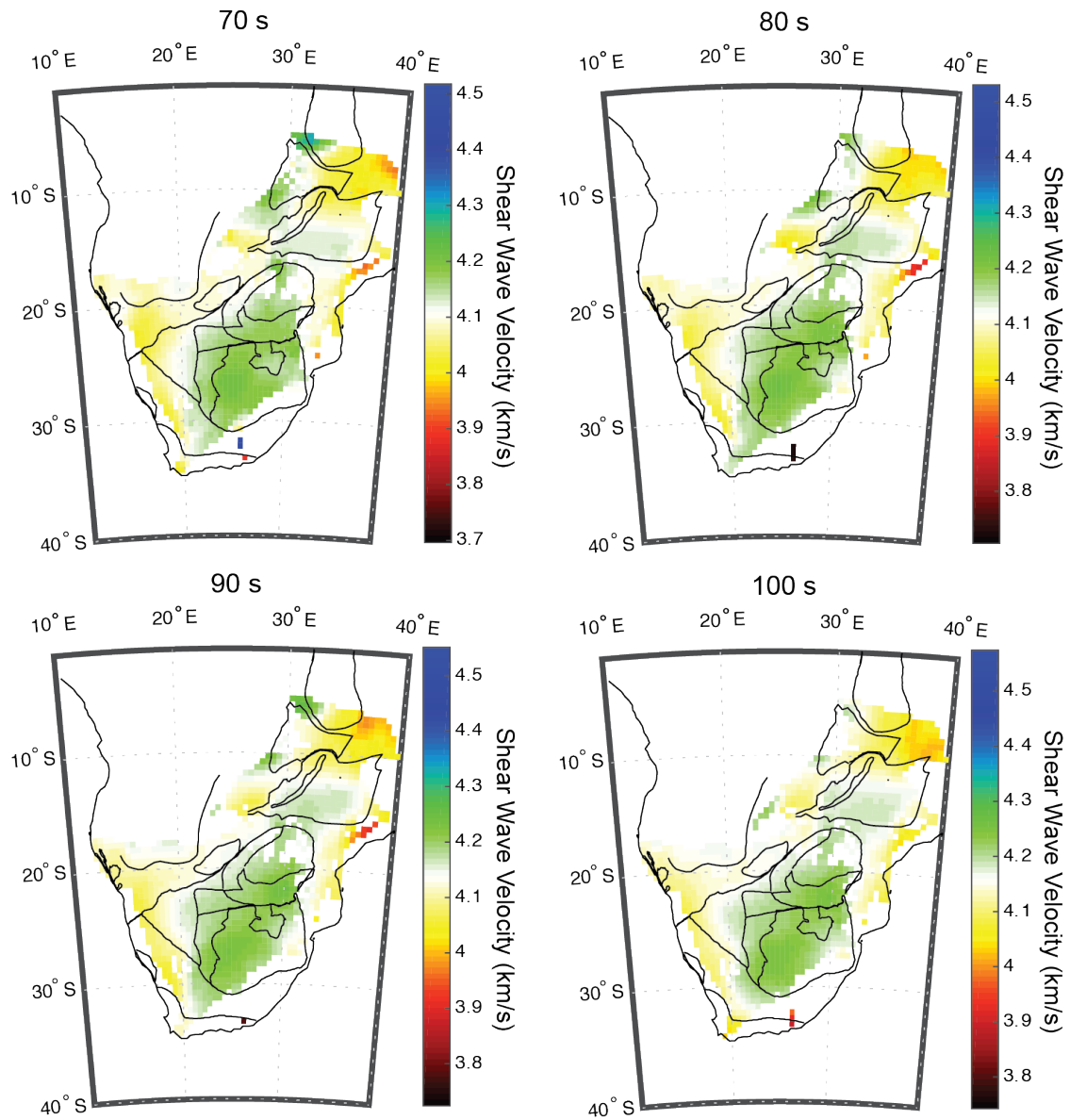


Figure C-2 **continued**: Apparent phase velocity maps for all measured periods (30-200 s) from eikonal tomography. Tectonic boundaries (Begg et al., 2009; Frimmel and Frank, 1998) are marked by black lines.

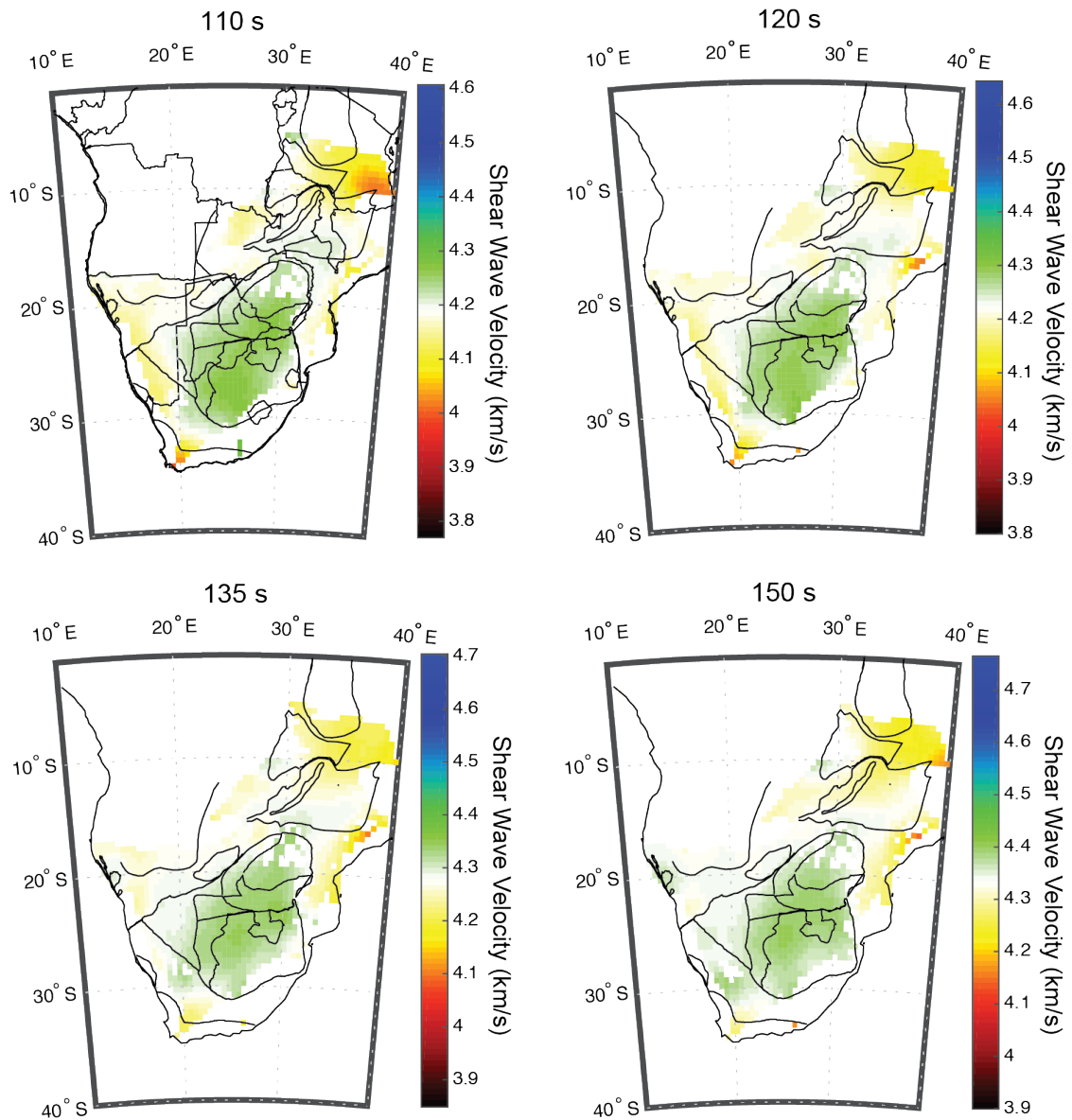


Figure C-2 continued: Apparent phase velocity maps for all measured periods (30-200 s) from eikonal tomography. Tectonic boundaries (Begg et al., 2009; Frimmel and Frank, 1998) are marked by black lines.

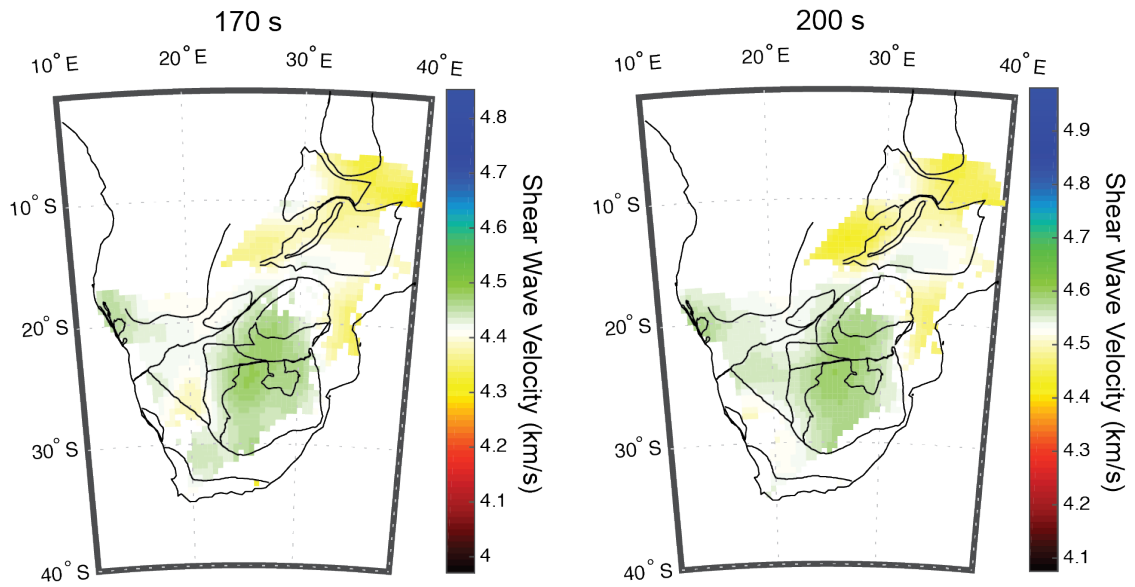


Figure C-2 **continued**: Apparent phase velocity maps for all measured periods (30-200 s) from eikonal tomography. Tectonic boundaries (Begg et al., 2009; Frimmel and Frank, 1998) are marked by black lines.

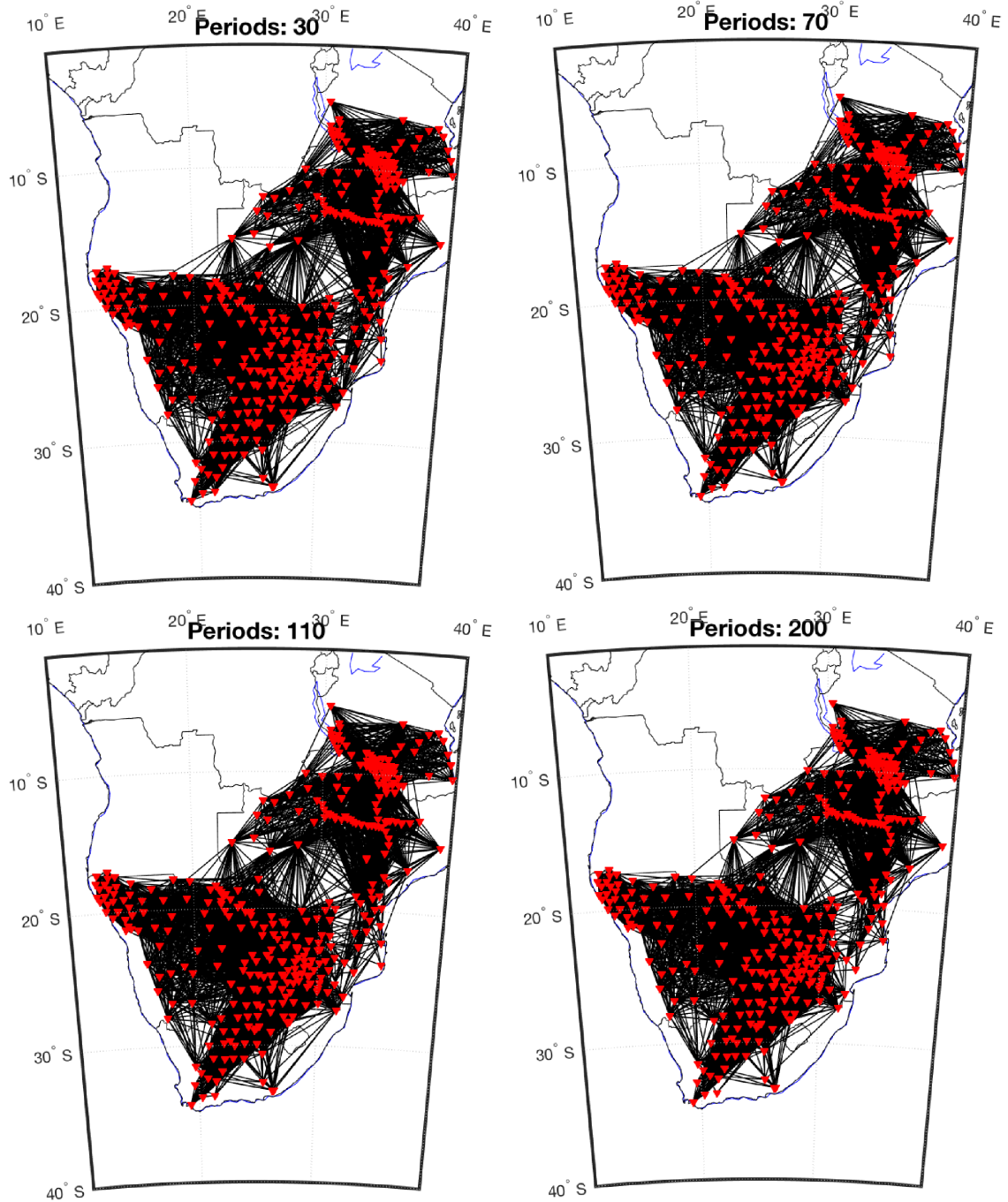


Figure C-3: Connected stations used for cross-correlations with maximum interstation spacing of 850 km and minimum spacing of 20 km for 30, 70, 110, and 200 s period Rayleigh waves.

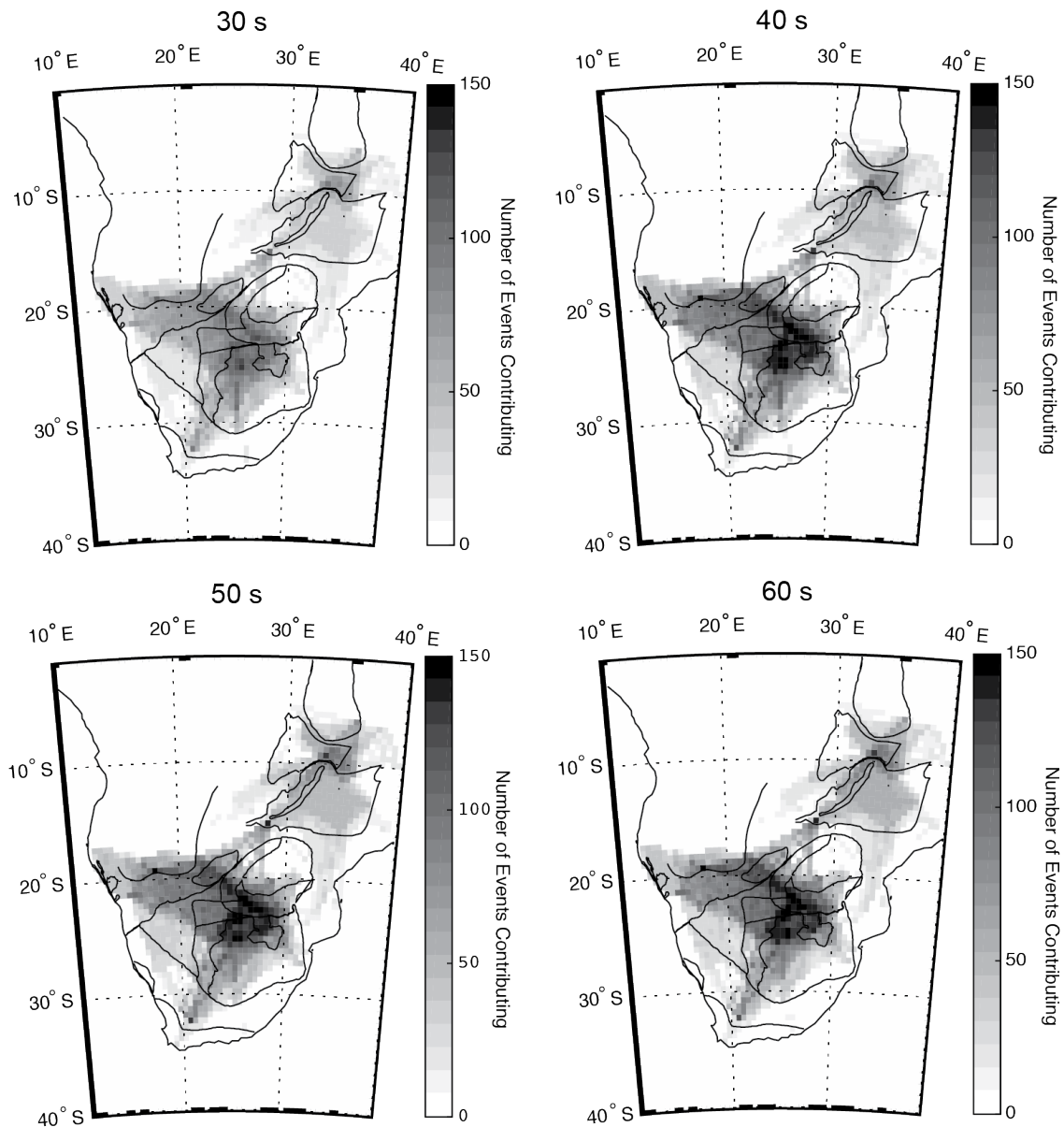


Figure C-4: Number of events contributing to each cell for the phase velocity inversion. This gives a rough estimate of the data distribution, but does not represent the total number of measurements that contribute to each cell, which can include multiple crossing rays per event. Tectonic boundaries (Begg et al., 2009; Frimmel and Frank, 1998) are marked by black lines.

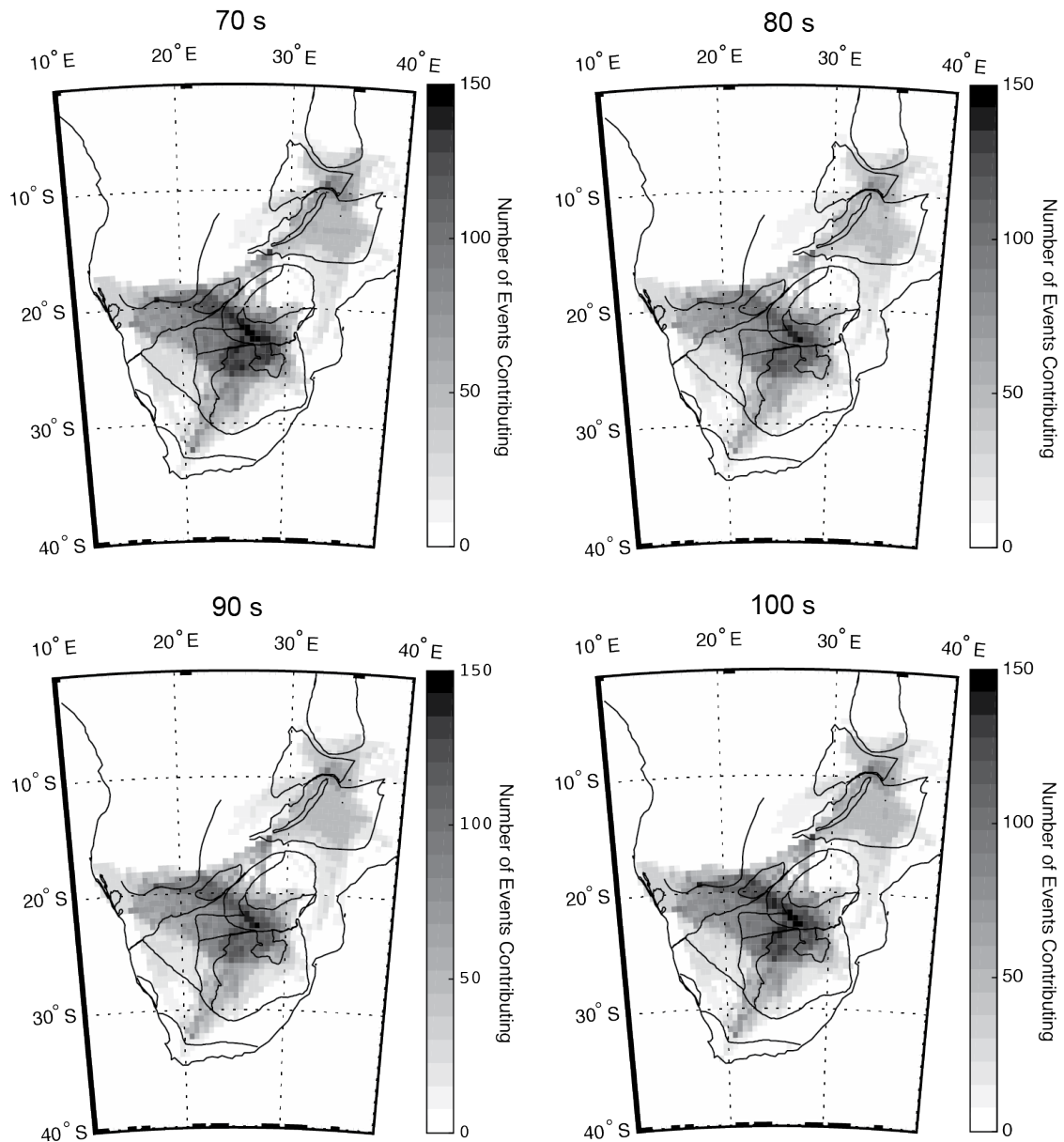


Figure C-4 **continued**: Number of events contributing to each cell for the phase velocity inversion. This gives a rough estimate of the data distribution, but does not represent the total number of measurements that contribute to each cell, which can include multiple crossing rays per event. Tectonic boundaries (Begg et al., 2009; Frimmel and Frank, 1998) are marked by black lines.

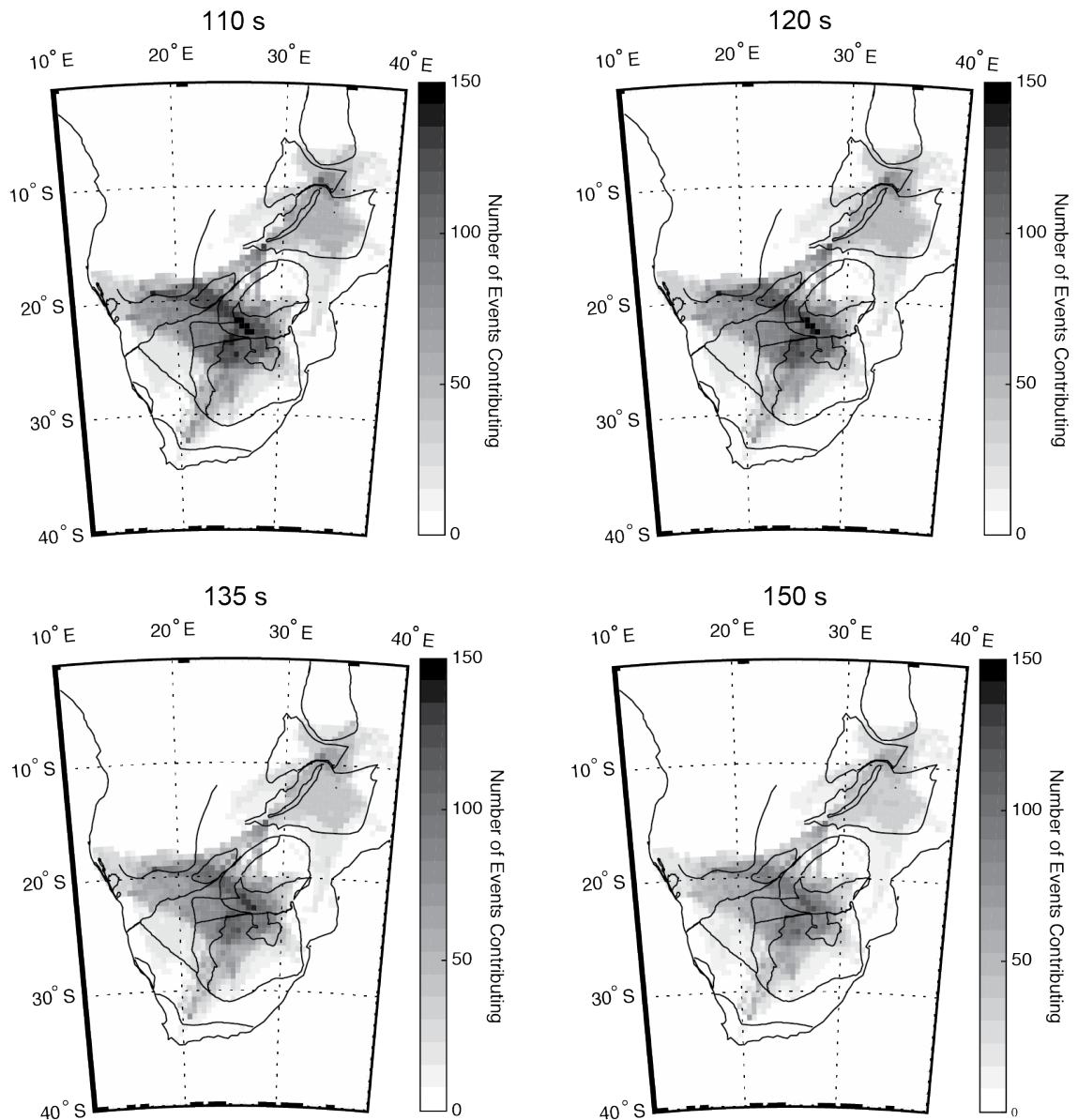


Figure C-4 **continued**: Number of events contributing to each cell for the phase velocity inversion. This gives a rough estimate of the data distribution, but does not represent the total number of measurements that contribute to each cell, which can include multiple crossing rays per event. Tectonic boundaries (Begg et al., 2009; Frimmel and Frank, 1998) are marked by black lines.

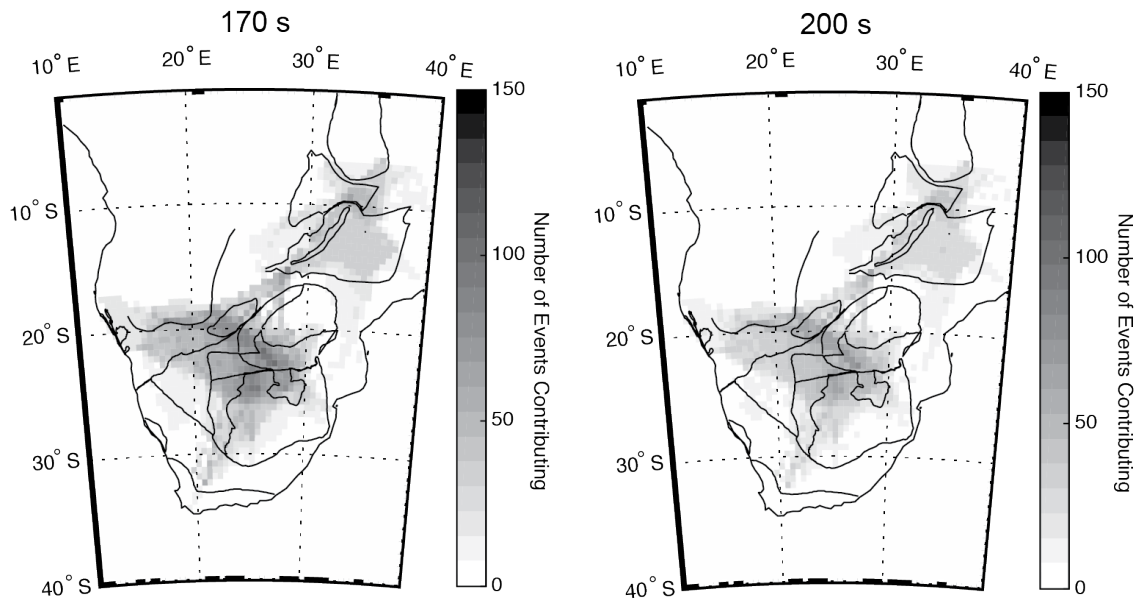


Figure C-4 continued: Number of events contributing to each cell for the phase velocity inversion. This gives a rough estimate of the data distribution, but does not represent the total number of measurements that contribute to each cell, which can include multiple crossing rays per event. Tectonic boundaries (Begg et al., 2009; Frimmel and Frank, 1998) are marked by black lines.

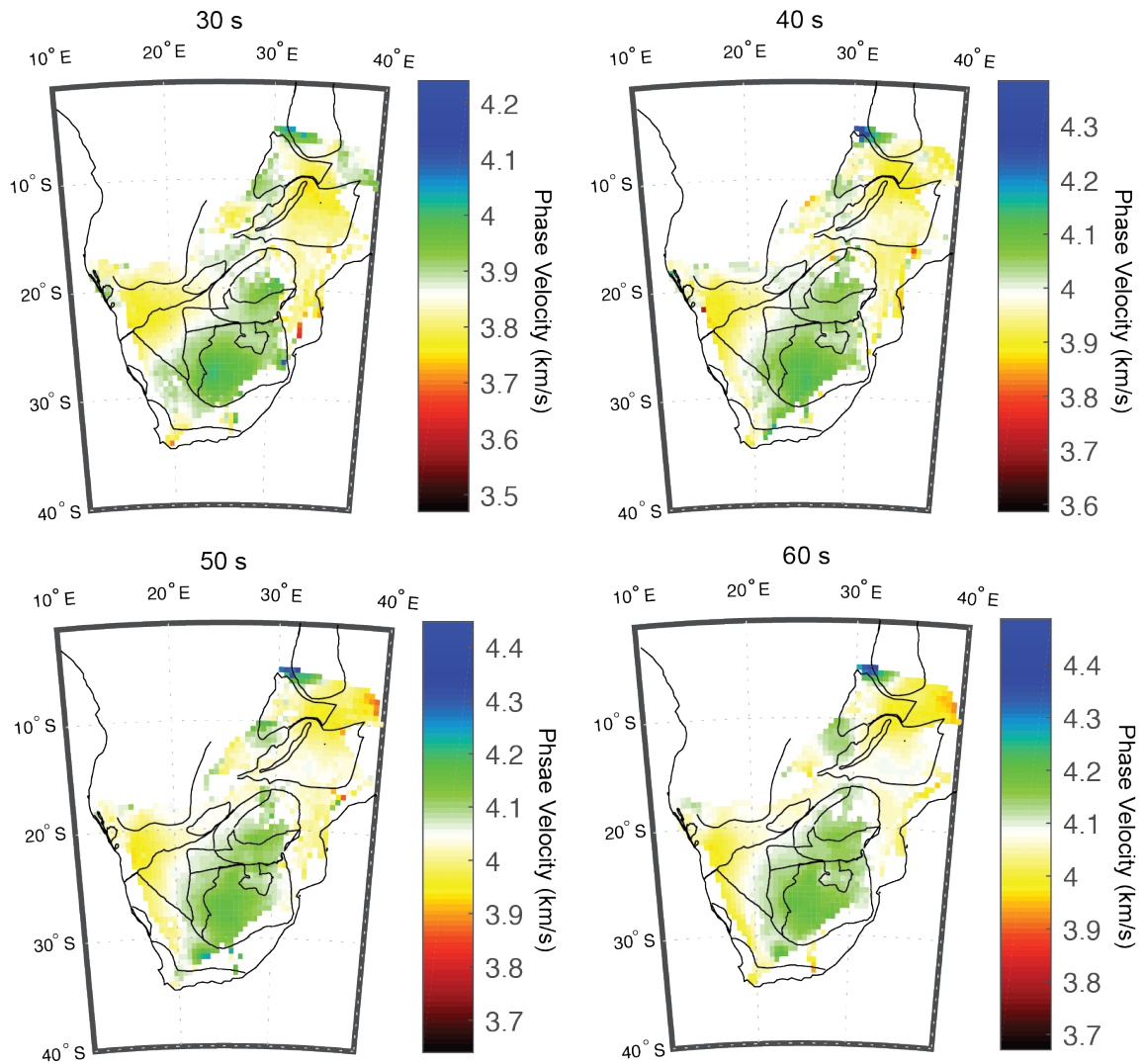


Figure C-5: Structural phase velocity maps for all measured periods (30-200 s) from Helmholtz tomography. Tectonic boundaries (Begg et al., 2009; Frimmel and Frank, 1998) are marked by black lines.

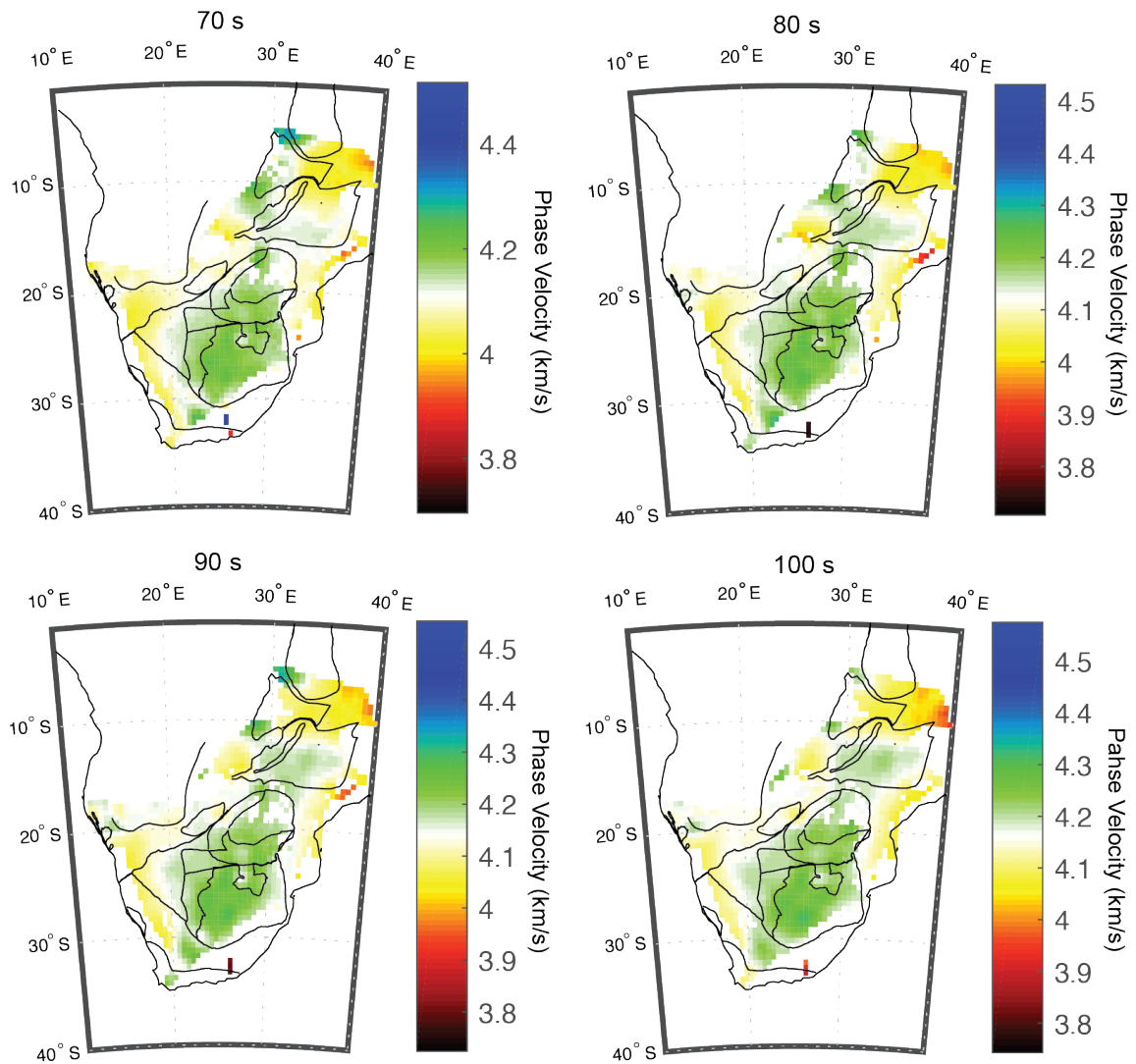


Figure C-5 continued: Structural phase velocity maps for all measured periods (30-200 s) from Helmholtz tomography. Tectonic boundaries (Begg et al., 2009; Frimmel and Frank, 1998) are marked by black lines.

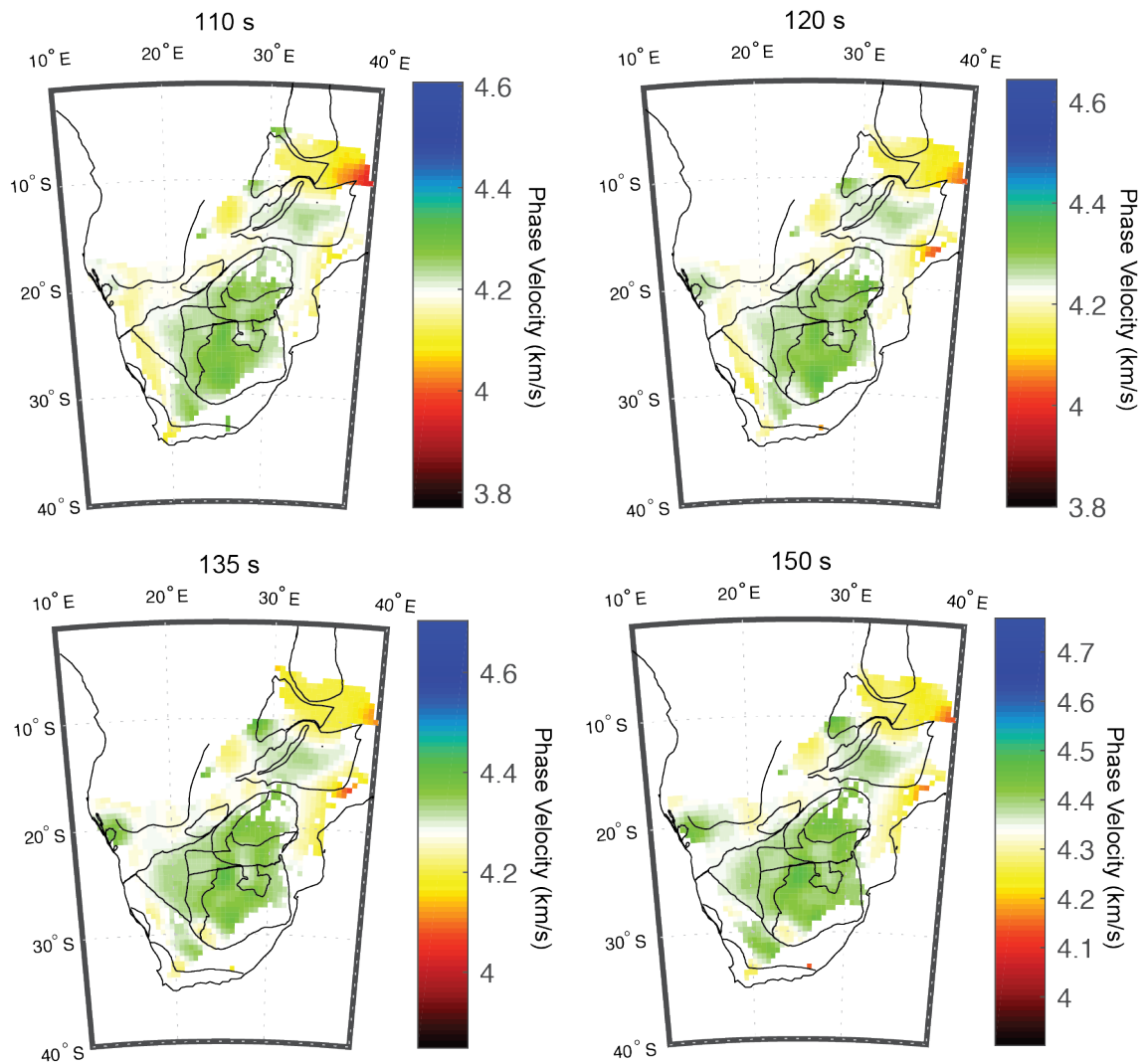


Figure C-5 **continued**: Structural phase velocity maps for all measured periods (30-200 s) from Helmholtz tomography. Tectonic boundaries (Begg et al., 2009; Frimmel and Frank, 1998) are marked by black lines.

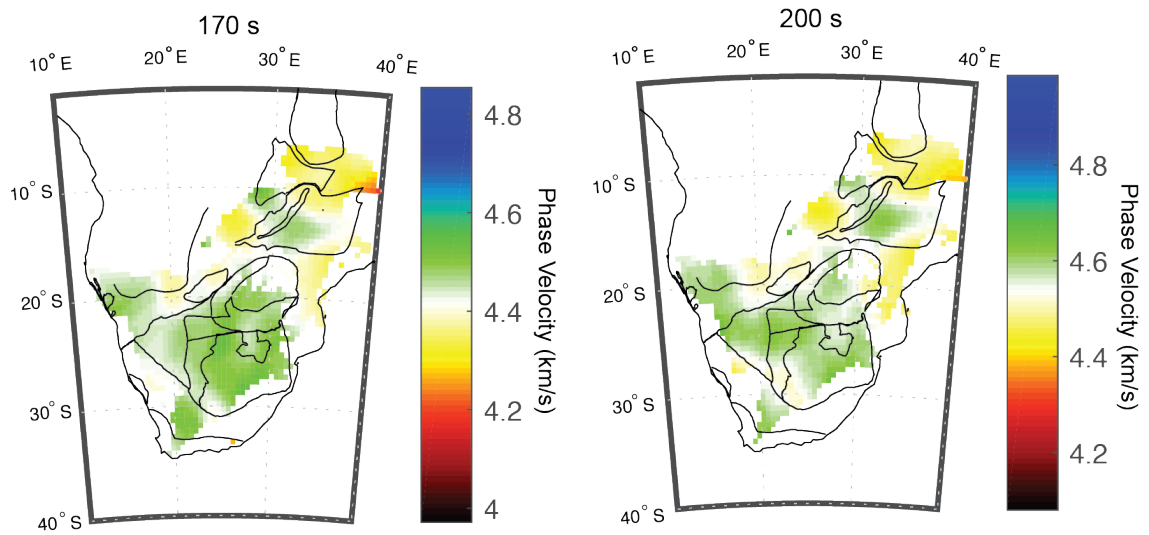


Figure C-5 continued: Structural phase velocity maps for all measured periods (30-200 s) from Helmholtz tomography. Tectonic boundaries (Begg et al., 2009; Frimmel and Frank, 1998) are marked by black lines.

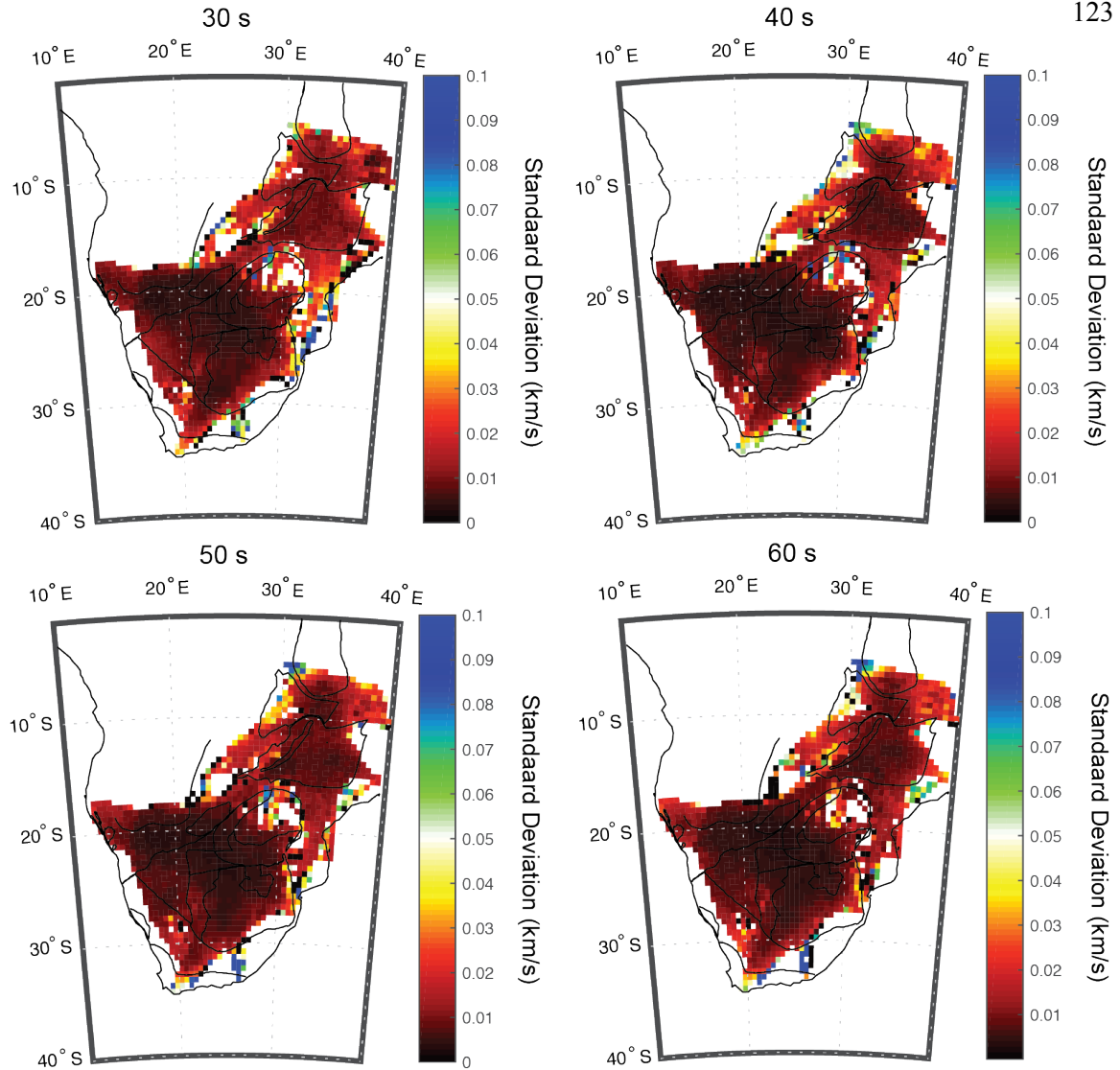


Figure C-6: Estimates of the standard deviation in phase velocity from stacking phase velocity maps driven from eikonal tomography

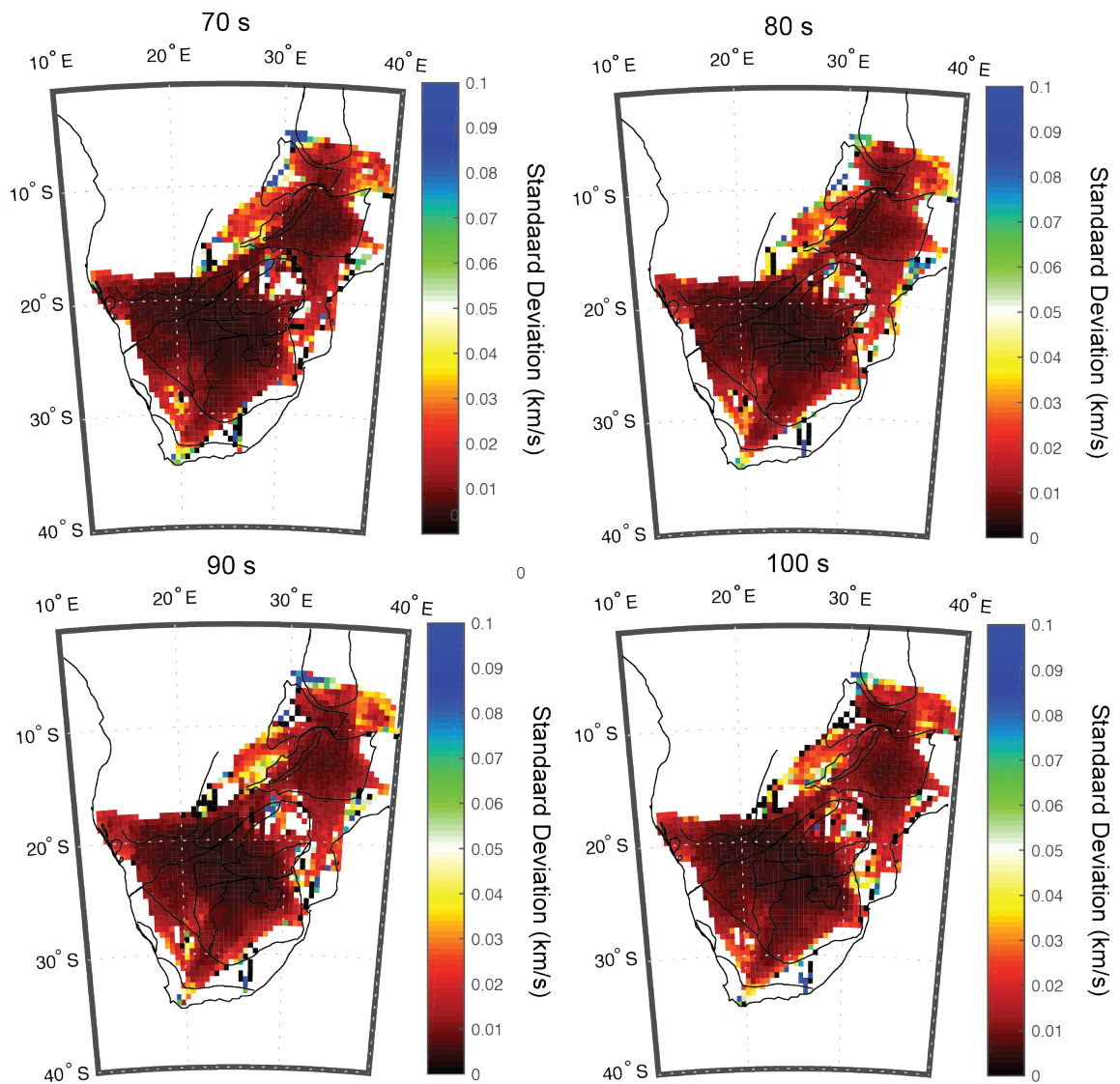


Figure C-6 continued: Estimates of the standard deviation in phase velocity from stacking phase velocity maps driven from eikonal tomography

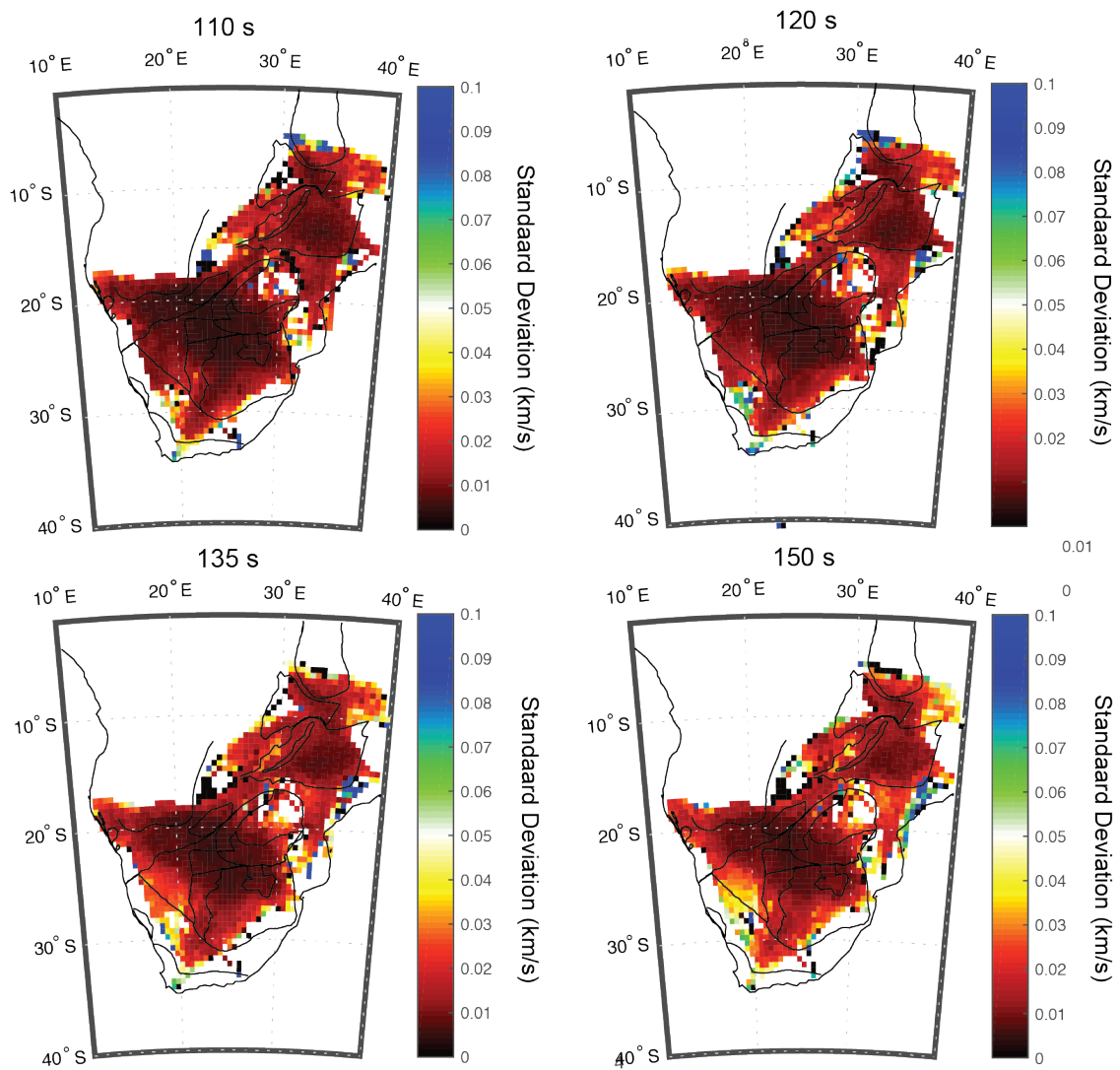


Figure C-6 **continued**: Estimates of the standard deviation in phase velocity from stacking phase velocity maps driven from eikonal tomography

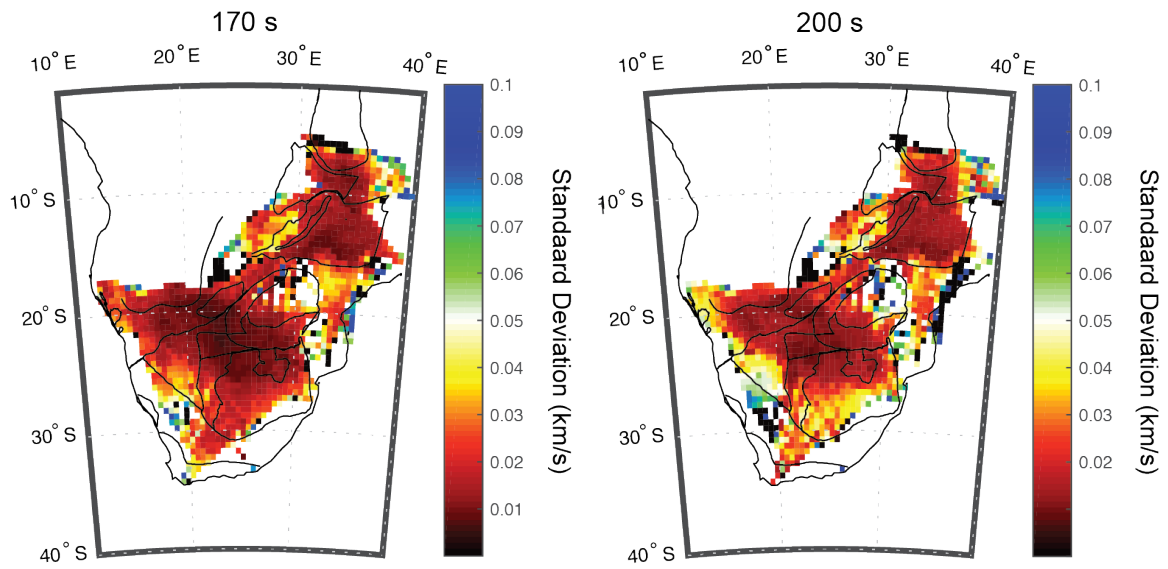


Figure C-6 continued: Estimates of the standard deviation in phase velocity from stacking phase velocity maps driven from eikonal tomography

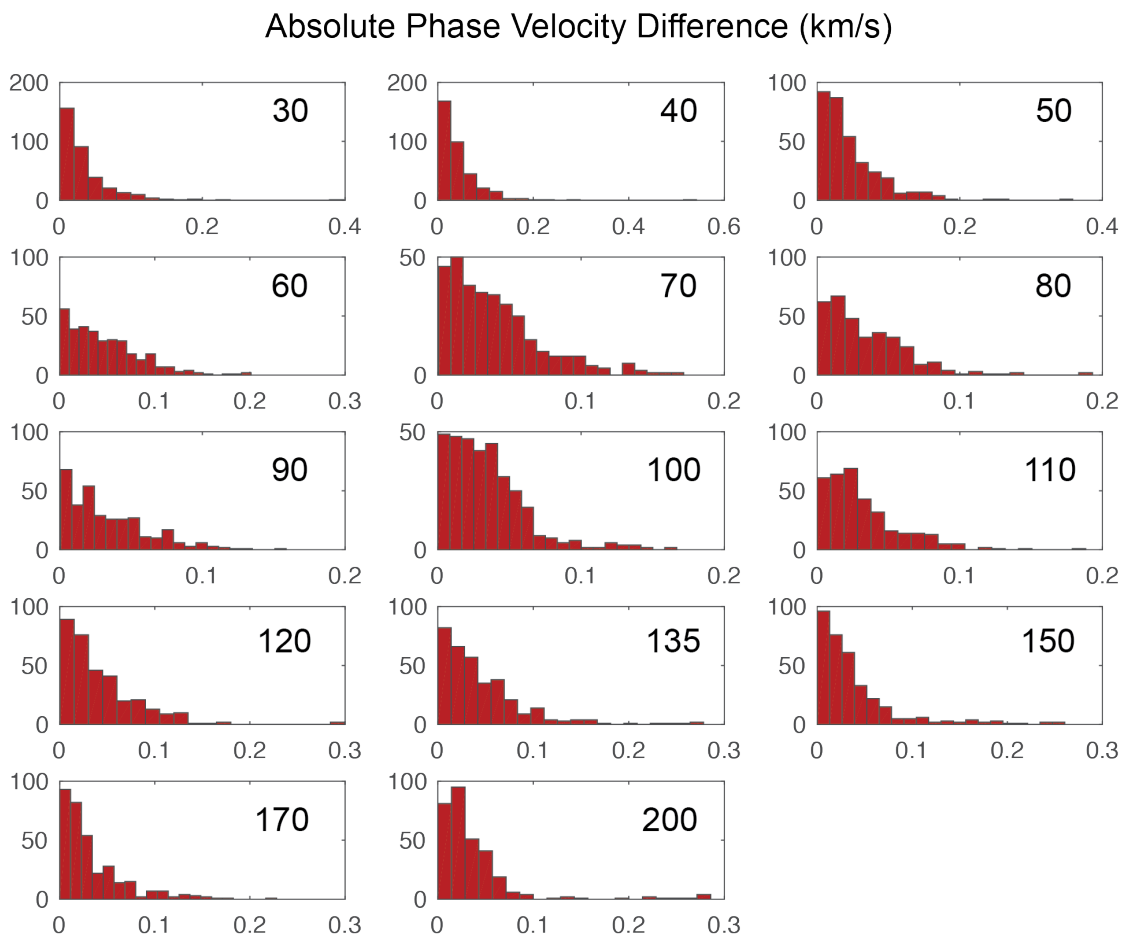


Figure C-7: Absolute phase velocity (30-200 s) differences for each grid cell measured with interstation distances limited to 250 km from the same cell measurement when interstation spacing was increased to 850 km. This shows that the difference between phase velocity measurements with highly restricted interstation spacing are primarily within 0.1 km/s from those measured with the interstation distances increased to 850 km, even at the short periods.

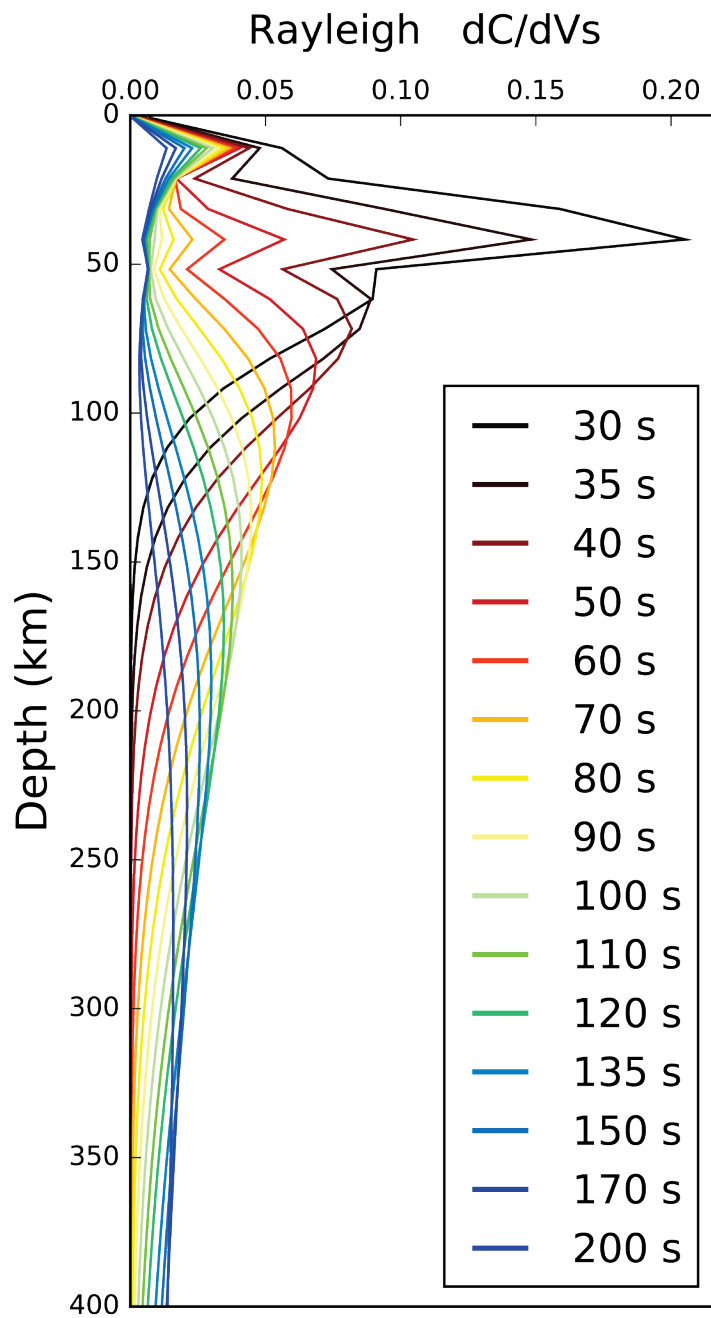


Figure C-8: Example sensitivity kernels for 30-200 s fundamental mode Rayleigh waves through a representative velocity model.

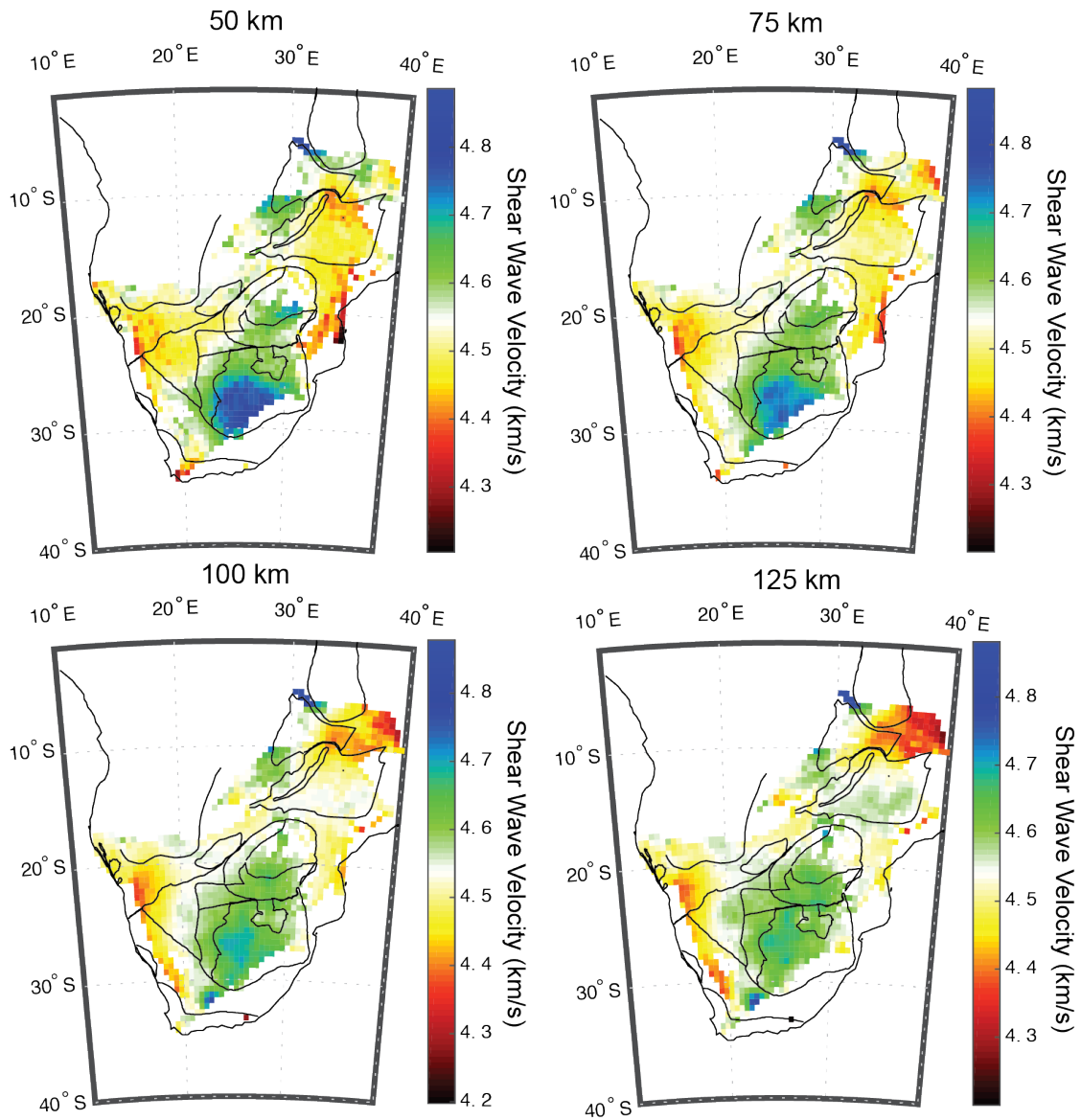


Figure C-9: Horizontal cross-sections (50-325 km) through the final shear wave velocity model at 25 km intervals. Tectonic boundaries (Begg et al., 2009; Frimmel and Frank, 1998) are marked by black lines.

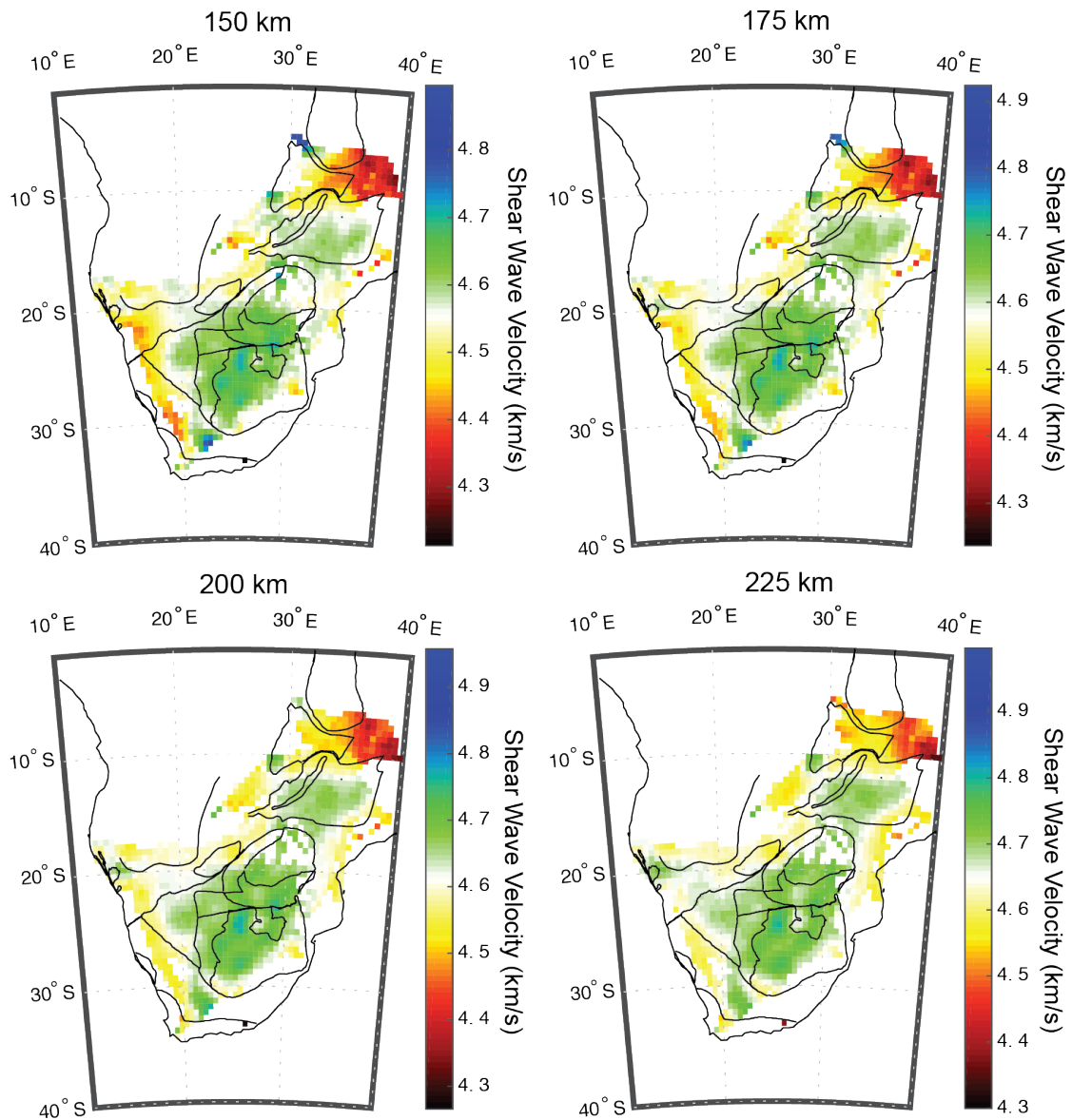


Figure C-9 continued: Horizontal cross-sections (50-325 km) through the final shear wave velocity model at 25 km intervals. Tectonic boundaries (Begg et al., 2009; Frimmel and Frank, 1998) are marked by black lines.

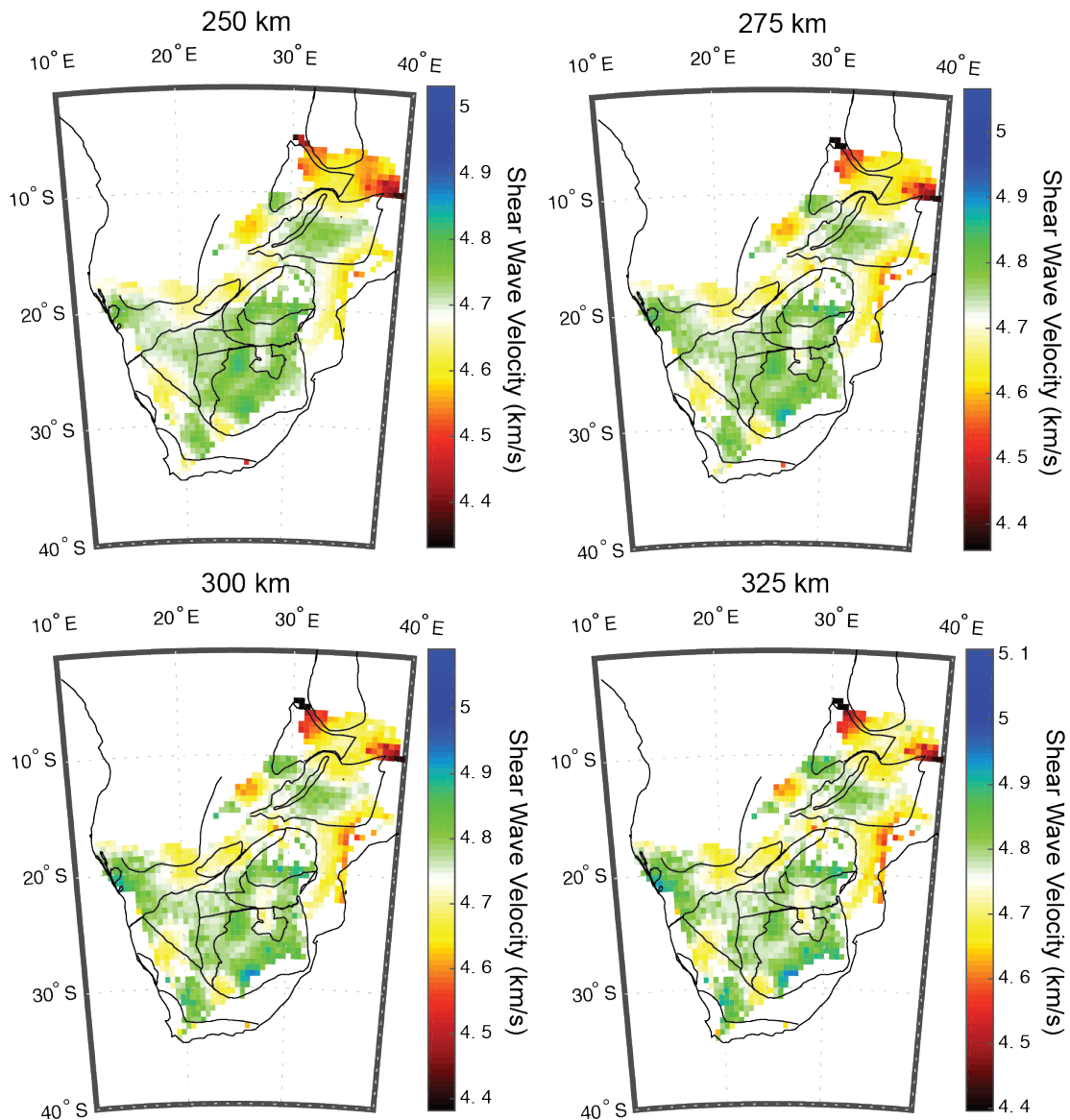


Figure C-9 continued: Horizontal cross-sections (50-325 km) through the final shear wave velocity model at 25 km intervals. Tectonic boundaries (Begg et al., 2009; Frimmel and Frank, 1998) are marked by black lines.

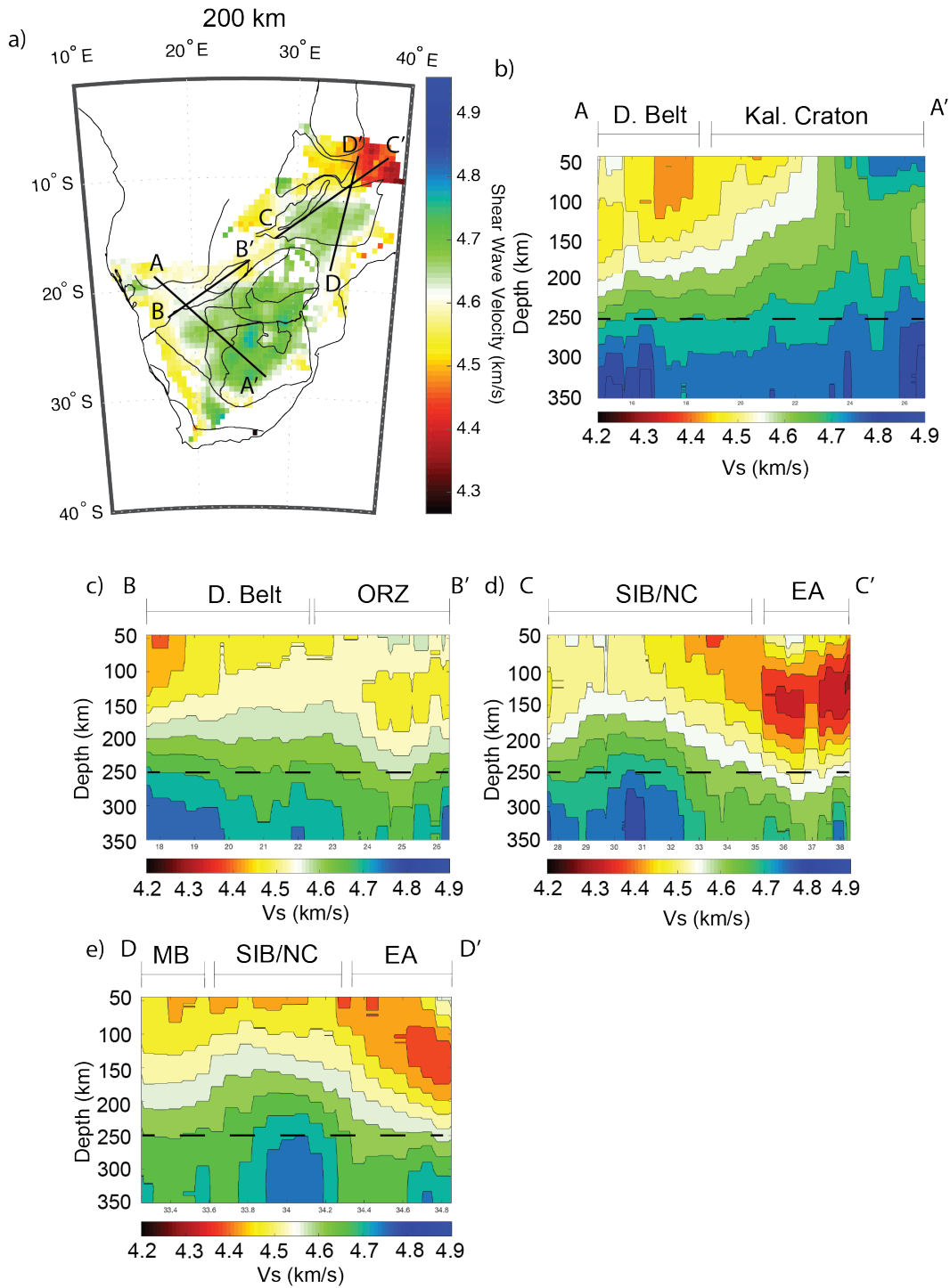


Figure C-10: a) Horizontal cross-section through shear wave velocity model. Surface intersections of vertical cross-sections are labeled A-D. b-e) Vertical cross-sections through the shear wave velocity model. Tectonic regions are labeled at the surface. D. Belt – Damara Belt; Kal. Craton – Kalahari Craton; ORZ – Okavango Rift Zone; EA – Eastern Africa; SIB/NC – Southern Irumide Belt / Niassa Craton; MB – Mozambique Belt.

Bibliography

- Adams, A., Nyblade, A. and Weeraratne, D., (2012) Upper mantle shear wave velocity structure beneath the East African plateau: evidence for a deep, plateau-wide low velocity anomaly. *Geophysical Journal International*, 189(1), 123-142.
- Adams, A., Miller, J. and Accardo, N., (2018) Relationships between lithospheric structures and rifting in the East African Rift System: A Rayleigh wave tomography study. *Geochemistry, Geophysics, Geosystems*, 19(10), 3793-3810.
- Adams, A. and Nyblade, A., (2011) Shear wave velocity structure of the southern African upper mantle with implications for the uplift of southern Africa. *Geophysical Journal International*, 186(2), 808-824.
- Anhaeusser, C.R., (1973) A Discussion on the evolution of the Precambrian crust-The evolution of the early Precambrian crust of Southern Africa. *Philosophical Transactions of the Royal Society of London. Series A, Mathematical and Physical Sciences*, 273(1235), 359-388.
- Batumike, J.M., Griffin, W.L., O'Reilly, S.Y., Belousova, E.A. and Pawlitschek, M., (2009) Crustal evolution in the central Congo-Kasai Craton, Luebo, DR Congo: insights from zircon U-Pb ages, Hf-isotope and trace-element data. *Precambrian Research*, 170(1-2), 107-115.
- Barletta, V. R., Bevis, M., Smith, B. E., Wilson, T. J., Brown, A., Bordoni, A., Willis, M., Khan, S. A., Rovira-Navarro, M., Dalziel, I. W., Smalley Jr., R., Kendrick, E., Konfal, S.,

- Caccamise, D. J., Aster, R. C., Nyblade, A. A., Wiens, D. A., (2018) Observed rapid bedrock uplift in Amundsen Sea Embayment promotes ice-sheet stability. *Science*, 360(6395), 1335-1339.
- Bauer, K., Neben, S., Schreckenberger, B., Emmermann, R., Hinz, K., Fechner, N., Gohl, K., Schulze, A., Trumbull, R.B. and Weber, K., (2000) Deep structure of the Namibia continental margin as derived from integrated geophysical studies. *Journal of Geophysical Research: Solid Earth*, 105(B11), 25829-25853.
- Begg, G.C., Griffin, W.L., Natapov, L.M., O'Reilly, S.Y., Grand, S.P., O'Neill, C.J., Hronsky, J.M.A., Djomani, Y.P., Swain, C.J., Deen, T. and Bowden, P., (2009) The lithospheric architecture of Africa: Seismic tomography, mantle petrology, and tectonic evolution. *Geosphere*, 5(1), 23-50.
- Behrendt, J. C., Saltus, R., Damaske, D., McCafferty, A., Finn, C. A., Blankenship, D., & Bell, R. E. (1996). Patterns of late Cenozoic volcanic and tectonic activity in the West Antarctic rift system revealed by aeromagnetic surveys. *Tectonics*, 15(3), 660-676.
- Brancolini, G., Cooper, A. K., & Coren, F. (1995). Seismic facies and glacial history in the western Ross Sea (Antarctica). *Geology and seismic stratigraphy of the Antarctic margin*, 209-233.
- Brandt, M.B., Grand, S.P., Nyblade, A.A. and Dirks, P.H., (2012). Upper mantle seismic structure beneath Southern Africa: Constraints on the buoyancy supporting the African superswell. *Pure and applied geophysics*, 169(4), 595-614.

- Brenn, G. R., Hansen, S. E., & Park, Y. (2017). Variable thermal loading and flexural uplift along the Transantarctic Mountains, Antarctica. *Geology*, 45(5), 463-466.
- Brock, B.B., (1959) On orogenic evolution, with special reference to southern Africa. *South African Journal of Geology*, 62(1), 325-372.
- Bufford, K.M., Atekwana, E.A., Abdelsalam, M.G., Shemang, E., Atekwana, E.A., Mickus, K., Moidaki, M., Modisi, M.P. and Molwalefhe, L., (2012) Geometry and faults tectonic activity of the Okavango Rift Zone, Botswana: Evidence from magnetotelluric and electrical resistivity tomography imaging. *Journal of African Earth Sciences*, 65, 61-71
- Cammarano, F., Goes, S., Vacher, P., & Giardini, D. (2003). Inferring upper-mantle temperatures from seismic velocities. *Physics of the Earth and Planetary Interiors*, 138(3-4), 197-222.
- Chaput, J., Aster, R. C., Huerta, A., Sun, X., Lloyd, A. D., Wiens, D., Nyblade, A. A., Anandkrishnan, S., Winberry, J. P., and Wilson, T. (2014). The crustal thickness of West Antarctica. *Journal of Geophysical Research: Solid Earth* 119 (1), 378-395.
- Chen, C.W., Rondenay, S., Weeraratne, D.S. and Snyder, D.B., (2007). New constraints on the upper mantle structure of the Slave craton from Rayleigh wave inversion. *Geophysical Research Letters*, 34(10).
- Chevrot, S. and Zhao, L., (2007) Multiscale finite-frequency Rayleigh wave tomography of the Kaapvaal craton. *Geophysical Journal International*, 169(1), 201-215

- Cornell, D.H., Van Schijndel, V., Ingolfsson, O., Scherstén, A., Karlsson, L., Wojtyla, J. and Karlsson, K., (2011) Evidence from Dwyka tillite cobbles of Archaean basement beneath the Kalahari sands of southern Africa. *Lithos*, 125(1-2), 482-502.
- Cornell, D.H., Thomas, R.J., Gibson, R., Moen, H.F.G., Reid, D.L., Moore, J.M. and Gibson, R.L., (2006) The Namaqua-Natal Province. Geological Society of South Africa.
- Dalziel, I. W., & Elliot, D. H. (1982). West Antarctica: problem child of Gondwanaland. *Tectonics*, 1(1), 3-19.
- Danesi, S., & Morelli, A. (2001). Structure of the upper mantle under the Antarctic Plate from surface wave tomography. *Geophysical Research Letters*, 28(23), 4395-4398.
- Davey, F. J. (1981). Geophysical studies in the Ross Sea region. *Journal of the Royal Society of New Zealand*, 11(4), 465-479.
- Davey, F. J., & Brancolini, G. (1995). The Late Mesozoic and Cenozoic structural setting of the Ross Sea region. *Geology and seismic stratigraphy of the Antarctic margin*, 167-182.
- de Wit, M.J., Jones, M.G. and Buchanan, D.L., (1992) The geology and tectonic evolution of the Pietersburg greenstone belt, South Africa. *Precambrian Research*, 55(1-4), 123-153.
- Decesari, R. C., Wilson, D. S., Luyendyk, B. P., & Faulkner, M. (2007). Cretaceous and tertiary extension throughout the Ross Sea, Antarctica. In *Antarctica: A Keystone in a Changing*

World – Online Proceedings of the 10th ISAES X, edited by A. K. Cooper et al., U.S.

Geological Survey Open File Rep., 1047.

Domingues, A., Silveira, G., Ferreira, A.M., Chang, S.J., Custódio, S. and Fonseca, J.F., (2016)

Ambient noise tomography of the East African Rift in Mozambique. *Geophysical Journal International*, 204(3), 1565-1578.

Duncan, R.A., Hooper, P.R., Rehacek, J., Marsh, J. and Duncan, A.R., (1997) The timing and

duration of the Karoo igneous event, southern Gondwana. *Journal of Geophysical Research: Solid Earth*, 102(B8), 18127-18138.

Eglinton, B.M., (2006) Evolution of the Namaqua-Natal Belt, southern Africa—A

geochronological and isotope geochemical review. *Journal of African Earth Sciences*, 46(1-2), 93-111.

Engelhardt, H. (2004). Ice temperature and high geothermal flux at Siple Dome, West Antarctica,

from borehole measurements. *Journal of Glaciology*, 50(169), 251-256.

Emry, E.L., Shen, Y., Nyblade, A.A., Flinders, A. and Bao, X., (2019) Upper Mantle Earth

Structure in Africa From Full-Wave Ambient Noise Tomography. *Geochemistry, Geophysics, Geosystems*, 20(1), 120-147.

Emry, E. L., Nyblade, A. A., Julià, J., Anandakrishnan, S., Aster, R. C., Wiens, D. A., Huerta, A.

D., & Wilson, T. J. (2015). The mantle transition zone beneath West Antarctica: Seismic

- evidence for hydration and thermal upwellings. *Geochemistry, Geophysics, Geosystems*, 16(1), 40-58.
- Faccenna, C., Rossetti, F., Becker, T. W., Danesi, S., & Morelli, A. (2008). Recent extension driven by mantle upwelling beneath the Admiralty Mountains (East Antarctica). *Tectonics*, 27(4).
- Fadel, I., van der Meijde, M. and Paulssen, H., (2018) Crustal structure and dynamics of Botswana. *Journal of Geophysical Research: Solid Earth*, 123(12), 10-659.
- Ferraccioli, F., Armadillo, E., Jordan, T., Bozzo, E., & Corr, H. (2009). Aeromagnetic exploration over the East Antarctic Ice Sheet: a new view of the Wilkes Subglacial Basin. *Tectonophysics*, 478(1-2), 62-77.
- Fielding, C. R., Henrys, S. A., & Wilson, T. J. (2006). Rift history of the western Victoria Land Basin: a new perspective based on integration of cores with seismic reflection data. *Antarctica*, 309-318.
- Finn, C. A., Müller, R. D., & Panter, K. S. (2005). A Cenozoic diffuse alkaline magmatic province (DAMP) in the southwest Pacific without rift or plume origin. *Geochemistry, Geophysics, Geosystems*, 6(2).
- Fisher, A. T., Mankoff, K. D., Tulaczyk, S. M., Tyler, S. W., & Foley, N. (2015). High geothermal heat flux measured below the West Antarctic Ice Sheet. *Science advances*, 1(6), e1500093.

- Fishwick, S. and Bastow, I.D., (2011) Towards a better understanding of African topography: a review of passive-source seismic studies of the African crust and upper mantle. *Geological Society, London, Special Publications*, 357(1), 343-371.
- Fishwick, S., (2010) Surface wave tomography: imaging of the lithosphere–asthenosphere boundary beneath central and southern Africa?. *Lithos*, 120(1-2), 63-73.
- Fitzgerald, P. G. (1992). The Transantarctic Mountains of southern Victoria Land: The application of apatite fission track analysis to a rift shoulder uplift. *Tectonics*, 11(3), 634-662.
- Fitzgerald, P. G. (2002). Tectonics and landscape evolution of the Antarctic plate since the breakup of Gondwana, with an emphasis on the West Antarctic Rift System and the Transantarctic Mountains. *Royal Society of New Zealand Bulletin*, 35, 453-469.
- Fretwell, P., Pritchard, H. D., Vaughan, D. G., Bamber, J. L., Barrand, N. E., Bell, R., Bianchi, C., Bingham, R. G., Blankenship, D. D., Casassa, G., & Catania, G. (2013). Bedmap2: improved ice bed, surface and thickness datasets for Antarctica.
- Fonseca, J.F.B.D., Chamussa, J., Domingues, A., Helffrich, G., Antunes, E., van Aswegen, G., Pinto, L.V., Custódio, S. and Manhiça, V.J., (2014) MOZART: a seismological investigation of the East African rift in Central Mozambique. *Seismological Research Letters*, 85(1), 108-116.

- Fouch, M.J., James, D.E., VanDecar, J.C., Van der Lee, S. and Kaapvaal Seismic Group, (2004) Mantle seismic structure beneath the Kaapvaal and Zimbabwe Cratons. *South African Journal of Geology*, 107(1-2), 33-44.
- Forsyth, D.W. and Li, A., (2005) Array analysis of two-dimensional variations in surface wave phase velocity and azimuthal anisotropy in the presence of multipathing interference. *Seismic Earth: Array Analysis of Broadband Seismograms*, 157, 81-97.
- Forte, A.M., Quéré, S., Moucha, R., Simmons, N.A., Grand, S.P., Mitrovica, J.X. and Rowley, D.B., (2010) Joint seismic–geodynamic–mineral physical modelling of African geodynamics: A reconciliation of deep-mantle convection with surface geophysical constraints. *Earth and Planetary Science Letters*, 295(3-4), 329-341.
- Frimmel, H.E. and Frank, W., (1998) Neoproterozoic tectono-thermal evolution of the Gariep Belt and its basement, Namibia and South Africa. *Precambrian Research*, 90(1-2), 1-28.
- Gee, L.S. and Jordan, T.H., (1992) Generalized seismological data functionals. *Geophysical Journal International*, 111(2), 363-390.
- Gomez, N., Pollard, D., & Holland, D. (2015). Sea-level feedback lowers projections of future Antarctic Ice-Sheet mass loss. *Nature communications*, 6, 8798.
- Grand, S.P. and Helmberger, D.V., (1984). Upper mantle shear structure of North America. *Geophysical Journal International*, 76(2), 399-438.

- Granot, R., Cande, S. C., Stock, J. M., & Damaske, D. (2013). Revised Eocene-Oligocene kinematics for the West Antarctic rift system. *Geophysical Research Letters*, *40*(2), 279-284.
- Graw, J. H., Adams, A. N., Hansen, S. E., Wiens, D. A., Hackworth, L., & Park, Y. (2016). Upper mantle shear wave velocity structure beneath northern Victoria Land, Antarctica: Volcanism and uplift in the northern Transantarctic Mountains. *Earth and Planetary Science Letters*, *449*, 48-60.
- Griffin, W.L., O'Reilly, S.Y., Natapov, L.M. and Ryan, C.G., (2003). The evolution of lithospheric mantle beneath the Kalahari Craton and its margins. *Lithos*, *71*(2-4), 215-241.
- Grijalva, A., Nyblade, A.A., Homman, K., Accardo, N.J., Gaherty, J.B., Ebinger, C.J., Shillington, D.J., Chindandali, P.R., Mbogoni, G., Ferdinand, R.W. and Mulibo, G., (2018) Seismic Evidence for Plume-and Craton-Influenced Upper Mantle Structure Beneath the Northern Malawi Rift and the Rungwe Volcanic Province, East Africa. *Geochemistry, Geophysics, Geosystems*, *19*(10), 3980-3994.
- Gurnis, M., Mitrovica, J.X., Ritsema, J. and van Heijst, H.J., (2000) Constraining mantle density structure using geological evidence of surface uplift rates: The case of the African superplume. *Geochemistry, Geophysics, Geosystems*, *1*(7).
- Hansen, S. E., Graw, J. H., Kenyon, L. M., Nyblade, A. A., Wiens, D. A., Aster, R. C., Huerta, A. D., Anandakrishnan, S., & Wilson, T. J. (2014). Imaging the Antarctic mantle using adaptively parameterized P-wave tomography: Evidence for heterogeneous structure beneath West Antarctica. *Earth and Planetary Science Letters*, *408*, 66-78.

- Hansma, J., Tohver, E., Schrank, C., Jourdan, F. and Adams, D., (2016) The timing of the Cape Orogeny: New $^{40}\text{Ar}/^{39}\text{Ar}$ age constraints on deformation and cooling of the Cape Fold Belt, South Africa. *Gondwana Research*, 32, 122-137.
- Hanson, R.E., (2003) Proterozoic geochronology and tectonic evolution of southern Africa. *Geological Society, London, Special Publications*, 206(1), 427-463.
- Heeszel, D. S., Wiens, D. A., Anandakrishnan, S., Aster, R. C., Dalziel, I. W., Huerta, A. D., Nyblade, A. A., Wilson, T. J., & Winberry, J. P. (2016). Upper mantle structure of central and West Antarctica from array analysis of Rayleigh wave phase velocities. *Journal of Geophysical Research: Solid Earth*, 121(3), 1758-1775.
- Herrmann, R.B., (2013) Computer programs in seismology: An evolving tool for instruction and research. *Seismological Research Letters*, 84(6), 1081-1088.
- Hole, M. J., & LeMasurier, W. E. (1994). Tectonic controls on the geochemical composition of Cenozoic, mafic alkaline volcanic rocks from West Antarctica. *Contributions to Mineralogy and Petrology*, 117(2), 187-202.
- James, D.E., Fouch, M.J., VanDecar, J.C., Van Der Lee, S. and Kaapvaal Seismic Group, (2001) Tectospheric structure beneath southern Africa. *Geophysical Research Letters*, 28(13), 2485-2488.

- Janney, P.E., Shirey, S.B., Carlson, R.W., Pearson, D.G., Bell, D.R., Le Roex, A.P., Ishikawa, A., Nixon, P.H. and Boyd, F.R., (2010) Age, composition and thermal characteristics of South African off-craton mantle lithosphere: Evidence for a multi-stage history. *Journal of Petrology*, 51(9), 1849-1890.
- Jelsma, H.A. and Dirks, P.H., (2002) Neoproterozoic tectonic evolution of the Zimbabwe Craton. *Geological Society, London, Special Publications*, 199(1), 183-211.
- Jin, G. and Gaherty, J.B., (2015) Surface wave phase-velocity tomography based on multichannel cross-correlation. *Geophysical Journal International*, 201(3), 1383-1398.
- Jin, G., Gaherty, J.B., Abers, G.A., Kim, Y., Eilon, Z. and Buck, W.R., (2015) Crust and upper mantle structure associated with extension in the Woodlark Rift, Papua New Guinea from Rayleigh-wave tomography. *Geochemistry, Geophysics, Geosystems*, 16(11), 3808-3824.
- Jordan, T.H., (1979) Mineralogies, densities and seismic velocities of garnet lherzolites and their geophysical implications. *The Mantle Sample: Inclusion in Kimberlites and Other Volcanics*, 16, 1-14.
- Kachingwe, M., Nyblade, A. and Julia, J., (2015) Crustal structure of Precambrian terranes in the southern African subcontinent with implications for secular variation in crustal genesis. *Geophysical Journal International*, 202(1), 533-547.

- Karner, G. D., Studinger, M., & Bell, R. E. (2005). Gravity anomalies of sedimentary basins and their mechanical implications: Application to the Ross Sea basins, West Antarctica. *Earth and Planetary Science Letters*, 235(3-4), 577-596.
- Kennett, B.L., Engdahl, E.R. and Buland, R., (1995) Constraints on seismic velocities in the Earth from traveltimes. *Geophysical Journal International*, 122(1), 108-124.
- Kennett, B. L. N., & Engdahl, E. R. (1991). Traveltimes for global earthquake location and phase identification. *Geophysical Journal International*, 105(2), 429-465.
- Kgaswane, E.M., Nyblade, A.A., Julià, J., Dirks, P.H., Durrheim, R.J. and Pasyanos, M.E., (2009) Shear wave velocity structure of the lower crust in southern Africa: Evidence for compositional heterogeneity within Archaean and Proterozoic terrains. *Journal of Geophysical Research: solid earth*, 114(B12).
- Khoza, D., Jones, A.G., Muller, M.R., Evans, R.L., Webb, S.J. and Miensopust, M., (2013) Tectonic model of the Limpopo belt: constraints from magnetotelluric data. *Precambrian Research*, 226, 143-156.
- Kröner, A., (1977) The Precambrian geotectonic evolution of Africa: plate accretion versus plate destruction. *Precambrian Research*, 4(2), 163-213.
- Kwadiba, M.T.O.G., Wright, C., Kgaswane, E.M., Simon, R.E. and Nguuri, T.K., (2003) Pn arrivals and lateral variations of Moho geometry beneath the Kaapvaal craton. *Lithos*, 71(2-4), 393-411.

- Lawrence, J. F., Wiens, D. A., Nyblade, A. A., Anandakrishnan, S., Shore, P. J., & Voigt, D. (2006). Crust and upper mantle structure of the Transantarctic Mountains and surrounding regions from receiver functions, surface waves, and gravity: implications for uplift models. *Geochemistry, Geophysics, Geosystems*, 7(10).
- LeMasurier, W. E. (1990). Late Cenozoic volcanism on the Antarctic plate: an overview. *Volcanoes of the Antarctic plate and southern oceans*, 48, 1-17.
- LeMasurier, W.E., (2008). Neogene extension and basin deepening in the West Antarctic rift inferred from comparisons with the East African rift and other analogs. *Geology*, 36(3), 247-250.
- LeMasurier, W. E., & Landis, C. A. (1996). Mantle-plume activity recorded by low-relief erosion surfaces in West Antarctica and New Zealand. *Geological Society of America Bulletin*, 108(11), 1450-1466.
- LeMasurier, W.E., Choi, S.H., Hart, S.R., Mukasa, S. and Rogers, N. (2016). Reconciling the shadow of a subduction signature with rift geochemistry and tectonic environment in Eastern Marie Byrd Land, Antarctica. *Lithos* 260, 134-153.
- Li, A. and Burke, K., (2006) Upper mantle structure of southern Africa from Rayleigh wave tomography. *Journal of Geophysical Research: Solid Earth*, 111(B10)

- Li, A. and Li, L., (2015) Love wave tomography in southern Africa from a two-plane-wave inversion method. *Geophysical Journal International*, 202(2), 1005-1020.
- Lithgow-Bertelloni, C. and Silver, P.G., (1998) Dynamic topography, plate driving forces and the African superswell. *Nature*, 395(6699), 269.
- Lough, A. C., Wiens, D. A., Barcheck, C. G., Anandakrishnan, S., Aster, R. C., Blankenship, D. D., Huerta, A. D., Nyblade, A. A., Young, D. A., & Wilson, T. J. (2013). Seismic detection of an active subglacial magmatic complex in Marie Byrd Land, Antarctica. *Nature Geoscience*, 6(12), 1031.
- Lloyd, A. J., Wiens, D. A., Nyblade, A. A., Anandakrishnan, S., Aster, R. C., Huerta, A. D., Wilson, T. J., Dalziel, I. W., Shore, P. J., & Zhao, D. (2015). A seismic transect across West Antarctica: Evidence for mantle thermal anomalies beneath the Bentley Subglacial Trench and the Marie Byrd Land Dome. *Journal of Geophysical Research: Solid Earth*, 120(12), 8439-8460.
- Masters, G., Johnson, S., Laske, G., & Bolton, H. (1996). A shear-velocity model of the mantle. *Phil. Trans. R. Soc. Lond. A*, 354(1711), 1385-1411.
- Matzel, E. and Grand, S.P. (2004), *The anisotropic seismic structure of the East European platform*, *Journal of Geophysical Research*, 109, B01302
- Maule, C. F., Purucker, M. E., Olsen, N., & Mosegaard, K. (2005). Heat flux anomalies in Antarctica revealed by satellite magnetic data. *Science*, 309(5733), 464-467.

McCourt, S., Hilliard, P., Armstrong, R.A. and Munyanyiwa, H., (2001) SHRIMP U-Pb zircon geochronology of the Hurungwe granite northwest Zimbabwe: Age constraints on the timing of the Magondi orogeny and implications for the correlation between the Kheis and Magondi Belts. *South African Journal of Geology*, 104(1), 39-46.

McNamara, A.K. and Zhong, S., (2005) Thermochemical structures beneath Africa and the Pacific Ocean. *Nature*, 437(7062), 1136.

Mégnin, C. and Romanowicz, B., (2000) The three-dimensional shear velocity structure of the mantle from the inversion of body, surface and higher-mode waveforms. *Geophysical Journal International*, 143(3), 709-728.

Miensopust, M.P., Jones, A.G., Muller, M.R., Garcia, X. and Evans, R.L., (2011) Lithospheric structures and Precambrian terrane boundaries in northeastern Botswana revealed through magnetotelluric profiling as part of the Southern African Magnetotelluric Experiment. *Journal of Geophysical Research: Solid Earth*, 116(B2).

Morin, R. H., Williams, T., Henrys, S. A., Mogens, D., Niessen, F., & Hansaraj, D. (2010). Heat flow and hydrologic characteristics at the AND-1B borehole, ANDRILL McMurdo Ice Shelf Project, Antarctica. *Geosphere*, 6(4), 370-378.

Mukasa, S. B., & Dalziel, I. W. (2000). Marie Byrd Land, West Antarctica: Evolution of Gondwana's Pacific margin constrained by zircon U-Pb geochronology and feldspar common-Pb isotopic compositions. *Geological Society of America Bulletin*, 112(4), 611-627.

- Mulibo, G.D. and Nyblade, A.A., (2013a) The P and S wave velocity structure of the mantle beneath eastern Africa and the African superplume anomaly. *Geochemistry, Geophysics, Geosystems*, 14(8), 2696-2715
- Mulibo, G.D. and Nyblade, A.A., (2013b) Mantle transition zone thinning beneath eastern Africa: Evidence for a whole-mantle superplume structure. *Geophysical Research Letters*, 40(14), 3562-3566.
- Muller, M.R., Jones, A.G., Evans, R.L., Grütter, H.S., Hatton, C., Garcia, X., Hamilton, M.P., Miensoopust, M.P., Cole, P., Ngwisanyi, T. and Hutchins, D., (2009) Lithospheric structure, evolution and diamond prospectivity of the Rehoboth Terrane and western Kaapvaal Craton, southern Africa: Constraints from broadband magnetotellurics. *Lithos*, 112, 93-105.
- Nair, S.K., Gao, S.S., Liu, K.H. and Silver, P.G., (2006) Southern African crustal evolution and composition: Constraints from receiver function studies. *Journal of Geophysical Research: Solid Earth*, 111(B2).
- Nguuri, T.K., Gore, J., James, D.E., Webb, S.J., Wright, C., Zengeni, T.G., Gwavava, O., Snoke, J.A. and Kaapvaal Seismic Group, (2001) Crustal structure beneath southern Africa and its implications for the formation and evolution of the Kaapvaal and Zimbabwe cratons. *Geophysical Research Letters*, 28(13), 2501-2504.
- Ni, S., Tan, E., Gurnis, M. and Helmberger, D., (2002) Sharp sides to the African superplume. *science*, 296(5574), 1850-1852.

- Nyblade, A.A. and Robinson, S.W., (1994) The african superswell. *Geophysical research letters*, 21(9), 765-768.
- Nyblade, A.A. and Sleep, N.H., (2003) Long lasting epeirogenic uplift from mantle plumes and the origin of the Southern African Plateau. *Geochemistry, Geophysics, Geosystems*, 4(12).
- O'Donnell, J. P., Selway, K., Nyblade, A. A., Brazier, R. A., Wiens, D. A., Anandakrishnan, S., Aster, R. C., Huerta, A. D., Wilson, T. J., & Winberry, J. P. (2017). The uppermost mantle seismic velocity and viscosity structure of central West Antarctica. *Earth and Planetary Science Letters*, 472, 38-49.
- O'Donnell, J.P., Adams, A., Nyblade, A.A., Mulibo, G.D. and Tugume, F., (2013) The uppermost mantle shear wave velocity structure of eastern Africa from Rayleigh wave tomography: Constraints on rift evolution. *Geophysical Journal International*, 194(2), 961-978.
- Olsson, J.R., Söderlund, U., Klausen, M.B. and Ernst, R.E., (2010) U–Pb baddeleyite ages linking major Archean dyke swarms to volcanic-rift forming events in the Kaapvaal craton (South Africa), and a precise age for the Bushveld Complex. *Precambrian Research*, 183(3), 490-500.
- Ortiz, K., Nyblade, A., van der Meijde, M., Paulssen, H., Kwadiba, M., Ntibinyane, O., Durrheim, R., Fadel, I. and Homman, K., (2019) Upper mantle P-and S-wave velocity

- structure of the Kalahari Craton and surrounding Proterozoic terranes, southern Africa. *Geophysical Research Letters*, 46(16), 9509-9518.
- Pasyanos, M.E. and Nyblade, A.A., (2007) A top to bottom lithospheric study of Africa and Arabia. *Tectonophysics*, 444(1-4), 27-44.
- Phillips, E.H., Sims, K.W., Blichert-Toft, J., Aster, R.C., Gaetani, G.A., Kyle, P.R., Wallace, P.J. & Rasmussen, D.J. (2018). The nature and evolution of mantle upwelling at Ross Island, Antarctica, with implications for the source of HIMU lavas. *Earth and Planetary Science Letters*, 498, 38-53.
- Pollard, D., DeConto, R. M., & Nyblade, A. A. (2005). Sensitivity of Cenozoic Antarctic ice sheet variations to geothermal heat flux. *Global and Planetary Change*, 49(1-2), 63-74.
- Priestley, K., McKenzie, D., Debayle, E. and Pilidou, S., (2008) The African upper mantle and its relationship to tectonics and surface geology. *Geophysical Journal International*, 175(3), 1108-1126.
- Ramirez, C., Nyblade, A., Hansen, S.E., Wiens, D.A., Anandakrishnan, S., Aster, R.C., Huerta, A.D., Shore, P. and Wilson, T., (2016). Crustal and upper-mantle structure beneath ice-covered regions in Antarctica from S-wave receiver functions and implications for heat flow. *Geophysical Journal International*, 204(3), 1636-1648.
- Ramirez, C., Nyblade, A., Emry, E.L., Julià, J., Sun, X., Anandakrishnan, S., Wiens, D.A., Aster, R.C., Huerta, A.D., Winberry, P. and Wilson, T. (2017). Crustal structure of the

- Transantarctic Mountains, Ellsworth Mountains and Marie Byrd Land, Antarctica: constraints on shear wave velocities, Poisson's ratios and Moho depths. *Geophysical Journal International*, 211(3), 1328-1340.
- Raveloson, A., Nyblade, A., Fishwick, S., Mangongolo, A. and Master, S., (2015) The upper mantle seismic velocity structure of south-central Africa and the seismic architecture of Precambrian lithosphere beneath the Congo Basin. In *Geology and Resource Potential of the Congo Basin* (3-18). Springer, Berlin, Heidelberg.
- Ravenna, M., Lebedev, S., Fulla, J. and Adam, J.M.C., (2018) Shear-Wave Velocity Structure of Southern Africa's Lithosphere: Variations in the Thickness and Composition of Cratons and Their Effect on Topography. *Geochemistry, Geophysics, Geosystems*, 19(5), 1499-1518.
- Rignot, E., Bamber, J. L., Van Den Broeke, M. R., Davis, C., Li, Y., Van De Berg, W. J., & Van Meijgaard, E. (2008). Recent Antarctic ice mass loss from radar interferometry and regional climate modelling. *Nature geoscience*, 1(2), 106.
- Ritsema, J. and van Heijst, H., (2000) New seismic model of the upper mantle beneath Africa. *Geology*, 28(1), 63-66.
- Ritsema, J., van Heijst, H.J. and Woodhouse, J.H., (1999) Complex shear wave velocity structure imaged beneath Africa and Iceland. *Science*, 286(5446), 1925-1928.

- Ritzwoller, M. H., Shapiro, N. M., Levshin, A. L., & Leahy, G. M. (2001). Crustal and upper mantle structure beneath Antarctica and surrounding oceans. *Journal of Geophysical Research: Solid Earth*, 106(B12), 30645-30670.
- Romanowicz, B., (2003) Global mantle tomography: progress status in the past 10 years. *Annual Review of Earth and Planetary Sciences*, 31(1), 303-328.
- Roult, G., Rouland, D., & Montagner, J. P. (1994). Antarctica II: upper-mantle structure from velocities and anisotropy. *Physics of the Earth and Planetary Interiors*, 84(1-4), 33-57.
- Sarafian, E., Evans, R.L., Abdelsalam, M.G., Atekwana, E., Elsenbeck, J., Jones, A.G. and Chikambwe, E., (2018) Imaging Precambrian lithospheric structure in Zambia using electromagnetic methods. *Gondwana Research*, 54, 38-49.
- Scholz, C.H., Koczyński, T.A. and Hutchins, D.G., (1976) Evidence for incipient rifting in southern Africa. *Geophysical Journal International*, 44(1), 135-144.
- Schutt, D.L. and Lesher, C.E., (2010) Compositional trends among Kaapvaal Craton garnet peridotite xenoliths and their effects on seismic velocity and density. *Earth and Planetary Science Letters*, 300(3-4), 367-373.
- Schroeder, D. M., Blankenship, D. D., Young, D. A., & Quartini, E. (2014). Evidence for elevated and spatially variable geothermal flux beneath the West Antarctic Ice Sheet. *Proceedings of the National Academy of Sciences*, 111(25), 9070-9072.

- Sebai, A., Stutzmann, E., Montagner, J.P., Sicilia, D. and Beucler, E., (2006) Anisotropic structure of the African upper mantle from Rayleigh and Love wave tomography. *Physics of the Earth and Planetary Interiors*, 155(1-2), 48-62.
- Siddoway, C. S. (2008). Tectonics of the West Antarctic Rift System: new light on the history and dynamics of distributed intracontinental extension. *Antarctica: A Keystone in a Changing World*, 91-114.
- Sieminski, A., Debayle, E., & L  v  que, J. J. (2003). Seismic evidence for deep low-velocity anomalies in the transition zone beneath West Antarctica. *Earth and Planetary Science Letters*, 216(4), 645-661.
- Silver, P.G., Gao, S.S., Liu, K.H. and Kaapvaal Seismic Group, 2001. Mantle deformation beneath southern Africa. *Geophysical Research Letters*, 28(13), 2493-2496.
- Simmons, N.A., Forte, A.M. and Grand, S.P., (2007) Thermochemical structure and dynamics of the African superplume. *Geophysical Research Letters*, 34(2).
- Shen, W., Wiens, D., Anandakrishnan, A., Aster, R.C., Gerstoft, P., Bromirski, P., Hansen, S.E., Dalziel, I., Heeszel, D., Huerta, A., Nyblade, A.A., Stephen, R., Wilson, T., Winberry, J.P. (2018) The crust and upper mantle structure of central and West Antarctica from Bayesian inversion of Rayleigh wave and receiver functions, *Journal of Geophysical Research*, 123.

- Tedla, G.E., Van Der Meijde, M., Nyblade, A.A. and Van der Meer, F.D., (2011) A crustal thickness map of Africa derived from a global gravity field model using Euler deconvolution. *Geophysical Journal International*, 187(1), 1-9.
- Trey, H., Cooper, A. K., Pellis, G., della Vedova, B., Cochrane, G., Brancolini, G., & Makris, J. (1999). Transect across the West Antarctic rift system in the Ross Sea, Antarctica. *Tectonophysics*, 301(1-2), 61-74.
- Tugume, F., Nyblade, A., Julià, J. and van der Meijde, M., (2013) Precambrian crustal structure in Africa and Arabia: evidence lacking for secular variation. *Tectonophysics*, 609, 250-266.
- Van Schijndel, V., Cornell, D.H., Hoffmann, K.H. and Frei, D., (2011) Three episodes of crustal development in the Rehoboth Province, Namibia. *Geological Society, London, Special Publications*, 357(1), 27-47.
- VanDecar, J. C., & Crosson, R. S. (1990). Determination of teleseismic relative phase arrival times using multi-channel cross-correlation and least squares. *Bulletin of the Seismological Society of America*, 80(1), 150-169.
- VanDecar, J. C. (1991). *Upper-mantle structure of the Cascadia subduction zone from non-linear teleseismic travel-time inversion* (Doctoral dissertation).
- Watson, T., Nyblade, A., Wiens, D. A., Anandakrishnan, S., Benoit, M., Shore, P. J., Voigt, D., & VanDecar, J. (2006). P and S velocity structure of the upper mantle beneath the

- Transantarctic Mountains, East Antarctic craton, and Ross Sea from travel time tomography. *Geochemistry, Geophysics, Geosystems*, 7(7).
- Weatherall, P., Marks, K.M., Jakobsson, M., Schmitt, T., Tani, S., Arndt, J.E., Rovere, M., Chayes, D., Ferrini, V. and Wigley, R., (2015) A new digital bathymetric model of the world's oceans. *Earth and Space Science*, 2(8), 331-345.
- Wessel, P., W. H. F. Smith, R. Scharroo, J. F. Luis, and F. Wobbe, Generic Mapping Tools: Improved version released, EOS Trans. AGU, 94, 409-410, 2013.
- Winberry, J. P., & Anandakrishnan, S. (2003). Seismicity and neotectonics of West Antarctica. *Geophysical Research Letters*, 30(18).
- Wright, C., Kgaswane, E.M., Kwadiba, M.T.O., Simon, R.E., Nguuri, T.K. and McRae-Samuel, R., (2003) South African seismicity, April 1997 to April 1999, and regional variations in the crust and uppermost mantle of the Kaapvaal craton. *Lithos*, 71(2-4), 369-392.
- Yang, Y., Li, A. and Ritzwoller, M.H., (2008) Crustal and uppermost mantle structure in southern Africa revealed from ambient noise and teleseismic tomography. *Geophysical Journal International*, 174(1), 235-248.
- Yang, Y., & Forsyth, D. W. (2006). Regional tomographic inversion of the amplitude and phase of Rayleigh waves with 2-D sensitivity kernels. *Geophysical Journal International*, 166(3), 1148-1160.

- Youssof, M., Thybo, H., Artemieva, I.M. and Levander, A., (2015) Upper mantle structure beneath southern African cratons from seismic finite-frequency P-and S-body wave tomography. *Earth and Planetary Science Letters*, 420, 174-186.
- Yu, Y., Liu, K.H., Huang, Z., Zhao, D., Reed, C.A., Moidaki, M., Lei, J. and Gao, S.S., (2017) Mantle structure beneath the incipient Okavango rift zone in southern Africa. *Geosphere*, 13(1), 102-111.
- Yu, Y., Liu, K.H., Moidaki, M., Reed, C.A. and Gao, S.S., (2015) No thermal anomalies in the mantle transition zone beneath an incipient continental rift: Evidence from the first receiver function study across the Okavango Rift Zone, Botswana. *Geophysical Journal International*, 202(2), 1407-1418.
- Yu, Y., Gao, S.S., Moidaki, M., Reed, C.A. and Liu, K.H., 2015. Seismic anisotropy beneath the incipient Okavango rift: Implications for rifting initiation. *Earth and Planetary Science Letters*, 430, pp.1-8.
- Yuan, X., Heit, B., Brune, S., Steinberger, B., Geissler, W.H., Jokat, W. and Weber, M., (2017). Seismic structure of the lithosphere beneath NW Namibia: Impact of the Tristan da Cunha mantle plume. *Geochemistry, Geophysics, Geosystems*, 18(1), 125-141.
- Yuan, H. and Romanowicz, B., (2010). Lithospheric layering in the North American craton. *Nature*, 466(7310), 1063.

VITA

Austin White-Gaynor

Education

- 2019 **PhD, Geosciences** Pennsylvania State University
Body and surface wave tomography of West Antarctica and southern Africa: Implications for lithospheric architecture, tectonic development, and geodynamics
- 2015 **MS, Geosciences** Pennsylvania State University
Seismic anisotropy across the Appalachian mountains and plateau
- 2012 **BS, Geosciences** Virginia Polytechnic Institute
Geophysics option, Mathematics Minor

Publications

- White-Gaynor, A**, et al., 2020, Seismic architecture of the upper mantle beneath southern Africa from body wave tomography, in review with *Geochemistry, Geophysics, Geosystems*
- White-Gaynor, A**, et al., 2019, Heterogeneous upper mantle structure beneath the Ross Sea Embayment and Marie Byrd Land, West Antarctica, revealed by P-wave tomography, *Earth and Planetary Science Letters*, 513, 40-50,
<https://doi.org/10.1016/j.epsl.2019.02.013>
- White-Gaynor, A** and Nyblade, A., 2017, Shear wave splitting across the Mid-Atlantic region of North America: a fossil anisotropy interpretation, *Geology*, 45, 555-558,
[doi:10.1130/G38794.1](https://doi.org/10.1130/G38794.1)

Awards and Scholarships

- 2017 Dr. Gabriel & Mrs. Katherine Leblanc Fellowship
- 2017 Richard Standish Good Scholarship
- 2017, 2018 Penn State Geosc. Graduate Colloquium – 2nd Place Oral Presentation (PhD)
- 2017 Penn State Graduate Student Exhibition – 2nd Place Poster Presentation
- 2015 Penn State Geosc. Graduate Colloquium – 2nd Place Oral Presentation (Master's)

Teaching Experience

- 2018 AfricaArray Field School, Instructor, South Africa
- 2018 Intro to Geosc. – Teaching Assistant for lab sections, taught multiple lectures
- 2017 Intro to Geosc. – Organized class material and taught 8 lectures to ~200 students

Field Work

- 2018 Seismic Imaging at the Susquehanna Shale Hills CZO, Pennsylvania
- 2013 – 2018 **POLENET**, South Pole and West Antarctica (4 Summer Seasons)
- 2013 – 2014 **PASEIS**, Pennsylvania